ISBN 978-82-326-3874-1 (printed version)
ISBN 978-82-326-3875-8 (electronic version)
ISSN 1503-8181

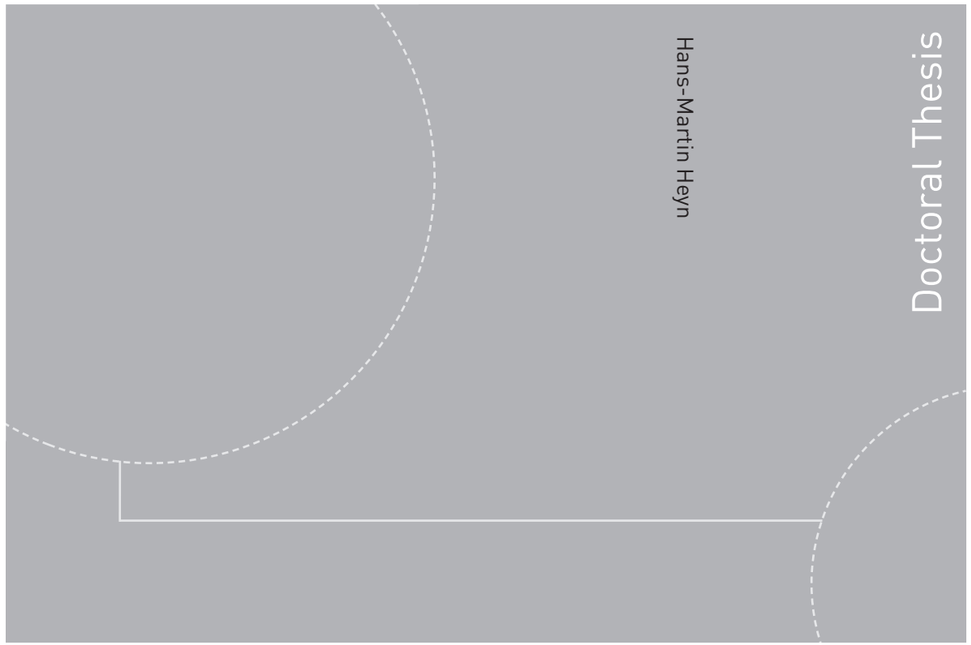

Doctoral theses at NTNU, 2019:138

Hans-Martin Heyn

Motion sensing on vessels operating in sea ice

A local ice monitoring system for transit and stationkeeping operations under the influence of sea ice

NTNU
Norwegian University of
Science and Technology

NTNU
Norwegian University of
Science and Technology

NTNU
Norwegian University of
Science and Technology
Faculty of Engineering
Department of Marine Technology

Doctoral theses at NTNU, 2019:138

NTNU

Hans-Martin Heyn

Motion sensing on vessels operating in sea ice

A local ice monitoring system for transit and stationkeeping operations under the influence of sea ice

Thesis for the degree of Philosophiae Doctor

Trondheim, May 2019

Norwegian University of Science and Technology
Faculty of Engineering
Department of Marine Technology

NTNU
Norwegian University of
Science and Technology

NTNU
Norwegian University of Science and Technology

Thesis for the degree of Philosophiae Doctor

Faculty of Engineering
Department of Marine Technology

ISBN 978-82-326-3874-1 (printed version)
ISBN 978-82-326-3875-8 (electronic version)
ISSN 1503-8181

Doctoral theses at NTNU, 2019:138

Printed by Skipnes Kommunikasjon as

For my family

Sammendrag

Smeltende sjøis i Arktis og Antarktis har medført en større interesse for skipsoperasjoner i polare strøk. Eksempler inkluderer frakttransport, ressursutforskning, fiske og turisme i disse områdene. For slike operasjoner er sjøis fortsatt den største risikoen. Utilgjengeligheten i polar områdene gjør ulykker vanskelig å håndtere. Miljøet i Arktis og Antarktis er ekstremt sårbar, og oljeutslipp assosiert med ulykker kan gi alvorlige og ødeleggende effekter på det naturlige habitatet. Is-observasjonssystemet måler kontinuerlig isforholdene rundt fartøyet det er installert på. Ved å gi tidlige advarsler, reduseres risikoen for ulykker.

Et is-observasjonssystem anvender en rekke teknologier for isovervåking, inkludert optiske kameraer, radaranlegg, drivbøyer og skrogbelastningsmålinger. Hver teknologi øker typisk muligheten for tidlig gjenkjenning av farlige isforholder, og innebefatter i tillegg at en får redundanse for det samlede systemet.

I denne avhandlingen presenteres, utvikles og valideres et lokalt is-observasjonssystem. Systemet baserer seg på distribuerte målinger av is-induserte vibrasjoner i skipets skrog, med det formål å øke sikkerheten under operasjoner i polare områder. Avhandlingen er strukturert som en serie av vitenskapelige artikler, og baserer seg på feltdata samlet inn under fire arktiske ekspedisjoner mellom 2015 og 2017.

En innledende studie etablerte forholdet mellom gjeldende isforholdene og is-induserte vibrasjoner i skroget av skipet. Etter en detaljert frekvensanalyse av is-induserte vibrasjoner konkluderes det med at akselerometre i skroget kan gi informasjon om isbryte-mekanismen og isforholdene rundt fartøyet. To ytterligere studier etablerte og validerte bruk av fordelte akselerometer som del av et is-observasjonssystem. Videre foreslo studien et system for å overvåke isforholdene i sanntid ved hjelp av statistisk signalbehandling og endringsdeteksjon. Dette systemet gir robust sanntidsinformasjon om de lokale isforholdene og fungerer uavhengig av værforholdet. En videre studie med flere sensorer langs skroget, som bruker metoder fra ekstremverdistatistikk, viste en sammenheng mellom isdrift-retningen og statistiske egenskapene av de målte signalene. De foreslåtte metodene tillater tidlig identifisering av isdrift-endringer.

Avhandlingen konkluderer at bevegelsessensor på et fartøy som opererer i sjøis gir et raskt og pålitelig lokalt is-observasjonssystem for skip som opererer i områdene med sjøis. Arbeidet indikerer at bevegelsessensor i fartøyets skrog også gir informasjon om sjøgang i hav, men en detaljert studie av dette ligger utenfor omfanget av denne avhandlingen.

I tillegg til hovedstudien inkluderer avhandlingen også en model for distribuer-

te bevegelses-målinger på skip i sjøis.

Summary

The diminishing sea ice in the Arctic and Antarctic could lead to a higher number of ship operations in these areas, such as cargo transit, resource exploration, fishing, and tourism. However, despite the sea ice reduction, sea ice remains the predominant risk during ship operations. Due to the remoteness and fragility of the polar regions, accidents are difficult to handle and could have devastating effects on the local ecosystem. Therefore, continuous assessment of the prevailing ice conditions is essential to operating vessels. Individual sensor systems, called ice monitoring systems, provide the necessary information for the ice condition assessment, and by giving early warnings, these systems reduce the risk of accidents.

A reliable ice observer system employs several technologies for ice monitoring such as optical cameras, radar systems, drift buoys, and hull strain measurements. Each additional technology increases the chance of early detection of dangerous ice conditions, and additionally adds redundancies to the overall system.

The aim of this thesis was to present and validate an applicable ice monitoring system that can increase the safety for vessels operating in polar regions. This thesis presents a series of studies, presented as a collection of journal papers, that lead to an on-board motion sensing based ice monitoring system for ships, which bases on distributed measurements of ice-induced vibrations in the ship's hull. The results of this thesis are based on field data collected during four Arctic cruises performed between 2015 and 2017.

An initial study established a relationship between the prevailing ice conditions and ice-induced vibrations in the ship's hull. A detailed frequency analysis of ice-induced vibrations concluded that accelerometers in the hull can provide information about the acting ice breaking mechanism, ice conditions around the vessel, and the location of ship-ice interaction along the hull. Two further studies established and validated the application of hull accelerometers as ice monitoring system. A first application study suggested to monitor ice conditions in real time with the help of statistical signal processing and change detection. It was found that the suggested ice monitoring system provides robust real-time information about the local ice conditions and operates independently of weather conditions. A second application study utilised several sensors along the hull and methods from extreme value statistics to find a relationship between the ice drift direction and statistical properties of the recorded signals. The proposed methods in this thesis would allow for an early detection of ice drift changes, which is essential for station-keeping operations in sea ice.

The overall research presented in this thesis conclude that motion sensing on vessels operating in sea ice provides a fast and reliable local ice monitoring system for both transit and station-keeping operations. It is further suggested, that motion sensing in the hull of a vessel also provides information about the current sea-state in open water. However, this possible application is outside the scope of this thesis.

Besides the main studies, the thesis additionally offers a contribution in form of a model for distributed motion sensing on ships operating in sea ice.

Contents

List of figures

List of tables

Abbreviations

AI	Artificial intelligence
AUV	Autonomous underwater vehicle
CCGS	Canadian coast guard ship
DOF	Degrees of freedom
IB	Icebreaker
IMU	Inertial measurement unit
MDOF	Multi-degrees of freedom
OATRC	Oden Arctic Technology Research Cruise
PSD	Power spectral density
SAR	Synthetic aperature radar
SKT	Station-keeping Trials in Ice
SPRS	Swedish Polar Research Secretariat
UAV	Unmanned aerial vehicle
UNCLOS	United Nations Convention on the Law of the Sea
USS	United States Ship

Preface

This thesis is submitted in partial fulfilment of the requirements for the degree of philosophiae doctor (PhD) at the Norwegian University of Science and Technology (NTNU). My doctoral studies were conducted at the Centre for Autonomous Marine Systems and Operations (NTNU AMOS) at the Department of Marine Technology (IMT) and at the Centre for research-based innovation (SFI) Sustainable Arctic Marine and Coastal Technology (NTNU SAMCoT) in the period September 2014 to August 2018. The Research Council of Norway (RCN) provided funding as part of the projects 223254 and 203471. My supervisors were Professor Roger Skjetne, Professor Mogens Blanke, Professor Sveinung Løset and Professor Asgeir J. Sørensen.

In September and October 2015 I visited the University Centre in Svalbard (UNIS) for studying Arctic offshore engineering. From August 2017 to December 2017 I had the privilege of visiting Professor Mogens Blanke at the Department of Electrical Engineering at the Technical University of Denmark (DTU) in Kongens Lyngby, Denmark. The visit made an important impact on my research and I am grateful for all the help I received during and after the visit at DTU from Professor Mogens Blanke.

When I started my phd studies, I expected series of experiments in the laboratory and literature studies. Instead, already after a few months into my PhD, my supervisor gave me the opportunity to gain experience in the Arctic on the icebreaker CCGS Amundsen. I still remember the first time our ship encountered sea ice: I opened my eyes on a very early morning and heard a strange, erratic rumbling in the walls of my cabin. When I arrived on the bridge, I saw the endless plains of white, the enormous forces in front of the vessel that built up during ice breaking. Metres thick ice floes broke and flipped around like they were made of paper, yet it felt like a smooth flight with the ship over a landscape so fast, empty and untouched by human civilisation. After a few days I understood that this environment is not empty at all but full of life everywhere: Seals, polar bears, wales, birds, and even underneath the ice in form of plankton and immense sea-life. The Arctic is not a hostile environment, the Arctic is full of life and we are only guests.

Acknowledgments

I would like to thank Professor Roger Skjetne for serving as my supervisor and pushing me to always think a step further, patiently answering all my questions, giving constructive feedback, and for sending me to places I never thought I would visit. I would like to thank Professor Mogens Blanke for giving me inspiration, support and insight into statistical signal processing, especially during my visit at DTU and in the last months of my PhD studies. I would like to thank Professor Asgeir Sørensen for giving me all the opportunities to present my research in front of other researchers and industry partners, and for providing with NTNU AMOS, an amazing hub of innovation. I would like to thank Professor Sveinung Løset, Professor Raed Lubbad, Professor Knut Vilhelm Høyland and Dr. Wenjun Lu for explaining and showing the Arctic and the science behind sea ice to me. I would like to thank the Swedish Polar Research Secretariat, Equinor and the amazing crews of the CCGS Amundsen, Icebreaker Frej, Icebreaker Oden, and everyone involved in the experiments on Magne Viking for assisting me in collecting valuable field data for my research.

Thank you to my fellow PhD candidates and postdocs from NTNU AMOS and NTNU SAMCoT for being amazing colleagues, friends and for all the brilliant discussions around the coffee machine. Thank you Stefan Viersen for sharing the office in the beginning with me, for all the regular after-work skiing, and for listening to all my complains and problems during our monthly after-work beers. NTNUI Koiene, takk for at dere har lært meg Norsk, og for de fine turene. I am so very thankful for having a wonderful family. Hans Heyn, thank you for making me the person I am today and for watching over me. Christel Steinke-Heyn, Fritz Kuckerts, Maren Heyn, Hans-Henning Heyn, and Michelle Nerentorp, without your love, support, understanding and interest in what I do, this thesis would not exist. Therefore, I dedicate this thesis to my family.

Chapter 1

Introduction

1.1 Background and motivation

This thesis presents a technology which can increase the overall safety during operations in Arctic ice-infested waters by monitoring the ship's motion. During interaction with ice features, rigid body motion leads to a displacement of the vessel from its current position. This is measureable anywhere on the vessel. In addition, local motion (e.g. vibrations in the hull or deflections) can occur which can often only be measured close to the location of the local motion. Motion sensors, which can measure linear motion and angular motion, are already part of inertial measurement units (IMUs) on most modern vessels. By measuring both global rigid body motion and local motion at different locations of the vessel, it is the aim of this thesis to provide an additional tool that can be used, in combination with other ice monitoring systems, to provide as much information as possible about the surrounding sea ice.

Although the Arctic is a remote and inhospitable environment it has always been a destination for courageous adventurers. During the 18th and 19th century those adventurers were mainly scientists trying to explore and to map the polar regions. In the second half of the 20th century commercial and geopolitical interests arouse. Especially the discovery of major oil reserves [18] and fishing grounds in the Arctic Ocean lead to commercial operations in ice-infested waters. The potential economic opportunities and overlapping territorial claims of the United States, Canada, Greenland/Denmark, Norway and Russia made the Arctic a hotspot of geopolitical interests [66]. However, the Arctic remained throughout the 20th century an impregnable region for permanent operations. Two developments in the 21st century changed that. First, advances in technology opened new opportunities in Arctic waters. Second, and probably the main driving factor, the diminishing sea ice cover due to the effects of climate change made the Arctic region significantly more accessible [24]. This also opened new shipping routes, particularly the Northeast passage as a transport corridor for trade between Europe and Asia. A new group of adventurers also set out for the Arctic: Tourism has become a major commercial activity in the Arctic [9] and each year more tourists enter the Arctic on ice strengthened cruise boats.

Because of its inaccessibility for humans, the Arctic is one of the last remaining untouched ecosystems on Earth. With over 21.000 species of plants, fungi and animals [50], the Arctic ecosystems is one of the world's smallest but most sensitive biotopes. The Arctic Ocean is stratified, meaning that the upper layers of the ocean shows less salinity than the lower water column. During summer the upper layers become the main production area of biomass in form of highly productive phytoplankton and algal blooms under the sea ice [50]. An oil spill, for example due to a ship accident or a catastrophic fault in oil production, would interrupt the creation of biomass and subsequently interrupt the entire Arctic food chain.

Due to the lack of infrastructure in the Arctic, accidents of any kind are difficult to confine and to handle. Accidents in the Arctic are therefore at a higher risk of having major environmental and economical consequences. The presence and unpredictability of sea ice is the dominant risk factor during Arctic operations. There are two options to minimise the consequences of accidents during operations in the Arctic. The Arctic can be declared a natural habitat under protection meaning that economical activities in the Arctic are kept to an absolute minimum in order to not endanger the ecosystem. The second option is to develop technology and operation routines that minimise the remaining risk of accidents during operations in the Arctic. By introducing a method for ice condition assessment by motion sensing, this thesis aims to provide a tool for additional safety during Arctic offshore operations.

1.2 Research questions and methods

The thesis follows two aims: First, it provides a foundation on why motion measurements can be used for ice condition assessment. Second, it focuses on the application of this technology during typical operations in the Arctic.

The three sets of research questions were as follows:

1. What characterises motion measurements during operations in sea ice? Why do these characteristics in the measurements occur? How can these characteristics best be measured?
2. How can motion sensing provide additional safety during operations in the Arctic? What are the typical marine operations in sea ice that would benefit from this technology?
3. How can motion sensing be integrated into the framework of an ice observer system?

The research methodology in this thesis includes theoretical analysis, rapid control prototyping under laboratory conditions and especially full-scale testing under real Arctic conditions.

Methodology for the first set of research questions

The first set of research questions are of fundamental nature, trying to find characteristics in motion measurements that are unique under the presence of sea ice. After a first theoretical analysis, a prototype system was developed and validated under laboratory conditions. Full-scale data from a vessel operating in the Arctic

validated that there exist characteristic properties in the measurements that originate from the interaction with sea ice.

Methodology for the second set of research questions

The second set of research questions regard the application of the proposed motion sensing technology. Methods from the fields of statistical signal processing and change detection were utilised to establish a relationship between measurement characteristics and the surrounding sea ice. The aim is to provide diagnostic systems that assess and present the ice condition in a way that is easy to understand for vessel operators or that can serve as input to a decision support system. Full scale data from Arctic expeditions allowed the validation of the proposed ice monitoring system. One expedition represented the case of transit in sea ice. Another expedition represented the case of stationkeeping in sea ice. Those two operations are the most common operations on a vessel in the Arctic.

Methodology for the last research question

Based on a literature review Section 3 will explain how the proposed system can be integrated into existing methods for ice condition monitoring and assessment.

1.3 Contributions of thesis

The main contribution of this thesis is the development and validation of a novel ice monitoring system which utilises inertial measurement units on a ship[1]. The following peer-reviewed conference and journal articles spin-off this thesis:

I Conference article
Hans-Martin Heyn, Martin Knoche, Qin Zhang, Roger Skjetne (2017). **A system for automated vision-based sea ice concentration detection and floe-size distribution indication from an icebreaker**. Proceedings of the 36th International Conference on Ocean, Offshore & Arctic Engineering (OMAE 2017), Trondheim
This article presents a preliminary work to establish a ground-truth source. Optical camera systems monitored the ice conditions during ship-ice interaction and several algorithms are presented to automatically detect sea ice concentration and floe sizes in the images. The scientific contribution of this paper is the introduction of an adaptive threshold methodology to compensate for changing brightness levels on the sea ice images.

II Conference article
Hans-Martin Heyn, Roger Skjetne, Francesco Scibilia (2018). **Distributed sensing of loads acting against the hull of a stationkeeping vessel in ice**. Proceedings of the 37th International Conference on Ocean, Offshore & Arctic Engineering (OMAE 2018), Trondheim
This article introduces the concept of distributed motion sensing. The goal is to describe the general full-scale measurement setup for motion sensing on a vessel in sea

[1] or structure

ice. The article concludes with a demonstration of the system under stationkeeping in ice. The scientific contribution is the introduction of a model of a distributed motion sensing system.

III Journal article
Hans-Martin Heyn, Roger Skjetne (2018). **Time-frequency analysis of acceleration data from ship-ice interaction events**. Cold Regions Science and Technology. Published.
This article lays the foundation for the application of motion sensors for ice condition assessment. Motion data from full-scale experiments on an icebreaker transiting in ice-infested waters show that the sea ice induces vibrations with frequency peaks at the natural frequencies of the ship's hull. A detailed time-frequency analysis reveals that the excited frequencies and the amplitude of the vibrations depend on the dominant ice breaking mechanism, on the encounter velocity, and on the position of where the ice interaction against the hull occurs. The scientific contribution is the fundamental proof that motion data during ship-ice interaction can be used for the assessment of the ice conditions.

IV Journal article
Hans-Martin Heyn, Mogens Blanke, Roger Skjetne (2019). **Ice condition assessment using onboard accelerometers and statistical change detection**. IEEE Journal of Oceanic Engineering. Accepted.
This article presents the application of distributed motion sensing for online ice condition assessment during transit of a vessel in sea ice. By means of statistical signal analysis the paper presents a relationship between statistical properties of the motion signals and the surrounding ice condition. Scientific contribution are especially mathematical formulations of the log-likehood ratio, Kullback-Leibler divergence, and entropy for bivariate t-distributions and their application in a signal change detection methodology. The study concludes that the presented ice condition assessment system provides weather independent and robust additional assessment of the prevailing ice conditions.

V Journal article
Hans-Martin Heyn, Roger Skjetne (2019). **Fast onboard detection of ice drift changes under stationkeeping in ice**. Cold Regions Science and Technology. Submitted.
This article broadens the application of distributed motion sensing for the case of stationkeeping in ice. As previously presented, local ice-induced hull vibrations indirectly indicate to the ice drift direction. This phenomenon was used to develop two detectors that independently can, within a few seconds, detect changes in the ice drift direction on a vessel stationkeeping in ice. The detectors use changes in the statistical entropy and the return level of extreme values to detect changes in the ice drift. The major scientific contribution is a relationship between the statistical entropy of the motion signals and the ice drift direction. The system allows a weather independent and fast detection of the ice drift against a stationkeeping vessel in sea ice.

The following articles originate from side-projects and cooperation with other scientists and are not part of this thesis:

- Hans-Martin Heyn, Roger Skjetne (2015). **Estimation of forces caused by ship-ice interaction using onboard sensor measurements**. Proceedings of the 2015 International Conference on Port and Ocean Engineering under Arctic Conditions.
- Jon Bjørnø, Hans-Martin Heyn, Rogker Skjetne, Andreas Reason Dahl, Preben Frederich (2017). **Modeling, Parameter Identification and Thruster-Assisted Position Mooring of C/S Inocean Cat I Drillship**. Proceedings of the 36th International Conference on Ocean, Offshore & Arctic Engineering (OMAE 2017).
- Wenjun Lu, Hans-Martin Heyn, Raed Lubbad, Sveinung Løset (2018). **A large scale simulation of floe-ice fractrures and validation against full-scale scenarios**. International Journal of Naval Architecture and Ocean Engineering, vol.10.

1.4 Thesis outline and limitations

Figure 1.1 presents an overview of the chapters of this thesis. The thesis is divided into three parts. Chapters 2 to 4 form the first part and provide an introduction to the field of Arctic offshore operations and ice observer systems. The second part encompassing Chapters 5 and 6 explains the origin of the full-scale data and describes a camera system that was used to create reference data. Chapter 7 and Chapter 8 form the third part of the thesis and present the main research. Chapter 7 describes the measurement setup for motion sensing on ships and explains the underlying phenomena that allows for ice condition assessment with motion sensors. Chapter 8 presents the application of the concept of motion sensing for ice condition assessment during two typical operations in Arctic waters: Transit in sea ice and stationkeeping in sea ice.

This thesis concentrates on a monitoring system for level sea ice. It does not encompasses the dangers posed by drifting icebergs. The thesis describes and proofs the fundamental phenomena which allows for ice condition monitoring with motion sensors. However, it is not in the scope of this work to explain the detailed physical processes of ship-ice interaction beyond what is needed to understand the working principle of motion sensing in ice. The presented ice monitoring system is a prototype system and more development is required to create a marketable product.

Table 1.1: Overview of the chapters of this thesis

Introduction	Chapter 2: **Operations in the Arctic**	As introduction this chapter describes typical operations in the Arctic. It points to the challenges due to the presence of sea ice and how operators in the Arctic meet these challenges.
	Chapter 3: **Ice observer systems**	This chapter outlines the structure of an ice observer system. Because this thesis introduces a new ice monitoring system, this chapter gives an overview of already existing ice monitoring systems.
	Chapter 4: **Onboard motion sensing**	In this chapter the sensor technology for motion sensing is introduced. The chapter presents mathematical descriptions, including remarks on the notation, for single sensor and multi sensor configurations on a ship.
Data sources	Chapter 5: **Arctic expeditions and data sources**	The results of this thesis base on full-scale data collected during four cruises in the Arctic. This chapter introduces each expedition and explains the origin of the collected data.
	Chapter 6: **Creating a ground truth with optical cameras** *Article I*	A ground truth source was required to establish a relationship between ship motions and ice conditions. A peer-reviewed conference article presents a camera system with at least 12 active lenses and algorithms to extract information such as ice concentration and floe sizes.
Methods and results	Chapter 7: **Fundamentals of motion sensing for local ice condition assessment** *Articles II and III*	This chapter explains why motion sensing on ships reveals information about the local ice conditions. A first article introduces the measurement setup. A second article presents the underlying phenomena that allows motion sensing based ice condition monitoring.
	Chapter 8: **Applications of motion sensing for local ice condition assessment** *Articles IV and V*	This is the principle chapter of this thesis. Two articles describe the application of motion sensing during transit and stationkeeping in sea ice. The results from Chapter 7 is the foundation and statistical signal processing methods are presented that allow real-time ice condition assessment using solely the motion data from the sensors.

Part I

Challenges in the Arctic

Chapter 2

Operations in the Arctic

> Seier venter den, som har alt i orden
> – hell kaller man det.
> Nederlag er en absolutt følge for den, som
> har forsømt å ta de nødvendige
> forholdsregler i tide
> – uhell kalles det
>
> Roald Amundsen

Marine operations in the Arctic differ significantly from open water operations. After a brief historical perspective this chapter will give an overview of current marine activities in the Arctic and it will provide explanations why operations in the Arctic are more challenging than in open water and how these challenges are met.

2.1 A historical perspective

Scientific curiosity was and still is a driving factor for travels in Arctic[1] waters. Towards the end of the 19th century Arctic expeditions often failed because the ship hulls could not withstand the forces caused by the surrounding sea ice. Between 1872 and 1874 an Austrian-Hungarian expedition tried to find the Northeast passage in the Arctic (illustrated in Figure 2.1), and as a secondary objective to reach the geographical Northpole. The vessel *Tegetthoff* left Tromsø in July 1872 and only a month into the expedition the ship got locked in sea ice north of Novaya Zemlya. It drifted for nearly two years before it had to be abandoned due to lack of supplies. The strength of the sea ice had made it impossible to fulfil the objectives of the expedition. However, during their drift in the Arctic they made important geological discoveries such as the discovery of Franz-Josef-Land.

The *USS Jeannette* departed in August 1879 from St. Michael, Alaska for an attempt to reach the geographic Northpole by sailing into the Bering Strait. A month later, North of Herald Island in Siberia, the vessel got locked in the thickening sea

[1] and Antarctic

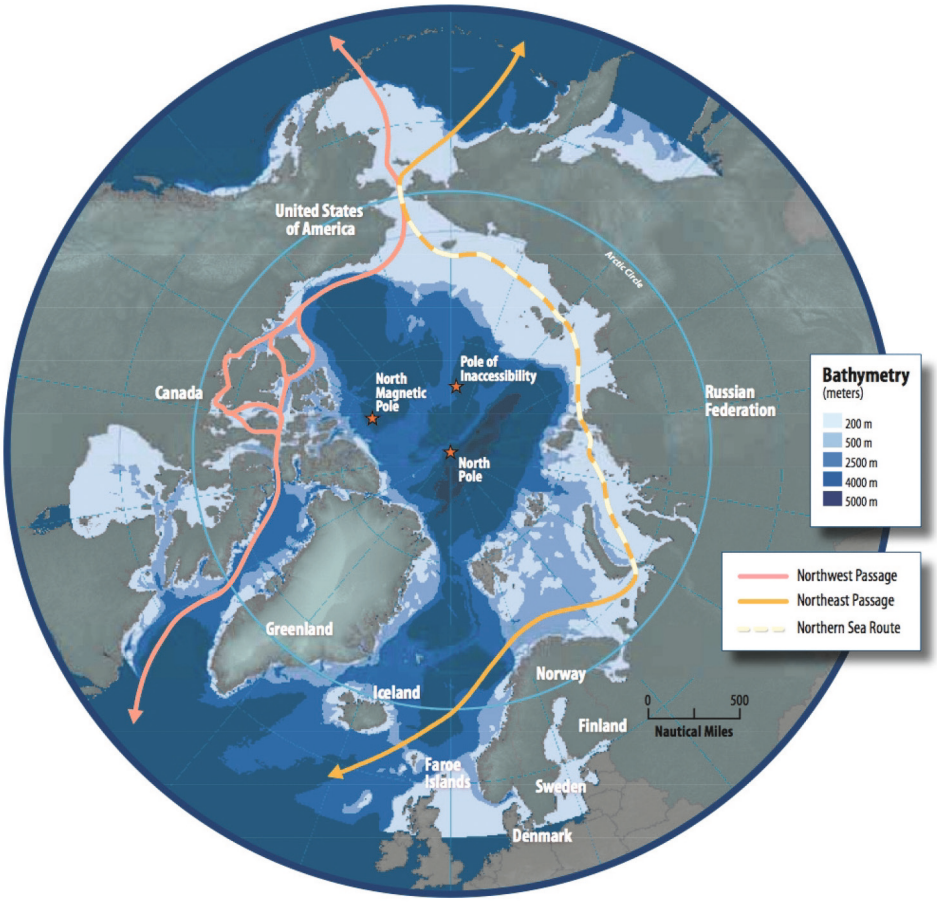

Figure 2.1: Map of the Arctic showing potential shipping routes [5]

ice. Four months later, in January 1880, the hull of the USS Jeannette was breached the first time due to ice pressure. The damage could be repaired but in June 1881, nearly two years after its departure, the hull was damaged by sea ice beyond repair and the vessel had to be abandoned.

The most successful expedition at that time was Fridtjof Nansen's expedition onboard the newly built wooden vessel *Fram* between 1893 and 1896. Nansen's expedition succeeded in reaching farther North (85°57'N) than any other ship before, although it also failed in reaching the geographic Northpole because of impenetrable sea ice. The ship Fram survived the polar ice because of it's ingenious hull design, which let the ice forces lift the vessel out of the sea instead of damaging it. The picture in Figure 2.2 shows Fram during it's third expedition which lead it to Antarctic in 1912. It took until 1977 before the first surface vessel, the Russian nuclear-powered icebreaker Arktika, could reach the geographic Northpole.

Although the presented cases are only examples of Arctic expedition, they all

Figure 2.2: Fram in Antarctic waters 1912 [3]

have in common that sea ice posed the greatest risk to the vessels.

2.2 Activities in the Arctic

Although sea ice is retreating [9] and ship design and engine power have improved significantly, the presence of sea ice still remains the major risk factor during operations in the Arctic [39]. Since the first attempts to travel in the Arctic Ocean, activities in the Arctic have increased dramatically. Today's main driver of Arctic activities are economical interests. The four main activities are [9]:

1. Arctic fisheries
2. Cargo transport
3. Tourism and science
4. Arctic offshore oil and gas exploration

All four activities require the capability of transiting in ice-infested waters or the capability of stationkeeping in ice, i.e. remaining on a fixed position in the ocean even under the influence of external forces.

2.3 Ships operating in the Arctic

Three types of ships can be distinguished that are suitable for Arctic operations [57]:

Icebreakers

They are the most capable vessels in ice. Their hull is designed to withstand all ice conditions and extremely oversized engines give them the capability of breaking sea ice of up to several metres thick. Breaking sea ice, however, is their main purpose as they have very limited cargo space. Therefore, operation costs of an icebreaker are high. They are mainly used as escort vessels for less ice-capable ships in the Arctic or for scientific purposes. Examples of icebreakers are the Russian Taymyr-class nuclear-powered icebreakers or Swedish diesel-powered Oden.

Ice going ships

These ships have the capability of sailing in sea ice without icebreaker support. Their hull is enforced and they have more power than a comparable conventional open-water vessel. In very serious ice conditions, however, these vessels can get locked in ice. They cannot compete in cargo space and economy with open water vessels which make them unattractive as cargo vessels. Ice going ships are often used as supply vessels for Arctic offshore operations and some examples are Tor Viking and Magne Viking.

Ice strengthened ships

They are designed mainly for open water operations but have a stronger hull to withstand ice pressure. As they easily can get locked in sea ice, they rely on ice observation systems. Most often these systems consist of *ice experts* on the ship or land-based institutions who provide ice forecasts. In heavy ice conditions ice strengthened vessels require icebreaker support. Most of the vessels operating in the Arctic are of the ice strengthened type. Examples are cargo vessels navigating the Baltic Sea in winter or the Northeast passage in the Arctic, Polar expedition cruise ships such as MS Roald Amundsen, or drilling, and production vessels for Arctic offshore oil and gas operations.

2.4 The danger of sea ice

2.4.1 Breaking of sea ice

Sea ice is considered hazardous when it induces a load[2] that exceeds the design or operational criteria for an exposed structure [28]. The level of sea ice load acting against a vessel's hull, sometimes referred to as *ice actions*[3], depends on the properties of the ship and the ice.

[2]Load is pressure that acts on a local area (local load) or that acts on the whole ship (global load) [39].

[3]Action is an external load applied to the structure [39].

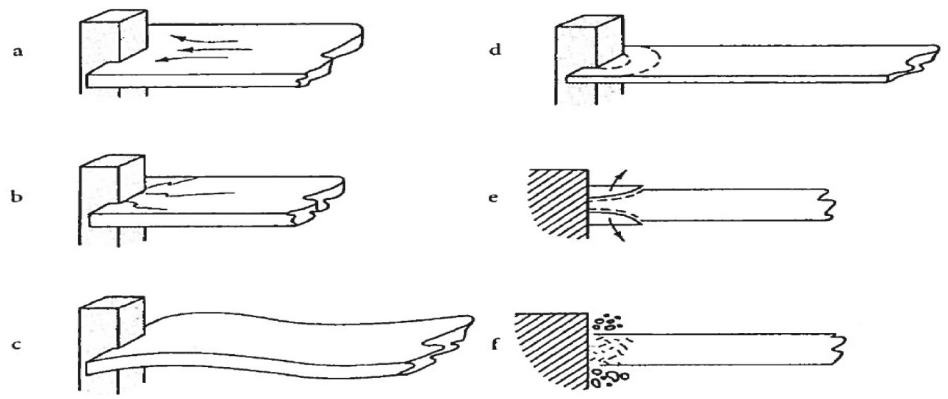

Figure 2.3: Illustration of different failure modes of ice [58]: (a) Creep, (b) Radial cracking, (c) Buckling, (d) Circumferential cracking, (e) Spalling, (f) Crushing

The most important property of the ship is the hull geometry which, when well designed, can redirect the load coming from the sea ice. This was for example the case with the earlier mentioned ship *Fram* whose hull was designed to lift the vessel upwards under ice load. Other hull features, like ice knives, allow an early breaking of the ice. An enforced hull for ice-going vessels does not abrogate all ice load, but it makes the ship more resistant against ice load.

The properties of sea ice can be classified into state variables of the ice which can change under each encounter and material properties which are constant for a given region of sea ice. State variables are encounter velocity, hull contact area, and temperature. Material properties of the ice are density, porosity, thickness, and salinity. First-year ice, for example, shows a higher porosity due to the enclosed brine pockets[4]. Multi-year ice, that is ice that withstand at least one summer, has a significantly lower porosity and is thus stronger.

Ship hull properties, state variables, and material properties of the ice govern the *failure mode* of the ice [41]. The ice load acting against the vessel depend significantly on the active failure mode [15]. Figure 2.3 illustrate six common failure modes that can occur during ship-ice interaction. Crushing of ice against a structure induces the highest load [28] because all impact energy is used to pulverise the ice without a release of pressure against the hull. Crushing typically occurs at high encounter velocities or small contact areas [58]. When ice fails by radial cracking or circumferential cracking the ice pressure against the hull is released, which results in an overall lower ice load.

The ice breaking process occurs in four steps illustrated in Figure 2.4.

1. The sea ice either drifts towards a *stationkeeping* ship, or the ship *transits* into sea ice. Either way, the impact velocity determines the initial load. When the hull gets into contact with the ice, hull and ice form an initial small contact area. A small contact area leads to initial crushing (Figure 2.3 f). As more

[4]Brine is a highly concentrated solution of salt in water

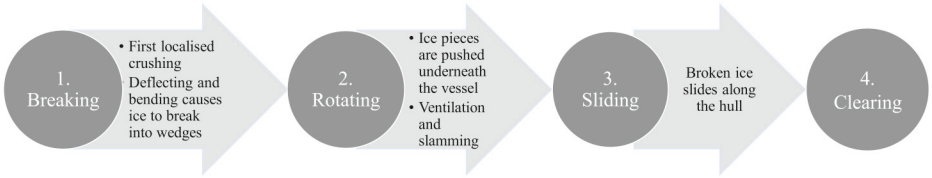

Figure 2.4: Ice-breaking process during ship-ice interaction [26]

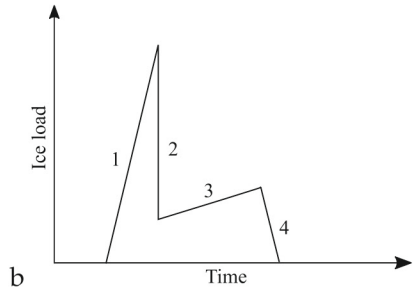

Figure 2.5: Qualitative load during breaking stages

ice keeps pushing against the hull, the ice creeps around the hull (Figure 2.3 a) and the contact area increases. The ice starts to buckle (2.3 c) and a force vertical component against the ice-sheet can build up [44].

2. When the vertical strength of the ice is reached it fails either by radial or circumferential cracking (2.3 b and d). The pressure against the hull is abruptly released and the ice pieces start to rotate and slide along the hull. Some ice pieces eventually get submerged, which can create additional loads against the hull due to ventilation and slamming [43].
3. The newly created ice pieces slide along the hull, causing friction loads.
4. Eventually the ice pieces clear off the hull or get milled in the propellers of the vessel.

The icebreaking process causes the highest loads against the vessel, as qualitatively depicted in Figure 2.5. Critical situations arise when the initial crushing process becomes the dominant failure mode because the vertical force component does not suffice for failure of the ice. In case the ice is drifting against the vessel and does not brake, it will push the vessel off position, which is especially critical during stationkeeping operations. If the vessel is in transit, the crushing of ice will take up all kinetic energy and the vessel will come to a standstill and eventually gets locked in the ice when the engine power is not sufficient to reverse the vessel out of the unbreakable ice. The vessel will then drift with the ice floe until the hull eventually fails under increasing ice pressure. To issue a warning of unbreakable ice before the ship gets locked, Chapter 8 presents a system for real-time ice condition assessment during transit.

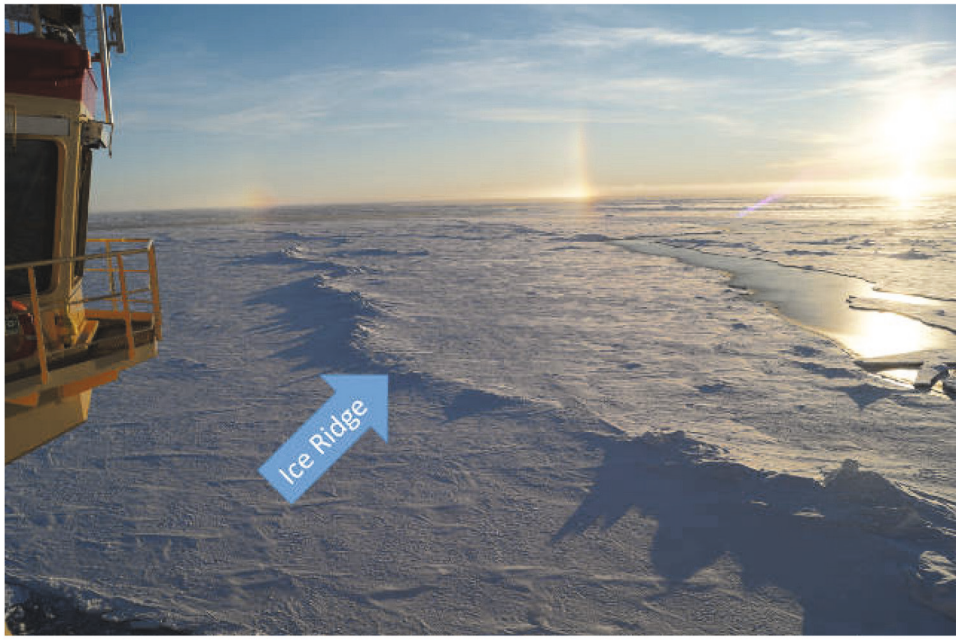

Figure 2.6: Encounter of an ice ridge during Arctic Ocean 2016 expedition

2.4.2 Ice ridges

Ice ridges pose the most severe obstacle for both transit and stationkeeping operations in the Arctic because ice ridges can cause ice loads that exceed the ship's thrust capabilities [57]. Ice ridges form under pressure by compressing of sea ice and forms a line or wall of broken ice and rubble. Typically three parts characterise an ice-ridge, as illustrated in Figure 2.7. The *keel* is formed from submerged ice rubble. Although the rubble contains major water pockets, and thus shows a low porosity, it can reach a thickness of 3-5 times the thickness of the surrounding sea ice. The thickness of the unbroken surface ice can increase by 20-100%. This thick layer of level ice is called *consolidated layer*. The *sail* of the ice ridge is the only visible feature and consist, like the keel, of ice rubble. A picture of a typical ice ridge is shown in Figure 2.6.

When a ship enters an ice ridge, the consolidated layer causes a significant increase in ice load against the ship. The increase is similar to what the ship would experience when the ice thickness suddenly increases by 20-100%. In addition to the increased level of ice load, the large amount of rubble ice under the water induces an additional load. This eventually slows a ship in transit to a total standstill or causes excessive pile up of rubble ice against a stationkeeping vessel. Furthermore, ice rubble can interact and in worst case damage propellers and the rudder.

As Figure 2.6 shows, ice ridges are difficult to spot by optical means such as the naked eye or cameras. Often it is unclear if the sail is part of an ice ridge or just some surface pile up of level ice. The increase of ice thickness due to the consolidated layer will cause an increase in ice load against the hull. By continuously

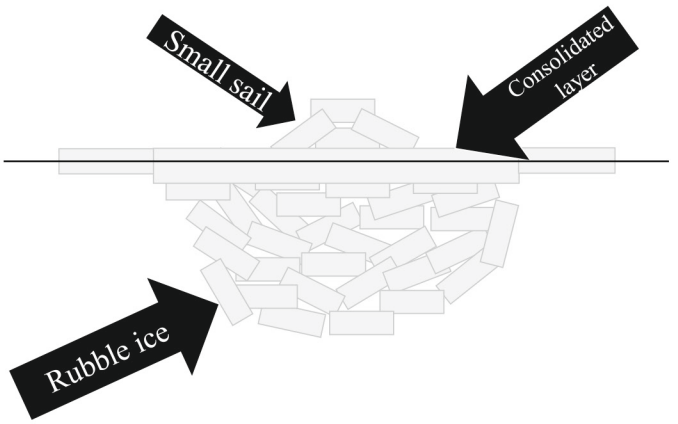

Figure 2.7: Sketch of an ice ridge

monitoring the ice load against the hull, e.g. by hull installed accelerometers as presented in Chapter 8, an early warning can be issued. The warning can in transit be used to increase the thrust or to reverse the vessel out of the ridge. Under stationkeeping, a warning can initiate a change of heading to move the bow of the vessel into the ice ridge and thus to minimise the attack surface against the hull.

2.4.3 Ice drift direction

The ice drift is governed by wind, sea-currents and kinetic effects such as the Coriolis force. The combination of these three influences make a long-term prediction of the ice drift complicated to impossible, see [23]. Figure 2.8 shows a stationkeeping operation in which a sudden, unannounced change of the ice drift is critical. The stationkeeping vessel is protected by two icebreakers. They reduce the acting ice load against the stationkeeping vessel by continuously creating an *ice channel*. The icebreakers drive in patterns through the ice, e.g. in circles. One icebreaker breaks ice floes into a diameter of several hundred metres. A second icebreaker breaks these ice floes down to a size the stationkeeping vessel can handle. Both icebreakers operate over a fixed area, and the broken ice drifts downstream against the protected vessel. If the ice drift changes, the channel of broken ice will drift into the wrong direction, leaving the protected vessel surrounded by unbroken ice if the icebreakers do not change their area of operation. Therefore, it is crucial to detect changes in the ice drift as quickly as possible and relocate the icebreakers. Chapter 8 presents a method for fast detection of ice drift changes on the stationkeeping vessel. Once a change is detected, it can be communicated to the icebreakers.

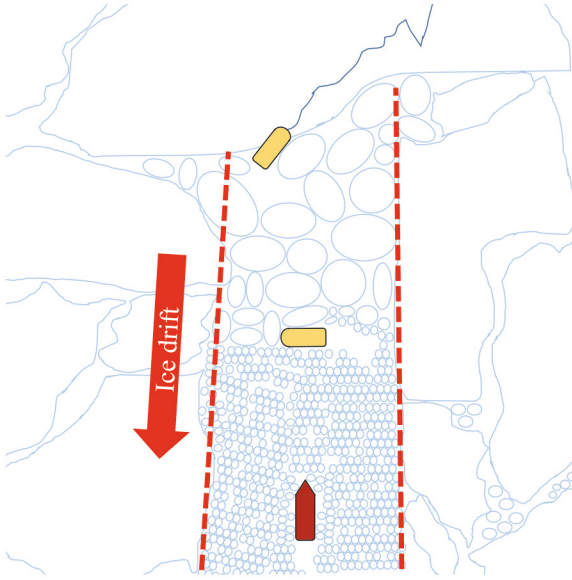

Figure 2.8: Ice channel during stationkeeping operations

2.5 Ice management systems

The earlier mentioned two icebreakers (see Figure 2.8) are part of an *ice management system*. The task of an ice management system is, as well summarised in [13]: *Ice management is the sum of all activities where the objective is to reduce or avoid actions from any kind of ice features. This will include, but is not limited to:*

- *Detection, tracking and forecasting of sea ice, ice ridges and icebergs.*
- *Threat evaluation.*
- *Physical ice management such as ice breaking and iceberg towing.*

Figure 2.9 shows the hierarchy of the three tasks of an ice management system. The ice management provides a threat evaluation based on ice information it obtained from an *ice observer system*. It further decides on the required necessary physical ice management and relays the commands to the physical ice management.

It is obvious that the ice management system requires reliable and constant ice information to function successfully. This thesis presents a novel method to gain ice information from motion sensors installed in the hull of ships. Chapter 3 will provide a deeper insight into ice observer systems.

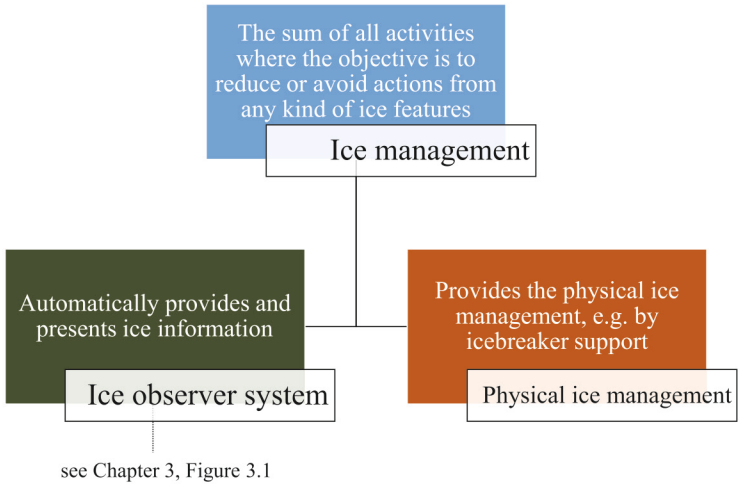

Figure 2.9: Structure of an ice management system, inspired by [13]

Chapter 3

Ice observer systems

> Nature! We are surrounded and embraced
> by her: powerless to seperate ourselves
> from her, and powerless to penetrate
> beyond her.
>
> Georg Christoph Tobler

Ice observer systems collect and process data from different ice monitoring systems. Ice monitoring systems can be divided into systems collecting local ice data and regional ice data. The border between the two regions is fuzzy in literature, however, local ice monitoring systems normally have a range of up to 15 km [13].

This chapter will systematically classify the components of an ice observer system. It will provide an overview of existing ice monitoring systems and it will argue why inertial monitoring can complement existing ice monitoring systems.

3.1 Components and hierarchy

Ice intelligence encompasses the detection, tracking, and forecasting of ice features using data provided by ice monitoring systems. Decision tasks plan the required data acquisition. Data from several ice monitoring systems are often fused to provide a more detailed ice intelligence (see for example [10, 22]). An ice observer system processes and presents the ice intelligence as ice information either to a crew of an ice-going vessel or to an ice management system. Figure 3.1 illustrates the complete hierarchy of an ice observer system.

3.2 Sensors and platforms for ice monitoring systems

Both common and experimental ice monitoring systems are illustrated in Figure 3.2. A monitoring system consists of a platform and a sensor system. The platform dictates the range, operational restrictions, and availability of data especially for regional ice monitoring systems. A camera can continuously deliver visual data of ice conditions. However, if the camera is installed on a satellite as

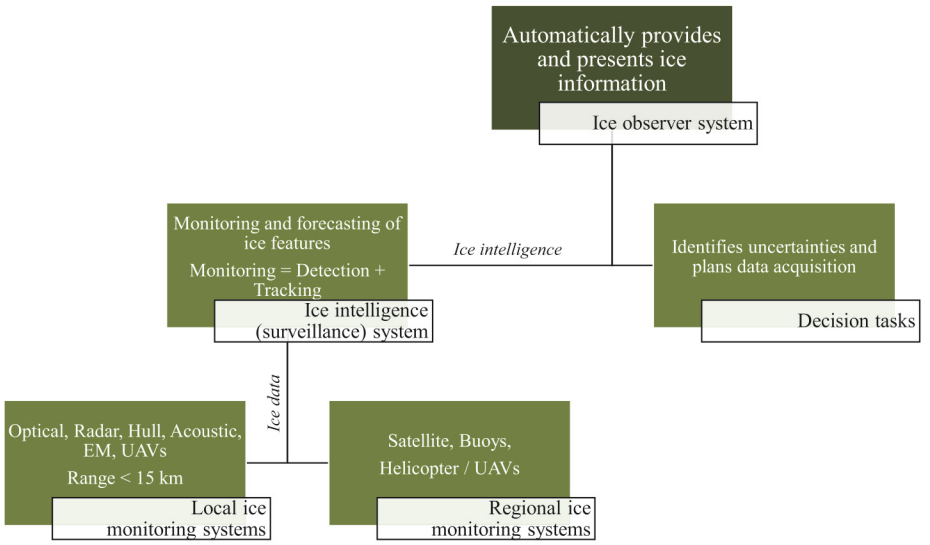

Figure 3.1: Structure of an ice observer system, inspired by [25]

platform it could only provide relevant data when the satellite flies over the operation area.

3.2.1 Platforms for regional ice monitoring systems

Typically, regional ice monitoring platforms carry optical cameras or synthetic aperture radar (SAR). Each platform has individual advantages and disadvantages:

Satellites

Space satellites are popular platforms for providing high resolution pictures or radar images of a vast area. Unfortunately, satellites can only provide data when they pass the region of interest on their orbit. Additionally, the sky must be free of disturbing clouds. Examples of the application of satellites as platform for ice monitoring can be found in [6, 8, 47, 63].

Airplanes and helicopters

Manned airplanes or helicopters serve as airborne platforms for sensors such as optical cameras or electro-magnetic (EM) ice thickness sensors [21]. They are flexible in their operation area and human experience can be used to track interesting ice features. Deployment and operation of manned airborne systems is however complex and expensive. Airplanes and helicopters both require good weather conditions for operations.

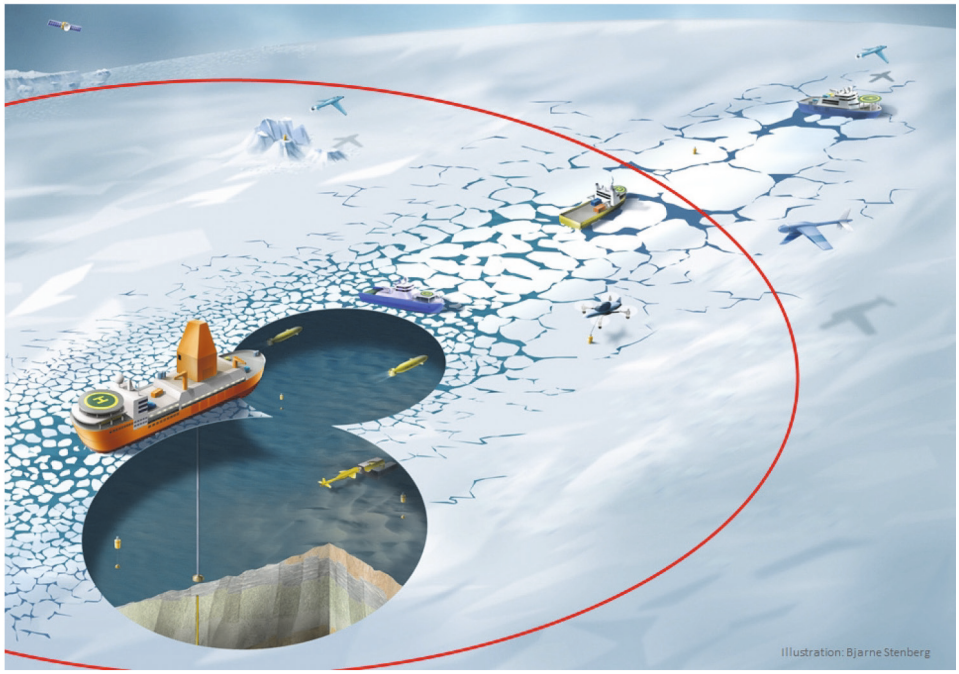

Figure 3.2: Illustration of different ice monitoring systems (Illustration: Bjarne Stenberg, Copyright: NTNU). The circle indicates the boarder between local and regional ice monitoring systems.

Ice drift buoys

Buoys provide measurements of the ice drift direction and speed by collecting GPS data while drifting with the sea ice. Some buoys have additional equipment for measuring ice thickness. Buoys can be operated independently of weather conditions. However, deployment and recovery of the buoys is not only troublesome, but also often require the use of helicopter which again can only operate under good weather conditions.

Unmanned vehicles

Both unmanned aerial vehicles (UAVs), as well as autonomous underwater vehicles (AUVs) are conceptual platforms for ice monitoring cameras. Both platforms are today not robust enough for continuous operations, but intensive research will allow operations with unmanned vehicles in the Arctic in the foreseeable future [36]. Examples for autonomous underwater vehicles used as sensor platforms for tracking ice features under the ice are demonstrated in [52]. Their operation is more or less weather independent. Another example is the development of low cost UAVs for aerial observation of sea ice [46]. Operating UAVs will be much cheaper than manned airborne platforms. However, their operations will as well be restricted by weather conditions.

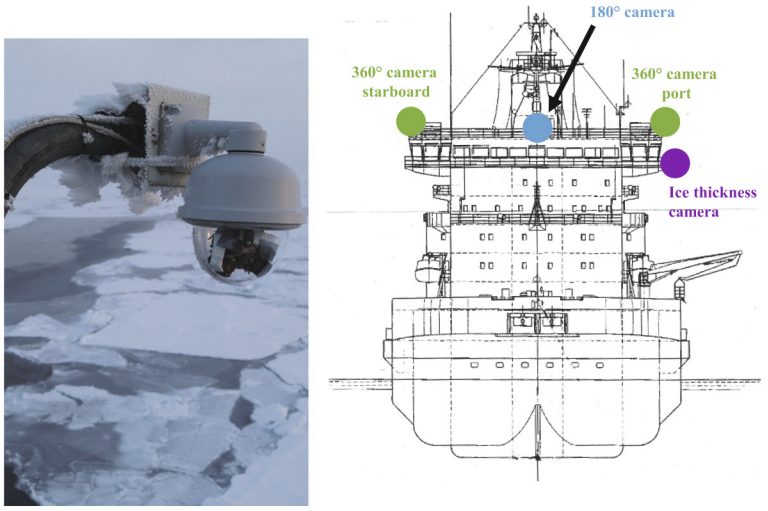

(a) 360° camera unit

(b) Typical installation points for camera units for all expeditions described in Chapter 5.

Figure 3.3: Camera system for ice condition observation

3.2.2 Sensors for local ice monitoring systems

Local ice monitoring systems are typically ship-borne. Although limited in range, ship-borne sensors can operate without platform depending restrictions. Here are some examples:

Ship's SAR

The ship's SAR, or an ice modified SAR, provides a variety of information about the surrounding sea ice. Typically, a ship-borne SAR covers an area of 2-20 km radius. Recent developments allow for the detection of ice floe size, velocity and drift direction [32]. Ship-borne SAR are especially suitable for the detection and tracking of icebergs [13]. The system works mostly independent of weather. In the near field around the vessel it might not produce reliable results because of interferences with the ship's hull.

Optical camera systems

Ship-mounted optical cameras are easy to install and operate. They require clear sight, though in contrast to airborne platforms, wind conditions do not impose restrictions to ship-mounted cameras. Besides the optical impression of the obtained ice pictures, post processing reveals significantly more information. This includes ice concentration [40, 68, 71, 72], ice thickness [42, 61], and floe size distribution [69]. A full tutorial on sea ice image processing can be found in [70].

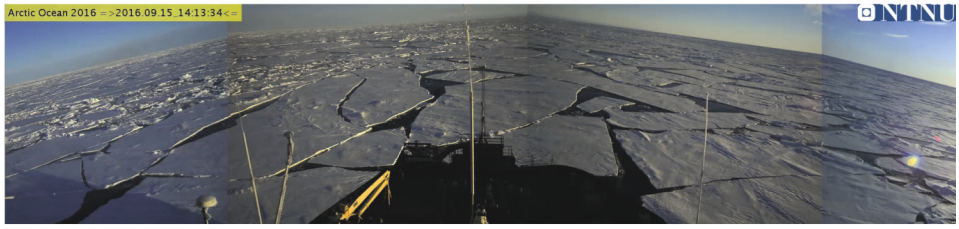

Figure 3.4: Example image from the 180° camera system

A ship-borne camera system, and subsequent post processing, provided some ground-truth about the ice conditions in this thesis. A detailed description is provided in Chapter 6. Basically, a 360° camera system provides images of the surrounding ice conditions, see Figure 3.3a. Additional 180° cameras provide panoramic images of the ice condition ahead or behind the vessel, as shown in Figure 3.4. An ice thickness camera captures images of rotating ice floes. Together with a length reference, e.g. a measurement stick mounted on the side of the vessel, the estimation of ice thickness is possible. A typical setup of the different cameras is illustrated in Figure 3.3b. Each camera unit of the 360° and 180° cameras contains several lenses allowing a wide field of view. A detailed explanation of the 360° camera system used in this thesis is given in Chapter 6. The 180° and ice thickness cameras are presented in [42].

Strain gauges

Strain gauges along baring frames of the hull provide a measure of ice pressure against the hull by assuming a relationship between the measured sensor response and the local load against that frame [55]. In contrast to previously mentioned sensors, strain gauges provide a measure of the imminent local load acting against the vessel, see for example [34, 35]. Their installation and calibration is laborious, which is why often only a few frames are equipped with strain gauges. Several classification societies recommend strain gauges for ice load measurements [2, 11, 12]. Figure 3.5 shows a picture of the installation of strain gauges on the vessel Magne Viking.

Motion sensors

An alternative approach for ice load measurements are acceleration sensors. Johnston et al. presented and validated a sensor system containing a triaxis accelerometer for global ice-induced load determination [29, 30]. Based on the observability of linear motion quantities in navigation systems [7] and the necessary number of accelerometer for 6 degree-of-freedom (6DOF) acceleration reconstruction [67], Kjerstad et al. extended the single sensor approach to a distributed motion sensor network for global ice load estimation [32]. Motion sensors are significantly easier to install and maintain than strain gauges. Two motion sensors are shown in Figure 3.6. Chapter 4 provides a detailed description of motion sensing for ice monitoring purposes.

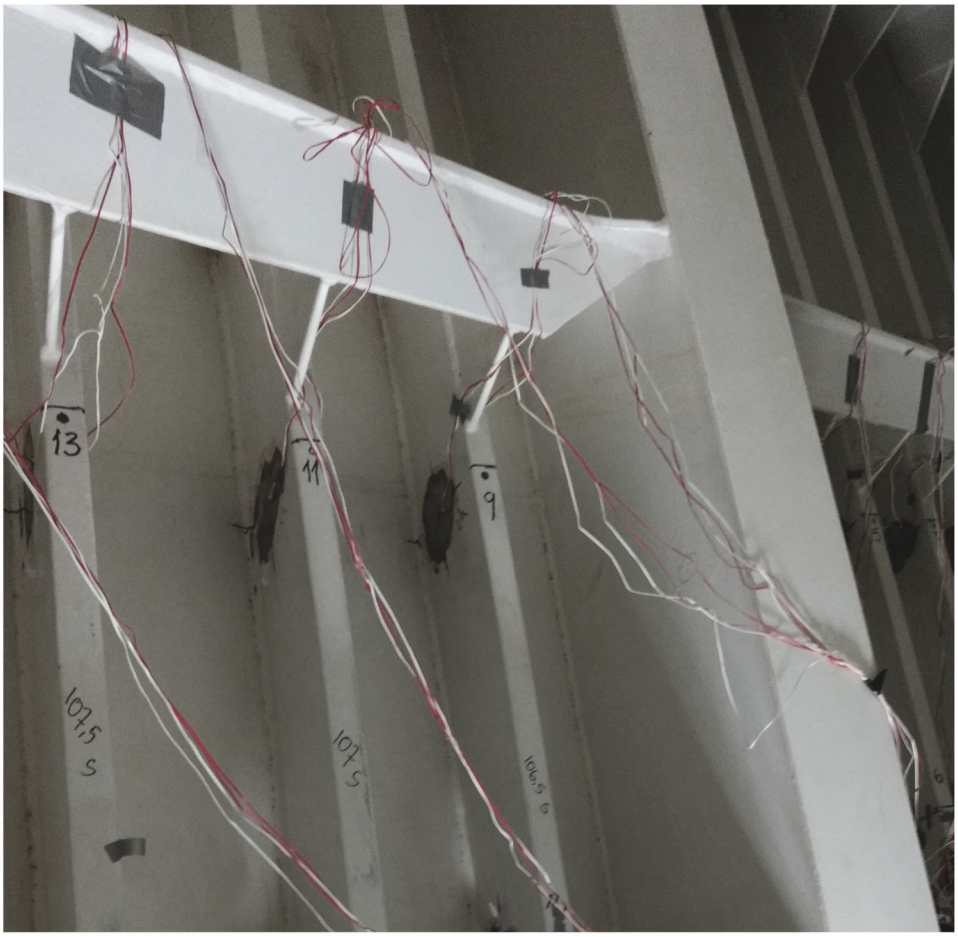

Figure 3.5: Strain gauges installation on Magne Viking

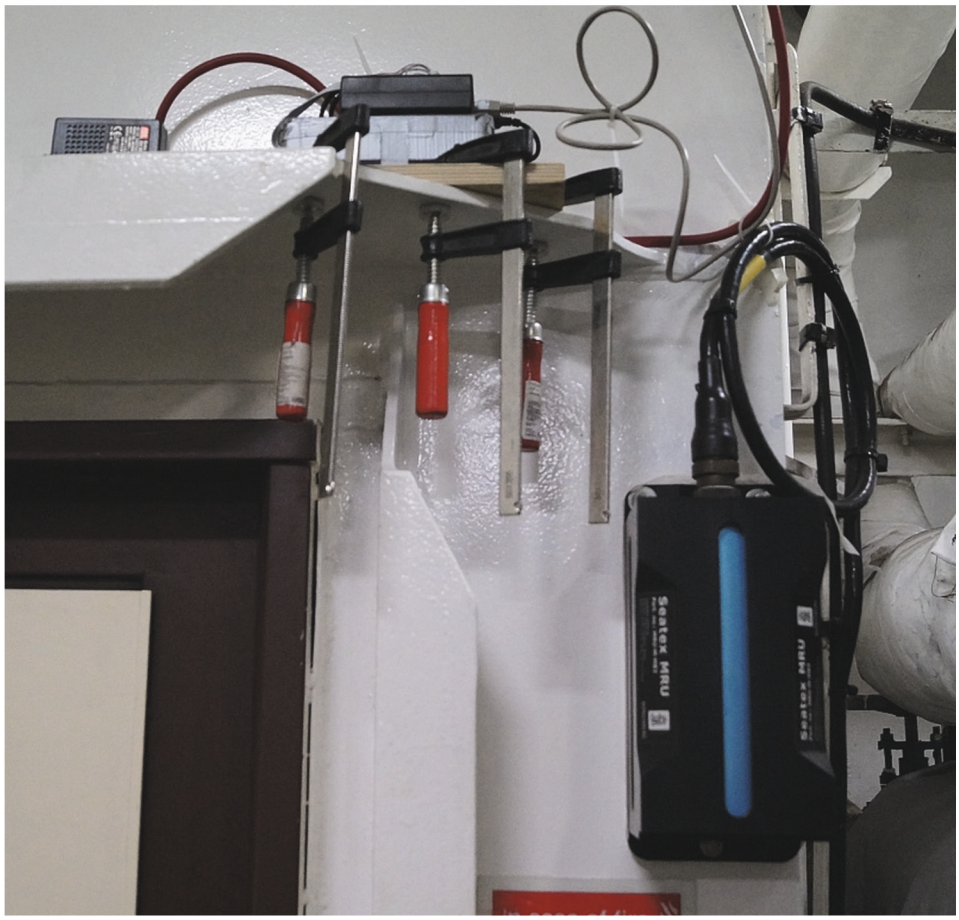

Figure 3.6: Two motion sensors on IB Oden (left: Prototype system (see Chapter 7), right: Commercial system from Kongsberg)

Chapter 4

On-board motion sensing

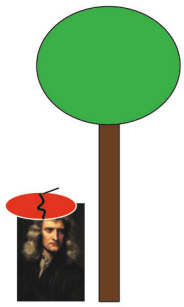

Lex I: Corpus omne perseverare in statu suo quiescendi vel movendi uniformiter in directum, nisi quatenus a viribus impressis cogitur statum illum mutare.
Lex II: Mutationem motus proportionalem esse vi motrici impressae, et fieri secundum lineam rectam qua vis illa imprimitur.

Sir Isaac Newton

Motion sensing depends on Newton's first and second laws of motion. The first law states that a body changes its state of motion only upon the influence of an external force on it. In an inertial reference frame the law is in principle easy to understand. It gets more complicated if one looks at the Earth's reference frame with gravity and fictitious forces acting on objects.

This chapter will give an introduction to motion sensing with inertial measurement units (IMUs) and an outline of how to measure linear accelerations and angular velocities on a body in motion. It will further describe the measurement model used throughout this thesis.

Definition 4.1. Inertial reference frame: *In an inertial reference frame a body with zero net force acting upon it is not accelerating* [14]. *It remains at rest or is moving at constant speed in a straight line.*

The second law of motion states that acceleration is always proportional to the acting force and that it is in the same direction. The proportional factor is the mass of the object.

Mathematically, this means

$$F = m \cdot a, \tag{4.1}$$

with F being the net force, m the mass of a body, and a the acceleration experienced by the body.

4.1 Notation

Throughout the thesis the following notation is applied:

- A subscript to a vector $\boldsymbol{x} \in \mathbb{R}^3$ gives a reference to a coordinate reference frame.
- A position vector $\boldsymbol{p}_{ab}^{c} \in \mathbb{R}^3$ represents the position seen from the origin of frame $\{a\}$ to the origin of frame $\{b\}$ decomposed along the coordinates of frame $\{c\}$.
- A translational velocity vector $\boldsymbol{v}_{ab}^{c} \in \mathbb{R}^3$ or an acceleration vector $\boldsymbol{a}_{ab}^{c} \in \mathbb{R}^3$ represents the translational velocity or acceleration of frame $\{b\}$ relative to frame $\{a\}$ decomposed in frame $\{c\}$.
- An Euler angle vector $\boldsymbol{\Theta} \in \mathcal{S}^3$ describing the angles from $\{a\}$ to $\{b\}$ is denoted $\boldsymbol{\Theta}_{ab}$.
- A rotation matrix $\boldsymbol{R}_{c}^{d} \in \mathcal{SO}(3)$ transforms a vector from frame $\{c\}$ to frame $\{d\}$. This can be parameterised by an Euler angle vector $\boldsymbol{R}(\boldsymbol{\Theta}_{cd})$ where $\boldsymbol{R}(\cdot)$ is a rotation matrix[1] defined as

$$\begin{aligned}\boldsymbol{R}(\boldsymbol{\Theta}_{cd}) &= \boldsymbol{R}_{z,\psi}\boldsymbol{R}_{y,\theta}\boldsymbol{R}_{x,\phi} \\ &= \begin{bmatrix} \mathrm{c}(\psi)\,\mathrm{c}(\theta) & -\mathrm{s}(\psi)\,\mathrm{c}(\phi) + \mathrm{c}(\psi)\,\mathrm{s}(\theta)\,\mathrm{s}(\phi) & \mathrm{s}(\theta)\,\mathrm{s}(\phi) + \mathrm{c}(\psi)\,\mathrm{c}(\phi)\,\mathrm{s}(\theta) \\ \mathrm{s}(\psi)\,\mathrm{c}(\theta) & \mathrm{c}(\psi)\,\mathrm{c}(\phi) + \mathrm{s}(\phi)\,\mathrm{s}(\theta)\,\mathrm{s}(\psi) & -\mathrm{c}(\psi)\,\mathrm{s}(\phi) + \mathrm{s}(\theta)\,\mathrm{s}(\psi)\,\mathrm{c}(\phi) \\ -\mathrm{s}(\theta) & \mathrm{c}(\theta)\,\mathrm{s}(\phi) & \mathrm{c}(\theta)\,\mathrm{c}(\phi) \end{bmatrix}\end{aligned} \tag{4.2}$$

- The derivation of a rotation matrix $\dot{\boldsymbol{R}}_{c}^{d} = \boldsymbol{R}_{c}^{d}\boldsymbol{S}(\boldsymbol{\omega}_{dc}^{c})$, where $\boldsymbol{S}(\boldsymbol{\omega}_{dc}^{c})$ is a skew-symmetric matrix which depends on the angular vector $\boldsymbol{\omega}_{dc}^{c}$, is given as

$$\boldsymbol{S}(\boldsymbol{\omega}) = \begin{bmatrix} 0 & -\omega_z & \omega_y \\ \omega_z & 0 & -\omega_x \\ -\omega_y & \omega_x & 0 \end{bmatrix} \tag{4.3}$$

Definition 4.2. Skew-symmetric matrix: *A skew-symmetric matrix* $\boldsymbol{S}(\boldsymbol{\omega}^a)$ *with* $\boldsymbol{\omega}^a \in \mathbb{R}^3$, $\boldsymbol{\omega}^b \in \mathbb{R}^3$, *and* $\boldsymbol{R}_{a}^{b} \in \mathcal{SO}(3)$ *has the following property:*

$$\boldsymbol{R}_{a}^{b}\boldsymbol{S}(\boldsymbol{\omega}^a)\boldsymbol{R}_{b}^{a} = \boldsymbol{S}(\boldsymbol{R}_{b}^{a}\boldsymbol{\omega}^a) = \boldsymbol{S}(\boldsymbol{\omega}^b) \tag{4.4}$$

[1] In (4.2) $\mathrm{s}(\cdot)$ and $\mathrm{c}(\cdot)$ denote the sine-cosine-functions.

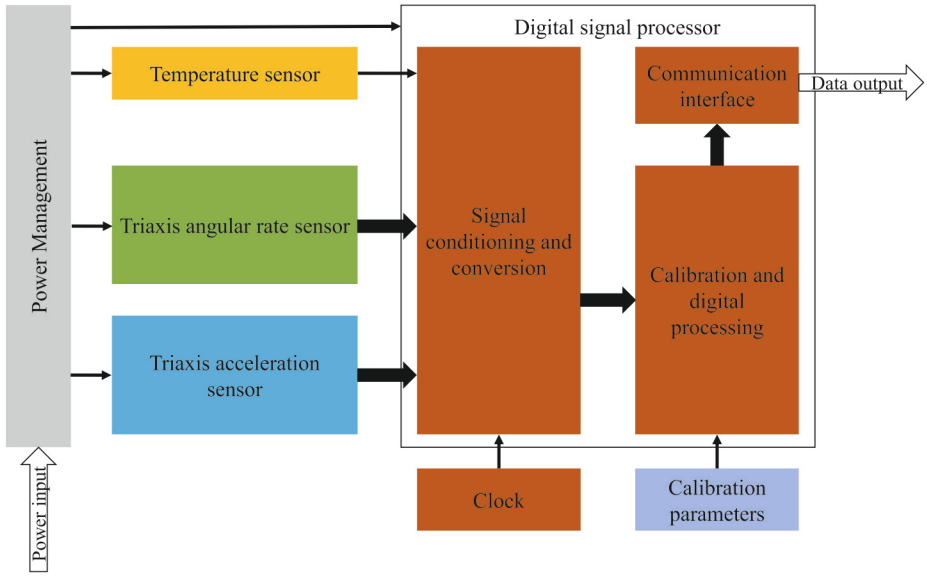

Figure 4.1: Schematic of a typical IMU (with elements from [4] and [20]).

4.2 Principle of IMU technology

An IMU is a suite of typically[2] three orthogonally arranged accelerometers and typically three orthogonally arranged gyros. The accelerometers measure linear motion in all spatial directions, and the gyros measure angular motion around the spatial axes. The axes of both sensor triads are fixed to the sensor's body axis, which throughout the thesis will be referred to as *sensor frame* $\{s\}$. Figure 4.1 gives an illustration of the schematic and data flow of a typical commercial IMU. Besides the inertial sensors, an IMU contains systems for power management, signal processing units, calibration routines, a digital clock, and a communication interface. A temperature sensor allows for the removal of temperature related bias drifts [53]. To reduce systematic errors, a calibration of the IMU [4] is conducted after the manufacturing process. The calibration parameters are stored internally on a rewriteable memory and allows the signal processor to correct the sensor measurements. To prevent resonance effects, the components inside an IMU are damped with vibration isolators [20]. The typical output signal rates range between 100 Hz - 1000 Hz [19]. IMUs can be rated mainly depending on their bias drift. There is however no standardised rating scheme for IMUs. In [20], Groves presents a good graduation of IMUs depending on accelerometer and gyro biases, which has been reproduced in Table 4.1. The IMUs used in this thesis range as *Intermediate* to *Aviation* grade on this scale.

[2]Some IMUs contain additional sensors in a skew configuration to allow single-sensor failures [20]

Table 4.1: Gradation of IMUs depending on their inertial sensors' biases [20]

IMU grade	Accelerometer bias (mg)	Gyro bias ($^\circ h^{-1}$)
Marine	0.01	0.001
Aviation	0.03 - 0.1	0.01
Intermediate	0.1 - 1	0.1
Tactical	1 - 10	1 - 100
Consumer	>3	>100

4.2.1 Sensor errors

Accelerometers and gyros show several types of errors during operation. Most dominant are bias errors, scale-factor errors, cross-coupling errors and errors due to random noise [19, 20]. The magnitude of the errors are either fixed throughout the lifetime of the sensor, are temperature depending, change upon activation of the sensor but remain constant during the measurements (run-to-run variation) or change slowly during the measurements (in-run variation) [20]. Factory calibration removes the fixed error components. The temperature related error components are removed within the IMU by measuring the temperature and correcting for the temperature error. The remaining two error components cannot be removed by the signal processor inside the IMU. The four main sources of measurement error will be depicted as follows. Additional errors are described in [19, 33].

Biases

Slowly changing biases are the largest source for measurement error [19]. Especially in strap-down navigation systems, the biases in the accelerometers cause a fast drift of any position estimate.

Scale-factor

The scale factor is the error between input and output, which is often a linear relationship. A 10000 ppm error would cause an output signal of $10.2\ m \cdot s^{-2}$ for a measured acceleration of $10\ m \cdot s^{-2}$ [54].

Cross-coupling

Cross-coupling causes an accelerometer to react on an, to its sensitive axis, orthogonal acting acceleration due to misalignment or vibrations in the casing. This often occurs in low-priced consumer IMUs [20].

Noise

All sensor systems experience influences from random noise. Both mechanical vibrations and noise in the electrical system cause a noise, which is normally approximately Gaussian in character. The root power spectral density (PSD) prescribes the noise characteristics of the sensor, with units of micro-gs per square

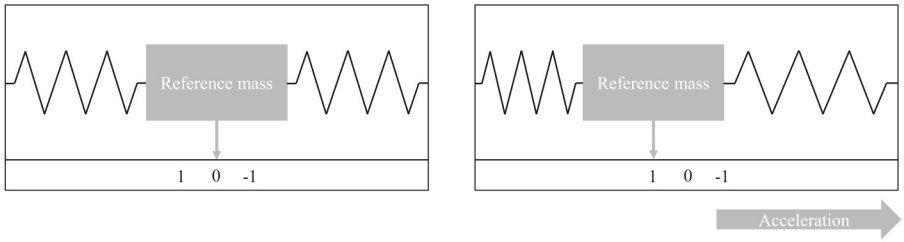

Figure 4.2: Principle of an accelerometer [53]

root of a hertz for accelerometers, and *rad* per square root of an hour for gyros [20]. The noise standard deviation can be calculated by multiplying the PSD with the sampling rate. An example is given in [20]: If an accelerometer has a noise PSD of $100\ \mu g/\sqrt{\text{Hz}}$, and the sampling rate is 400 Hz, then the corresponding noise standard deviation will be $2\ mg$.

4.2.2 Accelerometers

Figure 4.2 illustrates the functional principle of an accelerometer. The left illustration shows an accelerometer at rest without an external force acting on it. Two springs suspend a proof mass along a sensitive axis at an equilibrium point inside the accelerometer's casing. The inertia of the proof mass will cause a displacement of the proof mass inside the casing if a force accelerates the casing along the sensitive axis (see right illustration in Figure 4.2). The displacement is proportional to the acceleration. The distance from the equilibrium can be measured and converted into an electric signal. Note that an acceleration of the accelerometer to the right will cause a displacement of the proof mass to the left.

Accelerometers in this configuration cannot measure gravitational acceleration. A gravitational field acts on all components of the accelerometer, meaning that the casing, the springs, and the proof mass will be displaced equally resulting in no relative motion of the proof mass with respect to the casing [53]. An accelerometer in a gravity field during free fall will therefore produce a measurement output of $\mathbf{0}$. Assume however that the casing rests on a bench in a gravitational field of $1\ g$ pointing downwards into the same direction as the sensitive axis of the sensor. The proof mass in this case will be pulled downwards resulting in a permanent acceleration signal of -1 g. This often causes confusion as the signal shows the opposite of the gravitational acceleration. Humans perceive acceleration and gravity in a similar way. While we can feel accelerations acting on our body, e.g. in a roller-coaster, we perceive gravity only as weight which is caused by a force opposing gravity. During free-fall our body feels *weightless*, although there is a force that accelerates our body into the direction of gravity. The measurement output of an accelerometer is called *specific force*[3]. For a triaxis accelerometer with sensor frame

[3] or in some literature *proper force*

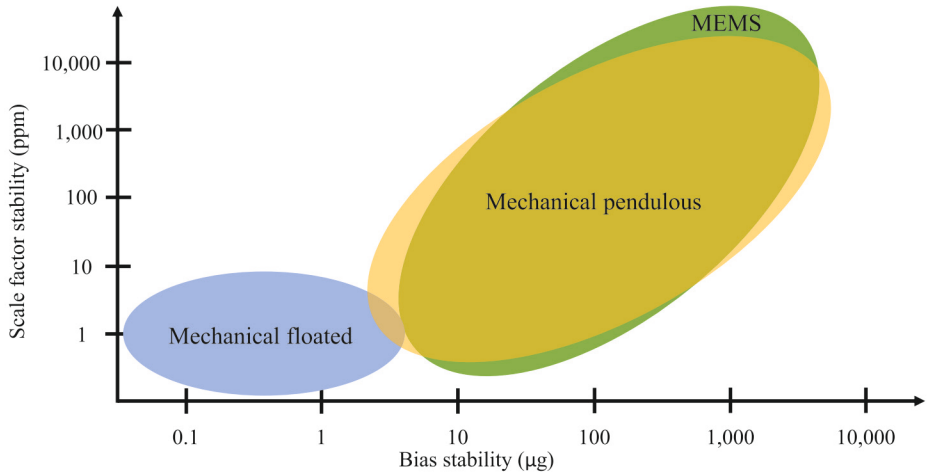

Figure 4.3: Technology and performance of IMU accelerometers [59]

$\{s\}$ in an inertial reference frame $\{i\}$ the specific force is given by

$$\boldsymbol{f}_s^s = \boldsymbol{a}_{\boldsymbol{is}}^{\boldsymbol{s}} - \boldsymbol{R}_i^s \bar{\boldsymbol{g}}^{\boldsymbol{i}}, \tag{4.5}$$

where $\boldsymbol{a}_{\boldsymbol{is}}^{\boldsymbol{s}} \in \mathbb{R}^3$ is an acceleration with respect to $\{i\}$ and $\bar{\boldsymbol{g}}^{\boldsymbol{i}} = [0, 0, g]^\top$ with $g = 9.80665\ \mathrm{m{\cdot}s^{-2}}$, is the gravitational vector in the inertial frame.

Different technologies allow for different precision and price tags for accelerometers. Traditional mechanical solutions allow for a high bias stability and scale factor stability especially when the mechanical parts float in a suspension liquid. In pendulous accelerometers the proof mass is supported by a pendulous arm which can swing along the sensitive axis. Additional damping and force feedback solutions can increase the precision of pendulous accelerometers. Recently, microelectromechnanical systems (MEMS) have allowed for a drastic miniaturisation and cost reduction of accelerometers. The most common MEMS design are vibrating beam accelerometers. The proof mass is again mounted on a pendulum, which is supported by typically two vibrating beams. When a force acts on the proof mass it compresses one beam and pulls on the other beam which in response changes their resonance frequencies. The changes in resonance frequency for each beam are measured and converted into an electrical signal indicating the acting force on the proof mass. Figure 4.3 shows the performance in terms of bias and scale-factor error stability for different accelerometer technologies. MEMS based accelerometers nowadays reach a similar performance as non-floating mechanical accelerometers. Floated mechanical accelerometers are still superior to MEMS based accelerometers. However, it is expected that new technologies such as cold-atom interferometry will outperform classical mechanical systems in the near future [49].

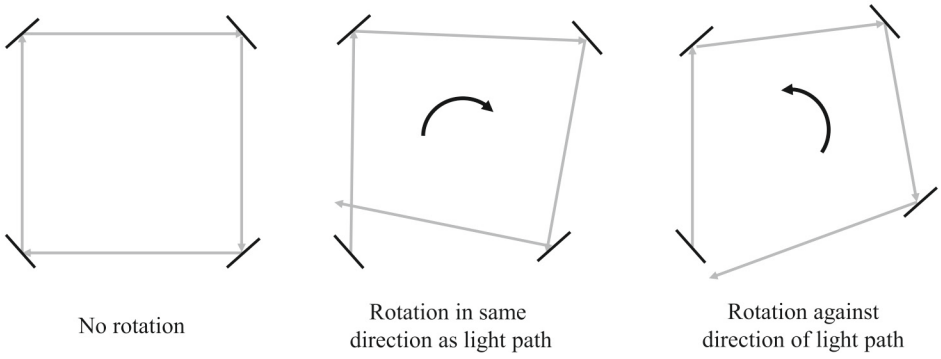

Figure 4.4: Principle of an optical gyro (reproduced from [19])

4.2.3 Gyroscopes

Gyroscopes measure the angular rate in degrees per second or rad per second. Gyros are either mechanical based, optical based, or a MEMS. Because gyros do not play a significant role in this thesis, besides measuring the attitude of the vessel, their function will only be outlined.

Mechanical gyros measure changes in angular momenta of a spinning proof mass. Because these devices are very bulky and include rotating parts they are not in common use anymore.

Higher precision, and a less bulky design is given with optical based gyros. The concept is illustrated in Figure 4.4. Optical gyros base on the *Sagnac effect*. Light travels at a constant speed in an inertial frame. The light travels a path consisting of several mirrors placed equidistantly to each other. At rest the path travelled by the light between each mirror is equal. If the light path rotates in the same direction as the light travels in it, the path length for the light will slightly increase. If the light path rotates against the direction of light travel, the path will slightly decrease. The rotational rate can be evaluated by measuring the change of distance travelled by the light.

MEMS gyros are vibratory gyros. They contain a vibrating element which can vibrate along two directions and is fixed along the third direction. Along one of the free directions a vibration is externally induced. If the element is rotated around the fixed axis, *Coriolis acceleration* will induce a vibration in the second free axis which is not externally driven. The amplitude of this induced vibration depends on the angular rate [20]. Depending on the quality of the gyro, the vibrating mass is either made of quartz for high-end gyros or silicon for consumer grade gyros for e.g. mobile phones.

The output of a triaxis gyro is $\boldsymbol{\omega}_{is}^{s}$, where the subscript indicates that the measurements are taken in the sensor frame $\{s\}$ in relation to an inertial frame $\{i\}$, and the subscript states that the measurements are expressed in the sensor frame orientation $\{s\}$.

4.3 Coordinate frames

Depending on where the measurements are taken and on the required relation to some reference, different coordinate frames are in use. A coordinate frame is used to describe the position and motion of an object in relation to another object or reference.

Sensors of an IMU produce measurements relative to an inertial frame described in the sensor's reference frame, i.e. resolved along the instrument's sensitive axes [53]. There are two groups of reference frames: Earth-centred reference frames and local reference frames. Local reference frames are illustrated in Figure 4.5.

4.3.1 Global coordinate systems

Earth-centred-inertial frame (ECI)

The ECI frame is an inertial frame. The origin is at the centre of mass of Earth. The z-axis is along the rotation axis of Earth and points towards the terrestrial Northpole. The x-axis points towards the vernal equinox which is the direction of intersection of the equatorial plane with the plane of Earth's orbit around the sun [53]. The y-axis lies orthogonal to the other two axes. The coordinate system is non-rotating which makes it difficult to describe the position of stationary objects on the surface of Earth. The ECI frame is referred to as frame $\{i\}$.

Earth-centred-earth-fixed frame (ECEF)

The introduction of a rotating coordinate frame remedies the problem of describing a stationary object on the surface. The ECEF frame is a rotating coordinate system with its origin at the centre of mass of Earth. The z-axis coincides with the z-axis of the ECI frame. The x-axis points towards the intersection of the equatorial plane and the Greenwich meridian. The y-axis completes the right-hand orthogonal coordinate system. While the z-axis is fixed, the x- and y-axes rotate in the direction of the Earth's rotation with the Earth's rotation rate $\boldsymbol{\omega}_{ie}^{e} = [0, 0, \omega_e]^\top$, with $\omega_e = 7.2921 \cdot 10^{-}5$ rad/s. The ECEF frame is referred to as frame $\{e\}$.

4.3.2 Local coordinate systems

North-east-down frame (NED)

The NED frame is a local reference frame which describes an object's attitude and position on, or close to, the surface of Earth [53]. The centre of the coordinate system is at some chosen point. The surface of Earth is assumed to be flat in the local area around the centre of the NED frame. The z-axis points downwards towards the centre of Earth. The x-axis points towards the geographic Northpole. The y-axis completes a left-hand orthogonal coordinate system, thus pointing towards east. The NED frame can be described relative to the ECEF frame with two coordinates: *latitude* and *longitude*. The NED frame is referred to as frame $\{n\}$.

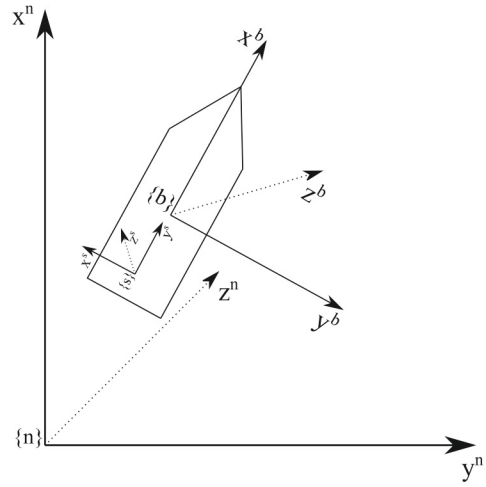

Figure 4.5: Definition of local reference frames

Body frame

The body frame's coordinate system coincides with the principal axes of the vehicle. It is a local frame with the origin at the centre of gravity or the centre of orientation of the vehicle. The z-axis points down. A rotation around the z-axis is called yaw. The x-axis points straight ahead. A rotation around it is called roll. The y-axis points to the right / astarboard and a rotation around it is called pitch. The body frame is referred to as frame $\{b\}$.

Sensor frame

A vehicle can be equipped with several motion detecting sensors, and often it is not possible to align their sensitive axes with the body frame. The sensors therefore haves their own reference frames with the centre and orthogonal sensitive axes defined by the manufacturers. It follows the same conventions as the body frame with another orientation. Both the sensor and body frames can be transformed to the NED frame by using (4.2). The sensor frame is referred to as frame $\{s\}$ or as frame $\{s_i\}$, with i indicating the sensor number.

4.4 Modelling of single sensor configuration

The triaxis accelerometer and the triaxis gyro of an IMU output specific forces $\boldsymbol{f}_s^s$ and angular rates $\boldsymbol{\omega}_s^s$ in the sensor's reference frame $\{s\}$. A rotation matrix $\boldsymbol{R}_b^s$ describes the orientation of the sensor frame in relation to the body frame. The specific force readings can be transferred to the body frame of the vessel:

$$\boldsymbol{f}_s^b = \boldsymbol{R}_s^b \boldsymbol{f}_s^s. \tag{4.6}$$

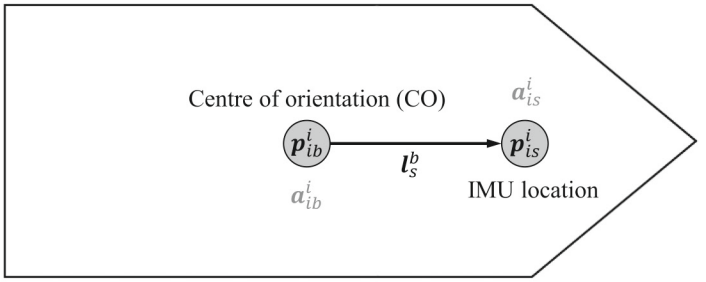

Figure 4.6: Position of a single IMU in relation to the centre of orientation (CO)

It is further assumed that the axes of the sensor are aligned[4] with the body frame. Assume that only a (slow changing) bias $\boldsymbol{b}^b_{a_s}$ and noise $\boldsymbol{w}^b_{a_s}$ remain for the triaxis accelerometer and $\boldsymbol{b}^b_{\omega_s}$ and $\boldsymbol{w}^b_{\omega_s}$ for the triaxis gyro as error components after calibration. The specific force readings include sensed acceleration with respect to an inertial frame $\boldsymbol{a}^b_{is} = \boldsymbol{R}^b_i \ddot{\boldsymbol{p}}^i_{is}$ and a gravitational component $\bar{\boldsymbol{g}}^i$. Together with the error components, the triaxis accelerometer outputs

$$\boldsymbol{f}^b_s = \boldsymbol{a}^b_{is} - \boldsymbol{R}^b_i \bar{\boldsymbol{g}}^i + \boldsymbol{b}^b_{a_s} + \boldsymbol{w}^b_{a_s}, \tag{4.7}$$

and the triaxis gyro outputs:

$$\boldsymbol{\omega}^b_s = \boldsymbol{\omega}^b_{ib} + \boldsymbol{b}^b_{\omega_s} + \boldsymbol{w}^b_{\omega_s}. \tag{4.8}$$

The IMU sensor is not necessarily placed in the vessel's centre of orientation[5]. Instead, it is placed at a lever arm $\boldsymbol{l}^b_s \in \mathbb{R}^3$ away from the CO, as illustrated in Figure 4.6. Assume the centre of orientation is at position $\boldsymbol{p}^b_{ib}$. The position of the sensor in relation to the inertial frame $\{i\}$ is then [60]

$$\boldsymbol{p}^i_{is} = \boldsymbol{p}^i_{ib} + \boldsymbol{R}^i_b \boldsymbol{l}^b_s. \tag{4.9}$$

The vessel's inertial velocity $\boldsymbol{v}^b_{ib} = \boldsymbol{R}^b_i \boldsymbol{p}^i_{ib}$ is given by

$$\begin{aligned} \dot{\boldsymbol{p}}^i_{is} &= \dot{\boldsymbol{p}}^i_{ib} + \dot{\boldsymbol{R}}^i_b \boldsymbol{l}^b_s && (4.10)\\ &= \boldsymbol{v}^i_{ib} + \boldsymbol{R}^i_b \boldsymbol{S}(\boldsymbol{\omega}^b_{ib}) \boldsymbol{l}^b_s && (4.11)\\ &= \boldsymbol{R}^i_b \left(\boldsymbol{v}^b_{ib} + \boldsymbol{S}(\boldsymbol{\omega}^b_{ib}) \boldsymbol{l}^b_s \right). && (4.12) \end{aligned}$$

The vessel's acceleration is derived as

$$\begin{aligned} \ddot{\boldsymbol{p}}^i_{is} &= \dot{\boldsymbol{v}}^i_{ib} + \dot{\boldsymbol{R}}^i_b \boldsymbol{S}(\boldsymbol{\omega}^b_{ib}) \boldsymbol{l}^b_s + \boldsymbol{R}^i_b \boldsymbol{S}(\dot{\boldsymbol{\omega}}^b_{ib}) \boldsymbol{l}^b_s && (4.13)\\ &= \dot{\boldsymbol{v}}^i_{ib} + \boldsymbol{R}^i_b \boldsymbol{S}(\boldsymbol{\omega}^b_{ib})^2 \boldsymbol{l}^b_s + \boldsymbol{R}^i_b \boldsymbol{S}(\dot{\boldsymbol{\omega}}^b_{ib}) \boldsymbol{l}^b_s && (4.14)\\ &= \boldsymbol{R}^i_b \underbrace{\left(\boldsymbol{a}^b_{ib} + \boldsymbol{S}(\boldsymbol{\omega}^b_{ib})^2 \boldsymbol{l}^b_s + \boldsymbol{S}(\boldsymbol{\alpha}^b_{ib}) \boldsymbol{l}^b_s \right)}_{\boldsymbol{a}^b_{is}}, && (4.15) \end{aligned}$$

[4] but not necessarily coincide, i.e. the centre of $\{s\}$ is not at the same point as the centre of $\{b\}$

[5] For marine vessels the CO is often defined arbitrary to take advantage of the vessel's geometry, and does not necessarily coincide with the centre of gravity (CG) [16]

with the angular acceleration $\boldsymbol{\alpha}_{ib}^{b} = \dot{\boldsymbol{\omega}}_{ib}^{b}$. Besides the acceleration in the CO, the sensor registers two *fictitious accelerations*:

- **Centripetal acceleration** $\boldsymbol{S}(\boldsymbol{\omega}_{ib}^{b})^{2}\boldsymbol{l}_{s}^{b}$ acts when the vessel is turning. It acts orthogonally to the direction of motion of the vessel and points towards the centre of the curvature.
- **Euler acceleration** $\boldsymbol{S}(\boldsymbol{\alpha}_{ib}^{b})\boldsymbol{l}_{s}^{b}$ acts when the reference frame's rotational velocity changes. The Euler acceleration is perpendicular to the centripetal acceleration.

The fictitious accelerations occur because the body frame $\{b\}$ (and any sensor frame $\{s_i\}$ of a fixed sensor) of the vessels rotates together with the vessel, while the inertial frame $\{i\}$ remains fixed. This can be understood if one looks from perspective of $\{i\}$ on a point $\boldsymbol{p}_{ix}^{i}$. Assume the point is fixed, i.e. $\dot{\boldsymbol{p}}_{ix}^{i} = 0$, the point stands still. If the same point is observed from a rotating reference frame perspective (e.g. the body frame when the ship is turning), the fixed point $\boldsymbol{p}_{ix}^{b} = \boldsymbol{R}_{i}^{b}\boldsymbol{p}_{ix}^{i}$ seems to be moving. Note the change of superscript that indicates the change of perspective. The velocity of the point is now

$$\begin{aligned}\dot{\boldsymbol{p}}_{ix}^{b} &= \dot{\boldsymbol{R}}_{i}^{b}\boldsymbol{p}_{ix}^{i} + \boldsymbol{R}_{i}^{b}\dot{\boldsymbol{p}}_{ix}^{i} \\ &= \dot{\boldsymbol{R}}_{i}^{b}\boldsymbol{p}_{ix}^{i} \\ &= \boldsymbol{R}_{i}^{b}\boldsymbol{S}(\omega_{ib}^{b})\boldsymbol{p}_{ix}^{i} \neq 0.\end{aligned} \tag{4.16}$$

By rearranging (4.15) the acceleration in CO is obtained:

$$\boldsymbol{a}_{ib}^{b} = \boldsymbol{a}_{is}^{b} - \boldsymbol{S}(\boldsymbol{\omega}_{ib}^{b})^{2}\boldsymbol{l}_{s}^{b} - \boldsymbol{S}(\boldsymbol{\alpha}_{ib}^{b})\boldsymbol{l}_{s}^{b}. \tag{4.17}$$

Rearranging (4.7) gives an expression for the acceleration in the sensor's location:

$$\boldsymbol{a}_{is}^{b} = \boldsymbol{f}_{s}^{b} + \boldsymbol{R}_{i}^{b}\bar{\boldsymbol{g}}^{i} - \boldsymbol{b}_{a_s}^{b} - \boldsymbol{w}_{a_s}^{b}. \tag{4.18}$$

Entering (4.18) into (4.17) results in the acceleration in CO[6]:

$$\boldsymbol{a}_{ib}^{b} = \boldsymbol{f}_{s}^{b} + \boldsymbol{R}_{i}^{b}\bar{\boldsymbol{g}}^{i} - \boldsymbol{S}(\boldsymbol{\omega}_{ib}^{b})^{2}\boldsymbol{l}_{s}^{b} - \boldsymbol{S}(\boldsymbol{\alpha}_{ib}^{b})\boldsymbol{l}_{s}^{b} - \boldsymbol{b}_{a_s}^{b} - \boldsymbol{w}_{a_s}^{b}. \tag{4.19}$$

4.5 Ice induced accelerations

Riska showed in his doctoral thesis [56] that ice crushing, when hitting massive ice features, effects the ship hull vibrations. In [48] Matusiak showed that ship vibrations can be regarded as the motions of a forced, damped multi-degree-of-freedom (MDOF) system, given as

$$\mathbf{M}\ddot{\boldsymbol{x}} + \mathbf{C}\dot{\boldsymbol{x}} + \mathbf{G}\boldsymbol{x} = \boldsymbol{\tau}(t), \tag{4.20}$$

where $\mathbf{M} \in \mathbb{R}^{n\times n}$ is the mass matrix, $\mathbf{C} \in \mathbb{R}^{n\times n}$ is the damping matrix, $\mathbf{G} \in \mathbb{R}^{n\times n}$ is the stiffness matrix, and $\boldsymbol{x} \in \mathbb{R}^{n}$ is the displacement. Upon an external excitation, such as the impact of sea ice, the hull shows undamped vibrations

[6] or the acceleration $\boldsymbol{a}_{ix}^{b}$ felt at any other point $\boldsymbol{x}$ for which the distance $\boldsymbol{l}_{s}^{x}$ is given

due to the excitation of natural modes, denoted ϕ_i and congregated in the modal matrix $\mathbf{\Phi} = [\phi_1, \phi_2, \cdots, \phi_n]$. The natural modes of the vessel's hull can be found by solving (4.21) under a known load:

$$\ddot{\boldsymbol{\eta}}(t) + \mathbf{C}_g \dot{\boldsymbol{\eta}}(t) + \text{diag}(\omega_i^2)\boldsymbol{\eta}(t) = \text{diag}(M_i^{-1})\boldsymbol{f}(t), \tag{4.21}$$

where $\mathbf{C}_g = \text{diag}(2\xi_i\omega_i) \in \mathbb{R}^{n\times n}$ is the generalised damping matrix, M_i is the i^{th} generalised modal mass, ξ_i is the damping factor for the i^{th} natural mode, $\boldsymbol{f}(t) = \mathbf{\Phi}^T\boldsymbol{\tau}(t)$ is the generalised force, and $\boldsymbol{\eta} \in \mathbb{R}^n$ is the generalised coordinate vector. Further, Matusiak in [48] showed that a change in generalised mass can be calculated under the assumption of a velocity and ice thickness independent ship stiffness by

$$M_{i,1} = M_{i,0} \cdot \sqrt{\frac{f_{i,0}}{f_{i,1}}}. \tag{4.22}$$

Section 2.4 introduced three major ice failure mechanisms during operations of vessels in ice. Depending on the failure mechanism of the ice against the hull, vibrations are induced into the hull by excitation of the hull's natural modes described in (4.21). These vibrations are quickly damned out by the ship's structure. Therefore, only an accelerometer close to the hull and close to the impact location can measure the ice induced vibrations. An example from [26] is presented in Figure 4.7a. While the ship was travelling slowly in broken ice the port hull came into contact with a larger unbroken ice floe. The ice floe broke by bending and circumferential splitting. Higher natural modes of the hull were excited upon failure of the ice floe.

The measurement model (4.7) can be modified to include an ice induced vibration component in frame $\{s\}$:

$$\boldsymbol{f}_s^b = \tilde{\boldsymbol{a}}_{is}^b - \boldsymbol{R}_i^b \bar{\boldsymbol{g}}^i + \boldsymbol{b}_{a_s}^b + \boldsymbol{\xi}_s^b + \boldsymbol{w}_{a_s}^b, \tag{4.23}$$

with $\tilde{\boldsymbol{a}}_{is}^b = \boldsymbol{a}_{is}^b - \boldsymbol{\xi}_s^b$ being the vibration free acceleration at the sensor's location. The expression for the acceleration in CO given in (4.19) changes to:

$$\begin{aligned} \boldsymbol{a}_{ib}^b &= \tilde{\boldsymbol{a}}_{is}^b - \boldsymbol{S}(\boldsymbol{\omega}_{ib}^b)^2\boldsymbol{l}_s^b - \boldsymbol{S}(\boldsymbol{\alpha}_{ib}^b)\boldsymbol{l}_s^b & (4.24)\\ &= \boldsymbol{f}_s^b + \boldsymbol{R}_i^b\bar{\boldsymbol{g}}^i - \boldsymbol{S}(\boldsymbol{\omega}_{ib}^b)^2\boldsymbol{l}_s^b - \boldsymbol{S}(\boldsymbol{\alpha}_{ib}^b)\boldsymbol{l}_s^b - \boldsymbol{b}_{a_s}^b - \boldsymbol{\xi}_s^b - \boldsymbol{w}_{a_s}^b. & (4.25) \end{aligned}$$

Chapter 7, and [26], show the frequency properties of the ice-induced vibration $\boldsymbol{\xi}_s^b$. Chapter 8 illustrates the statistical properties of the ice-induced accelerations. The ice-induced vibrations can be regarded as an additional noise component. Measurement noise follows normally a Gaussian distribution, i.e.

$$\boldsymbol{w}_{a_s}^b \sim \mathcal{N}(\boldsymbol{\mu}_{\boldsymbol{w}_{as}}, \boldsymbol{\Sigma}_{\boldsymbol{w}_{as}}), \tag{4.26}$$

where $\boldsymbol{\mu}_{\boldsymbol{w}_{as}} \in \mathbb{R}^3$ is the mean vector of the measurement noise, and $\boldsymbol{\Sigma}_{\boldsymbol{w}_{as}} \in \mathbb{R}^{3\times3}$ is the covariance vector. Commonly the mean vector of the measurement noise is zero, i.e. $\boldsymbol{\mu}_{\boldsymbol{w}_{as}} = \mathbf{0}$. Ice-induced vibrations however do not necessarily follow a Gaussian distribution. Instead Chapter 8 shows that the ice-induced vibrations can be statistically modelled with a t-distribution, i.e.

$$\boldsymbol{\xi}_s^b \sim t(\boldsymbol{c}_{\boldsymbol{\xi}_s}, \boldsymbol{S}_{\boldsymbol{\xi}_s}, \nu_{\boldsymbol{\xi}_s}), \tag{4.27}$$

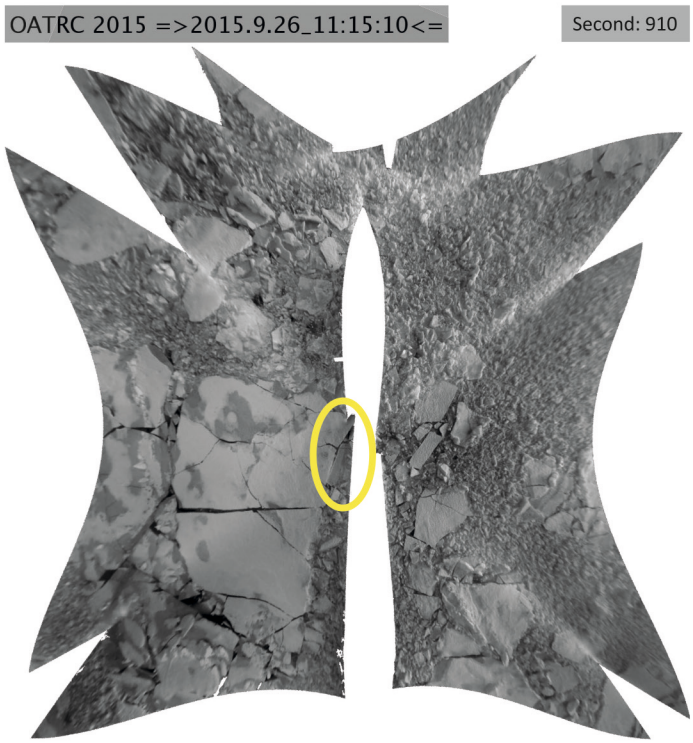

(a) Camera image

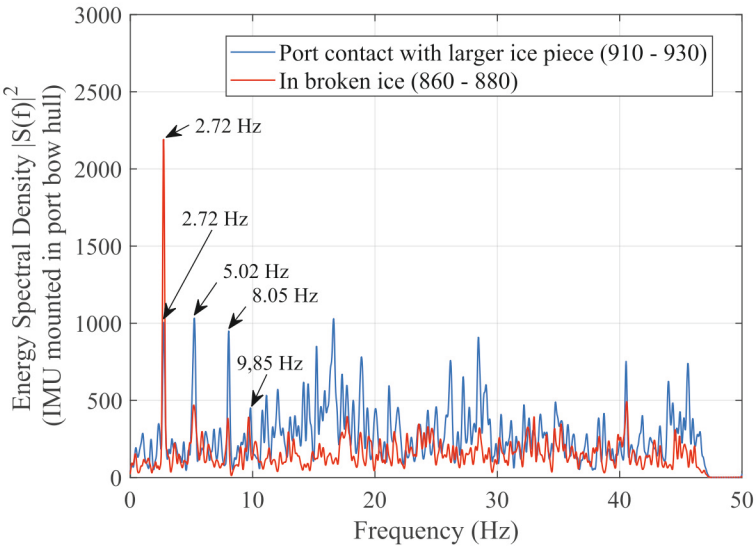

(b) Power density spectrum (PSD)

Figure 4.7: Encounter of unbroken ice floe in broken ice [26]

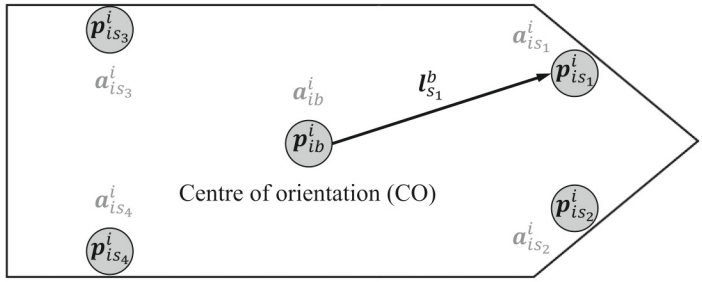

Figure 4.8: Positions of a distributed IMU setup in relation to the centre of orientation (CO)

where $\boldsymbol{c}_{\boldsymbol{\xi}_s} \in \mathbb{R}^3$ is the location vector, $\boldsymbol{S}_{\boldsymbol{\xi}_s} \in \mathbb{R}^{3\times3}$ is the shape vector, and $\nu_{\boldsymbol{\xi}_s} \in \mathbb{R}^1$ represents degrees of freedom of the distribution.

Statistical analysis allows the detection and separation of ice-induced vibrations in the overall measurement signal of the accelerometers.

4.6 Modelling of multi sensor configuration

The ice-induced accelerations are very localised. Therefore, it is required to establish a network of motion sensors in order to capture ice-induced accelerations at several locations along the hull. Figure 4.8 shows an example of a network of motion sensors. Kjerstad et al. presented in [31] a parameterisation of (4.17) for a configuration of four sensors which has been generalised to N sensors by [60]. The dynamic variables are accumulated in

$$\boldsymbol{z}^b_{ib} = [\tilde{\boldsymbol{a}}^b_{ib}, \boldsymbol{\alpha}^b_{ib}, \bar{\boldsymbol{\omega}}^b_{ib}]^\top \in \mathbb{R}^{12}, \tag{4.28}$$

and the static variables for each sensor s_i are collected in

$$\boldsymbol{W}(l^b_{s_i}) = [\boldsymbol{I}_{3\times3}, -\boldsymbol{S}(\boldsymbol{l}^b_{s_i}), \boldsymbol{H}(\boldsymbol{l}^b_{s_i})]^\top \in \mathbb{R}^{3\times12}. \tag{4.29}$$

Note that $\bar{\boldsymbol{\omega}}^b_{ib} = [\omega_x^2, \omega_y^2, \omega_z^2, \omega_x\omega_y, \omega_x\omega_z, \omega_y\omega_z]^\top \in \mathbb{R}^6$, $\boldsymbol{S}(\boldsymbol{\alpha}^b_{ib})\boldsymbol{l}^b_{s_i} = -\boldsymbol{S}(\boldsymbol{l}^b_{s_i})\boldsymbol{\alpha}^b_{ib}$, $\boldsymbol{S}(\boldsymbol{\omega}^b_{ib})^2\boldsymbol{l}^b_{s_i} = \boldsymbol{H}(\boldsymbol{l}^b_{s_i})\bar{\boldsymbol{\omega}}^b_{ib}$, and

$$\boldsymbol{H}(\boldsymbol{l}^b_{s_i}) = \begin{bmatrix} 0 & -l_x & -l_x & l_y & l_z & 0 \\ -l_y & 0 & -l_y & l_x & 0 & l_z \\ -l_z & -l_z & 0 & 0 & l_x & l_y \end{bmatrix}. \tag{4.30}$$

The specific force readings (4.23) can then be parameterised for sensor s_i as:

$$\boldsymbol{f}^b_{s_i} = \boldsymbol{W}(\boldsymbol{l}^b_{s_i})\boldsymbol{z}^b_{ib} - \boldsymbol{R}^b_i\bar{\boldsymbol{g}}^i + \boldsymbol{b}^b_{a_{s_i}} + \boldsymbol{\xi}^b_{s_i} + \boldsymbol{w}^b_{a_{s_i}}. \tag{4.31}$$

For a configuration of N sensors, the measurements, bias, ice-induced vibrations and noise vectors can be accumulated to

$$\boldsymbol{f}^b_{\text{vec}} = [\boldsymbol{f}^b_{s_1}, \boldsymbol{f}^b_{s_2}, \cdots, \boldsymbol{f}^b_{s_N}]^\top \in \mathbb{R}^{3N} \tag{4.32}$$

$$\boldsymbol{b}^b_{\text{vec}} = [\boldsymbol{b}^b_{a_{s_1}}, \boldsymbol{b}^b_{a_{s_2}}, \cdots, \boldsymbol{b}^b_{a_{s_N}}]^\top \in \mathbb{R}^{3N} \tag{4.33}$$

$$\boldsymbol{\xi}^b_{\text{vec}} = [\boldsymbol{\xi}^b_{s_1}, \boldsymbol{\xi}^b_{s_2}, \cdots, \boldsymbol{\xi}^b_{s_N}]^\top \in \mathbb{R}^{3N} \tag{4.34}$$

$$\boldsymbol{w}^b_{\text{vec}} = [\boldsymbol{w}^b_{a_{s_1}}, \boldsymbol{w}^b_{a_{s_2}}, \cdots, \boldsymbol{w}^b_{a_{s_N}}]^\top \in \mathbb{R}^{3N} \tag{4.35}$$

The specific force combined measurement vector is then

$$\boldsymbol{f}^b_{\text{vec}} = \boldsymbol{W}(\boldsymbol{l})\boldsymbol{z}^b_{ib} - \mathbf{1}_N \otimes \left(\boldsymbol{R}^b_i \bar{\boldsymbol{g}}^i\right) + \boldsymbol{b}^b_{\text{vec}} + \boldsymbol{\xi}^b_{\text{vec}} + \boldsymbol{w}^b_{\text{vec}}, \tag{4.36}$$

where $\mathbf{1}_N$ is a vector of N ones, $A \otimes B$ represents the *Kronecker product*, and

$$\boldsymbol{W}(\boldsymbol{l}) = [\boldsymbol{W}(\boldsymbol{l}^b_{s_1}), \boldsymbol{W}(\boldsymbol{l}^b_{s_2}), \cdots, \boldsymbol{W}(\boldsymbol{l}^b_{s_N})]^\top \in \mathbb{R}^{3N\times 12} \tag{4.37}$$

By defining $\boldsymbol{W}(\boldsymbol{l})^\dagger$ as the *Moore-Penrose pseudoinverse* of $\boldsymbol{W}(\boldsymbol{l})$, (4.36) can be solved for $\boldsymbol{z}^b_{ib}$:

$$\boldsymbol{W}(\boldsymbol{l})^\dagger \boldsymbol{f}^b_{\text{vec}} = \boldsymbol{z}^b_{ib} - \boldsymbol{W}(\boldsymbol{l})^\dagger \left(\mathbf{1}_N \otimes \left(\boldsymbol{R}^b_i \bar{\boldsymbol{g}}^i\right) - \boldsymbol{b}^b_{\text{vec}} - \boldsymbol{\xi}^b_{\text{vec}} - \boldsymbol{w}^b_{\text{vec}}\right) \tag{4.38}$$

$$\boldsymbol{z}^b_{ib} = \boldsymbol{W}(\boldsymbol{l})^\dagger \left(\boldsymbol{f}^b_{\text{vec}} + \left(\boldsymbol{R}^b_i \bar{\boldsymbol{g}}^i\right)\right) - \boldsymbol{W}(\boldsymbol{l})^\dagger \left(\boldsymbol{b}^b_{\text{vec}} + \boldsymbol{\xi}^b_{\text{vec}} + \boldsymbol{w}^b_{\text{vec}}\right) \tag{4.39}$$

The ice-induced vibration free acceleration in CO can be found by multiplying (4.39) with a selection matrix $\boldsymbol{H}_a$:

$$\tilde{\boldsymbol{a}}^b_{ib} = \boldsymbol{H}_a \boldsymbol{z}^b_{ib} \tag{4.40}$$

$$= \boldsymbol{H}_a \boldsymbol{W}(\boldsymbol{l})^\dagger \left(\boldsymbol{f}^b_{\text{vec}} + \left(\boldsymbol{R}^b_i \bar{\boldsymbol{g}}^i\right)\right) - \boldsymbol{H}_a \boldsymbol{W}(\boldsymbol{l})^\dagger \left(\boldsymbol{b}^b_{\text{vec}} + \boldsymbol{\xi}^b_{\text{vec}} + \boldsymbol{w}^b_{\text{vec}}\right), \tag{4.41}$$

$$\boldsymbol{H}_a = [\boldsymbol{I}_{3\times 3}, \mathbf{0}_{3\times 9}]^\top \in \mathbb{R}^{3\times 12}. \tag{4.42}$$

Note that the $\boldsymbol{W}(\boldsymbol{l})^\dagger$ is only properly defined if not more than 3 sensors span a plane, i.e. the sensors are not coplanar [67]. For four sensors it means that one sensors must be placed out of plane. Furthermore, besides providing the accelerations in CO, the parameterisation (4.39) also gives the angular velocities and angular accelerations from linear acceleration measurements. The results can be enhanced by employing sensor fusion with the gyro readings.

Chapter 5

Arctic expeditions and data sources

Vid polens tröskel bland skär och vågor.
Ett land jag vet,
Ej rikt som drufvornas land i söder,
Men skönt som det:
På fästet stjernor och norrskenslågor
Dess vinter satt,
Och junisol öfver fjellen glöder
I sommarnatt

Ernst Björck

The results from this thesis base on field data collected during four expeditions on four ships. This chapter will give an overview of each expedition. It will state the general purpose of each expedition, the equipment installed in respect to this thesis, the region where the data were collected and an overview of the collected data.

Figure 5.1: CCGS Amundsen [64]

5.1 CCGS Amundsen, Labrador Sea, 2015

The CCGS Amundsen, Figure 5.1, sailed from 17th April to 6th May 2015 through the Lawrence Strait and the Labrador Sea off the coast of Newfoundland and Labrador. Figure 5.3 shows the track of the ship during the expedition. It was conducted as a cooperation between Statoil Canada and ArcticNet, a network of Canadian universities, agencies and the private sector in the field of Arctic research.

The main purpose of the expedition was meteorology, oceanography, iceberg, and sea ice research. NTNU operated a 360° camera system to monitor ice conditions around the vessel. The camera system consisted of three camera units with a total of twelve lenses. Furthermore, a prototype IMU was brought onboard and tested as proof of concept while the ship encountered drifting ice floes and during transit in broken ice.

The main purpose of the expedition in regards to this thesis was to gain experience in the Arctic environment and to install and operate the 360° camera system. The proof of concept for motion measurements during ice encounter was a side project. The prototype IMU was installed in the bow of the vessel, as depicted in Figure 5.2. The sensor was an ADIS16480, which is a slightly improved version of the ADIS16364 used during the other expeditions. As preliminary results the

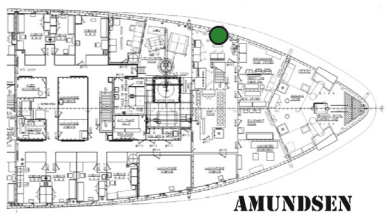

Figure 5.2: Location of IMU prototype

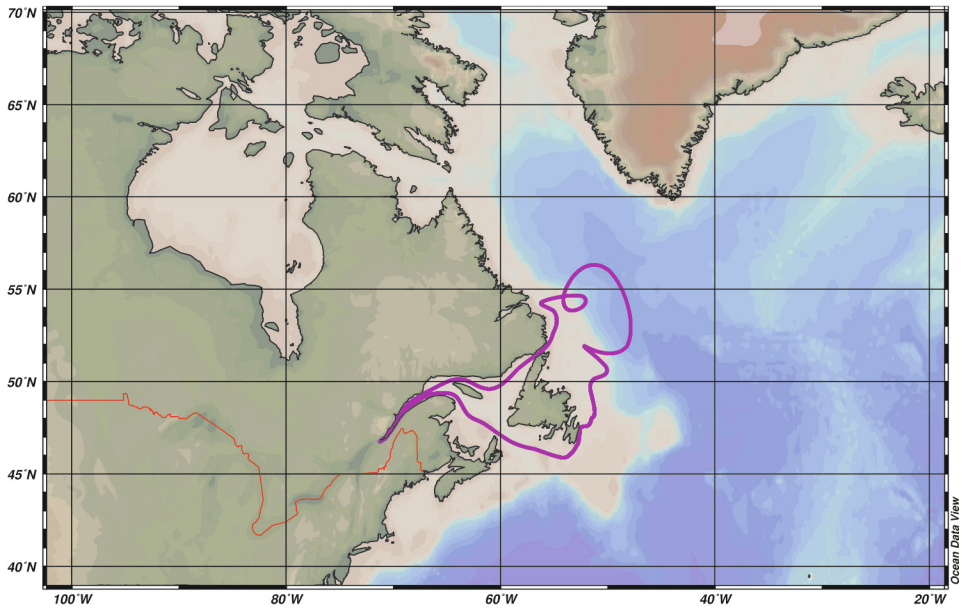

Figure 5.3: Track of CCGS Amundsen during 2015 expedition

expedition revealed that IMUs are well capable of measuring ice induced accelerations in the hull. Therefore, a full system was developed, calibrated and tested in the laboratory in the following months after the expedition.

Figure 5.4: Icebreaker Frej [65]

5.2 IB Frej, Arctic Ocean, 2015

As part of the "Oden Arctic Technology Research Cruise 2015" (OATRC2015), the two Swedish icebreakers Oden (Figure 5.7) and Frej (Figure 5.4) sailed from Longyearbyen on Svalbard into the Arctic Ocean. The expedition was a cooperation of NTNU and the Swedish Polar Research Secretariat (SPRS), supported by the ExxonMobil Upstream Research Company. It took place from 18th September to 2nd October.

The expedition's main goal was to test and evaluate ice management tactics

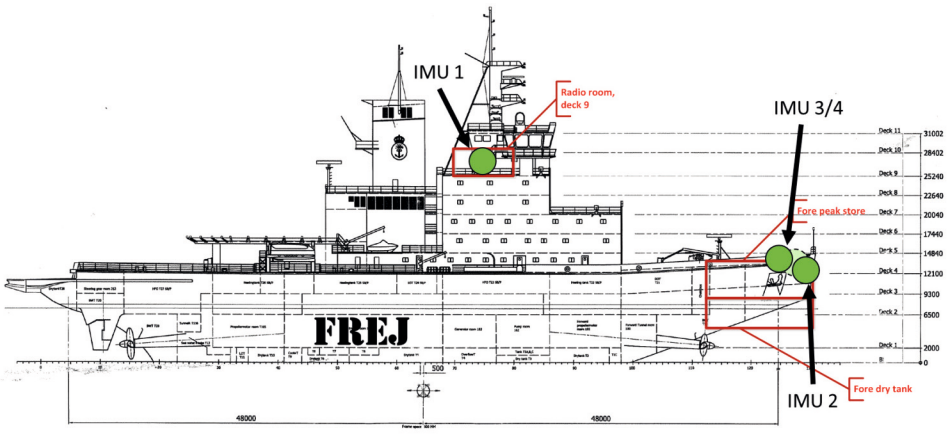

Figure 5.5: Positions of IMUs on Frej

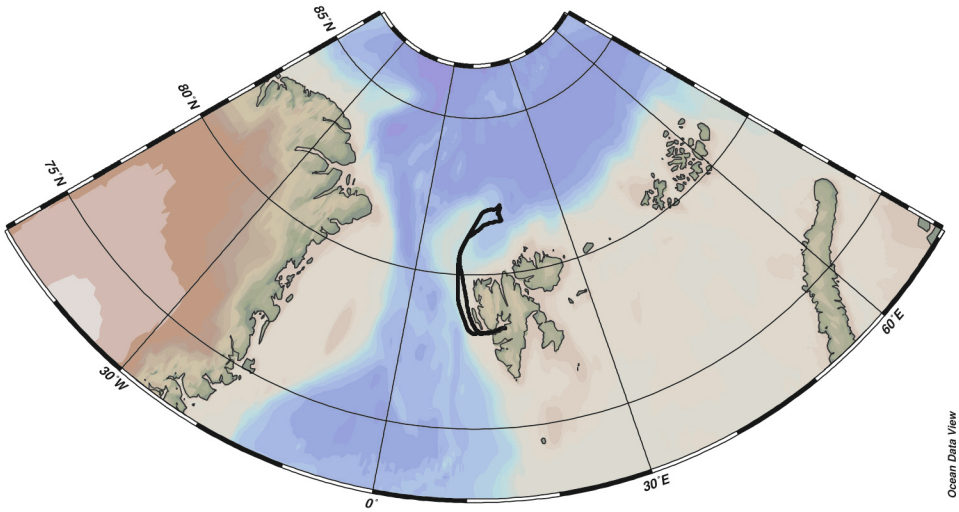

Figure 5.6: Track of IB Frej during OATRC 2015

and to collect full-scale data for validation of models of ice-action against floating structures. A full overview of the objectives and research activities can be found in [44, 45]. The track of icebreaker Frej is illustrated in Figure 5.6.

For this thesis images from a 360° camera system and motion data from a distributed IMU system were collected. These data were used for research on frequency analysis of ice-induced hull vibrations (see Chapter 7). The camera system consisted of three panoramic camera units and an ice thickness camera as illustrated in Figure 3.3b. Additional cameras monitored the bow of the vessel. The IMU system consisted of four IMUs, out of which one IMU was installed on the bridge-level and three IMUs directly in the bow of the vessel. The installation points of the IMUs are given in Figure 5.5. Additional ship data were collected, such as GPS positions, engine status and meteorological data.

The IMU on the bridge-level provided reference measurements of the ship's motion, as it was not affected by ice induced hull vibrations. The remaining three IMUs measured ice-induced vibrations in the bow section of the hull while the vessel transited in different ice conditions. The main purpose was to identify a relationship between ice conditions and ice induced vibrations. The camera images provided a ground-truth of the surrounding ice conditions.

Figure 5.7: Icebreaker Oden (Courtesy of Lars Lehnert)

5.3 IB Oden, Arctic Ocean, 2016

From 8th August to 20th September 2016 the icebreaker Oden (5.7) sailed together with the Canadian icebreaker CCGS Luis S. St-Laurent into the Arctic Ocean. As part of the Swedish *SWEDARCTIC* program three scientists from NTNU were invited to join the Arctic Ocean 2016 expedition onboard Oden. The track of Oden during the cruise is illustrated in Figure 5.9.

The Arctic Ocean 2016 expedition focused on geoscience to support Canada's United Nations Convention of the Law of the Sea (UNCLOS) submission. Oden's main tasks were serving as icebreaker support for the CCGS Luis S. St-Laurent, sea bottom profiling, seismic reflection, and core sampling. Besides these tasks, twelve science work packages were carried out. A full report is given in [17].

As part of the work package *Ice Management*, a camera system as depicted in Figure 3.3b recorded the surrounding ice conditions. Four IMU sensors were distributed throughout the ship as illustrated in Figure 5.8. The aim was to find a relationship between the ice conditions monitored by the camera systems and the statistical properties of the ice induced vibrations in the hull recorded by the IMUs. Furthermore, the system was tested in long term operations. As result, a system was presented that detects changes in ice conditions during transit by monitoring the statistical properties of the IMUs' signals (see Chapter 8).

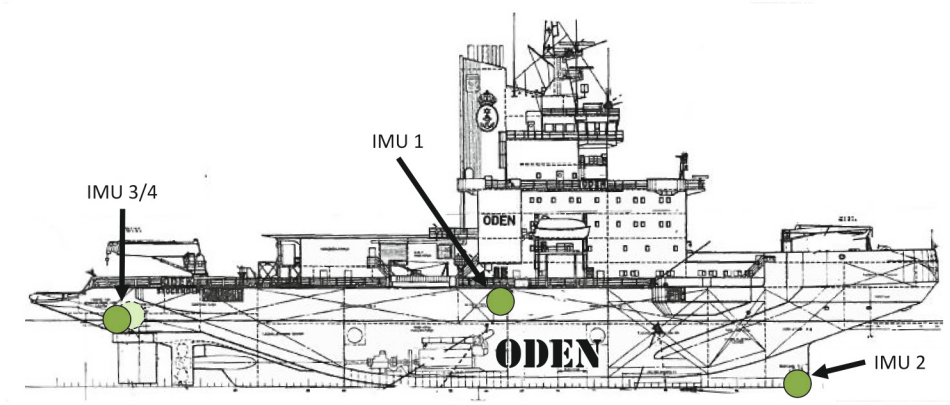

Figure 5.8: Positions of IMUs on Oden

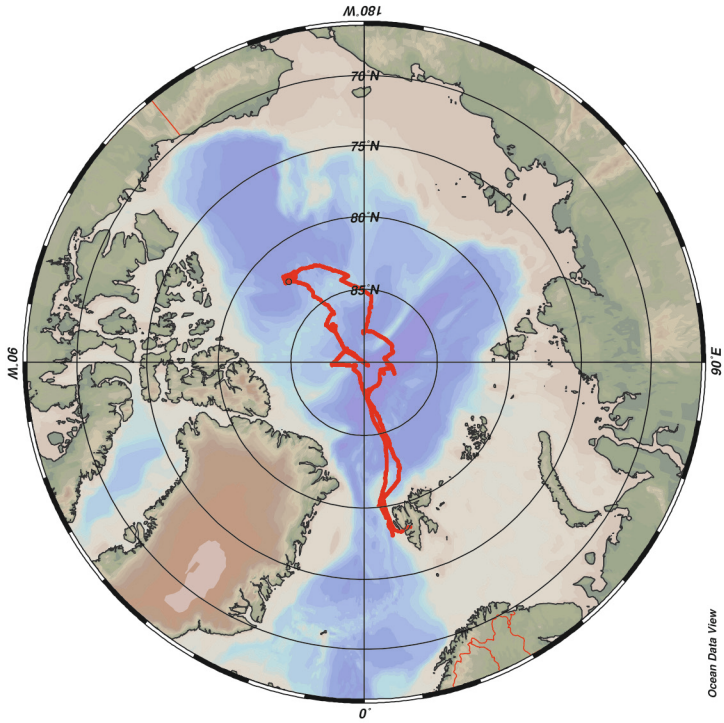

Figure 5.9: Track of IB Oden during Arctic Ocean 2016

Figure 5.10: Magne Viking (Courtesy of Francesco Scibilia)

5.4 Magne Viking, Bay of Bothnia, 2017

The Station-Keeping Trials in ice (SKT) project conducted by Equinor aimed at the collection of full-scale data for validation of models of floating structures in ice. Equinor invited several NTNU scientist to join the cruise. The vessels Magne Viking (Figure 5.10) and Tor Viking participated in the expedition. The cruise took place from 3rd March to 17th March 2017 and the main operation area was the Bay of Bothnia. The track of the cruise is illustrated in Figure 5.12.

The major objective of the expedition was to collect data on a floating vessel during stationkeeping with a mooring system. Magne Viking was the stationkeeping vessel, while Tor Viking provided icebreaker support and anchor handling. A complete list of objectives can be found in [37]. Magne Viking as the main test vessel was heavily equipped with ice load monitoring systems [55] and ship system logging systems [1]. The test scenarios and encountered ice conditions were summarised in [38, 62].

In regard to this thesis, it was an unique chance to test the distributed motion sensing system on a ship performing stationkeeping in ice. During no other expedition stationkeeping data could be collected. Magne Viking was therefore equipped with the distributed IMU system as illustrated in Figure 5.11. Four sensors were installed at water level. The two sensors towards the bow were placed directly on the outer hull, while the aft sensors had to be placed inside the engine room. A fifth sensor on the bridge provided reference measurements without the influence of hull vibrations. Under mooring and dynamic positioning, and under different ice conditions, motion data were collected. The main objective was to test if by analysis of the vibration components a detection of ice drift during stationkeeping and accumulation of ice against the hull is possible. The results are presented in Chapter 8.

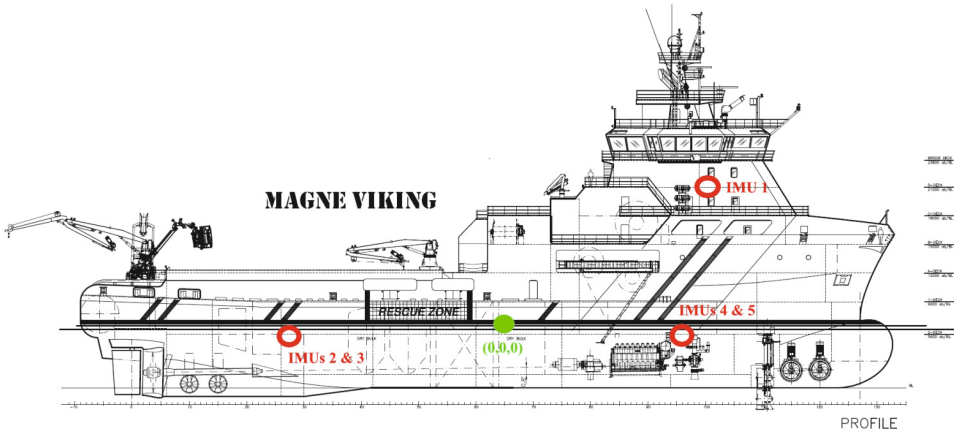

Figure 5.11: Positions of IMUs on Magne Viking

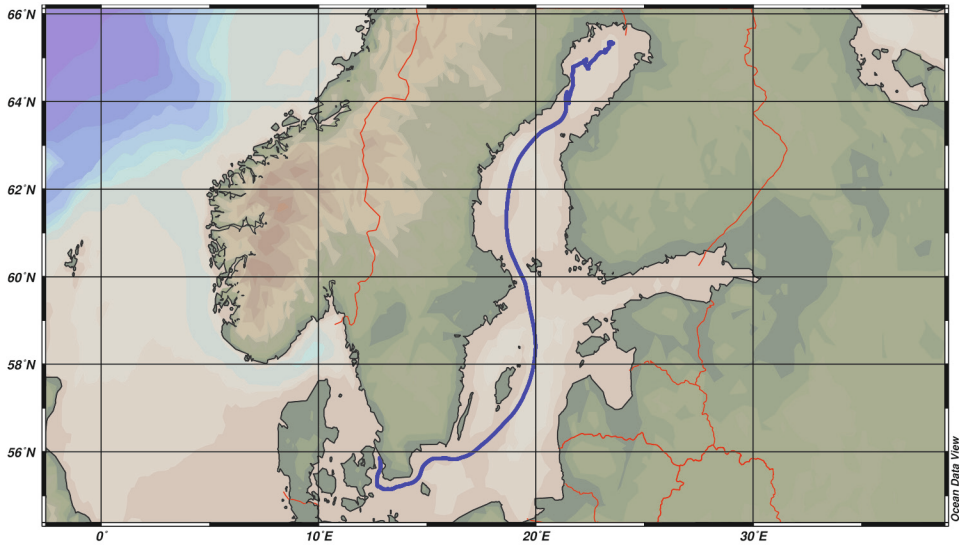

Figure 5.12: Track of Magne Viking during SKT 2017

Part II

Selected publications

Chapter 6

Creating a ground truth with optical cameras

Paper 1: Heyn, Hans-Martin; Knoche, Martin; Zhang, Qin; Skjetne, Roger. A system for automated vision-based sea-ice concentration detection and floe-size distribution indication from an icebreaker. I: ASME 2017 36th International Conference on Ocean, Offshore and Arctic Engineering - Volume 8: Polar and Arctic Sciences and Technology; Petroleum Technology, Trondheim, Norway, June 25–30, 2017. ASME Press 2017

Chapter 7

Fundamentals of motion sensing for local ice condition assessment

7.1 A system for distributed motion sensing on a ship

Paper 2: Heyn, Hans-Martin; Skjetne, Roger; Scibilia, Francesco. Distributed sensing of loads acting against the hull of a stationkeeping vessel in ice. I: ASME 2018 37th International Conference on Ocean, Offshore and Arctic Engineering - Volume 8: Polar and Arctic Sciences and Technology; Petroleum Technology. ASME Press 2018 ISBN

7.2 Time-frequency analysis of motion data on a ship in sea ice

Cold Regions Science and Technology 156 (2018) 61–74

Contents lists available at ScienceDirect

Cold Regions Science and Technology

journal homepage: www.elsevier.com/locate/coldregions

Time-frequency analysis of acceleration data from ship-ice interaction events

Hans-Martin Heyn*, Roger Skjetne

Norwegian University of Science and Technology (NTNU),Trondheim 7491, Norway

ARTICLE INFO

Keywords:
Arctic
Ship-ice interaction
Acceleration
Wigner-Ville distribution
Time-frequency analysis
Vibrations
Ice load
Marine technology
Ocean engineering

ABSTRACT

During operations with ships in ice-infested waters, vibrations of the hull occur due to ship-ice interaction. The acting ice load and the induced vibrations depend on the ice regime and ice breaking mechanism. Especially crushing of ice against the hull causes high loads against the vessel. The objective of this study is to analyse the frequency components of ice-induced vibrations, measured with accelerometers placed in the bow section of the ship's hull. The Wigner-Ville distribution, which provides a time-frequency representation, is applied on acceleration data collected on the icebreaker Frej during transit in ice-infested Arctic waters. The resulting time-frequency representations show that the excited frequencies depend on the dominant ice breaking mechanism, on the encounter velocity, and on the position of where the ice interaction against the hull occurs. Furthermore, the natural frequencies of the ship's hull change slightly, depending on the conditions on the sea-ice around the vessel. It is concluded that a system of distributed accelerometers on a ship can provide information about the acting ice breaking mechanism, the ice conditions around the vessel, and about the location along the hull, where the ship-ice interaction occurs. This can be used as an additional tool in monitoring systems during operations in ice-infested waters.

1. Introduction

The presence of sea-ice makes operations in the Arctic challenging (Løset et al., 2006). The decay of ice cover in the Arctic region (Lubin and Massom, 2006) will lead to new sea-cargo routes between Europe and Asia (Arctic Council, 2009). Furthermore, hydrocarbon deposits lie possibly under the seabed of the Arctic oceans (Hossain et al., 2014). Technologies have to be developed to support safe and sustainable operations in the fragile environment of the Arctic. Ice management refers to a system that is capable of reducing the ice loads on a protected vessels to endurable levels (Hamilton et al., 2011). An ice management system can be parted into an ice observer system and a response system (Eik, 2008). The ice observer system requires ice intelligence, which is obtained by collecting and processing information about the ice environment utilising different sensor technologies (Haugen et al., 2011). When a ship operates in ice-infested waters, it is subjected to ice-induced vibrations (Belov and Spiridonov, 2012). The properties of the ice-induced vibration change, depending on the ice interaction mechanism and the ice load affecting the vessel (Yue et al., 2009). In laboratory experiments, Sodhi (1991) showed that the ice-induced vibrations clearly depend on the failure mechanism of the ice. Measuring and evaluating the ice-induced vibrations in real-time could therefore be a reliable source of ice intelligence.

By measuring vibrations on the Finnish icebreaker Sisu during ice-breaking operations, Matusiak (1982) showed that the additional ice load excites several natural modes of the ship's hull in the bandwidth 2.75 Hz to 7.5 Hz. For a narrow, conical structure, equipped with load panels, Yue et al. (2007) showed that the frequency spectrum of the measured ice loads change under different ice conditions. They used short-time fourier transformation (STFT) for their analysis. The major drawback of the STFT is that the product of time resolution and frequency resolution is constant. It is desired to have a higher frequency resolution at the lower frequency band, in which the ice-induced vibrations typically occur. Bjerkås (2006) overcame this limitation by using a wavelet transformation. Bjerkås et al. (2007) applied a continuous wavelet transformation on ice load signals recorded during ice-structure interaction of a lighthouse in the Gulf of Bothnia. The authors were able to identify intervals of intermittent crushing of ice against the structure, which was the cause of high ice loads and significant vibrations in the structure.

The results from the wavelet transformation can be difficult to interpret, because the resulting spectrum depends on the chosen wavelet function. It is more intuitive to study directly the energy representation of the recorded vibrations and to determine the distribution of the

* Corresponding author.
E-mail address: martin.heyn@ntnu.no (H.-M. Heyn).

https://doi.org/10.1016/j.coldregions.2018.01.019
Received 31 January 2017; Received in revised form 1 December 2017; Accepted 29 January 2018
Available online 08 February 2018
0165-232X/

energy content of the vibrations over both frequency and time (Flandrin et al., 2002). The Wigner-Ville distribution is such a joint time-frequency energy density (Boashash, 2003). The vibrations can be recorded with accelerometers placed inside the hull of a ship. Compared to strain gauges or load panels, accelerometers are significantly easier to install and they can be placed anywhere in the ship at little cost and effort.

This study shows that data from accelerometers placed in the hull of a ship, in combination with the Wigner-Ville distribution, provides clear time and frequency information about ice-induced vibrations. The aim is to provide an additional tool for ice condition assessment. Typical ship-ice interaction events as cause for ice-induced vibrations are introduced. A windowed version of the Wigner-Ville distribution, which allows real-time analysis of ice-induced vibrations, is derived. The data from a system of four accelerometers on the icebreaker Frej is used for frequency analysis by the proposed method. In five scenarios, the frequency patterns during ship-ice interaction are analysed and discussed. Because the icebreaker Frej is a sistership of the Finnish icebreaker Sisu, a comparison with the results of Matusiak (1982) is conducted. It is shown that the variations of the natural frequencies of the ship's hull can be tracked in order to assess the ice conditions.

The paper is structured as follows: Section 2 contains a brief overview of the relevant theory on ship-ice interaction and ice-induced vibrations. Section 3 presents the methodology of the time-frequency decomposition based on the Wigner-Ville distribution. Section 4 describes the test setup on the Swedish Atle-class icebreaker Frej and a method to estimate the impact load during the encounter of sea-ice. In Section 5 the recorded acceleration data and the result from the time-frequency analysis are presented and discussed. Section 6 provides a closer analysis of the excitation of natural modes of the ship's hull. Section 7 concludes the research results and gives an outlook on future research.

2. Ship-ice interaction

The effects of ship-ice interaction depend on properties of the ship and properties of the ice. When a ship interacts with ice, either by ice drifting towards it or the ship travelling through ice, the ice eventually breaks. The additional loads a ship experiences during the ice-breaking process depend on the failure mode of the ice (ISO/FDIS/19906:2010, 2010). During ship-ice interaction, three failure modes play a significant role: Failure due to bending of the ice, failure of the ice by splitting, and failure of the ice by crushing. The active failure mode depends on the shape of the structure (e.g., inclination angle) and several state variables and material properties of the ice (Lu et al., 2015a). State variables are the encounter velocity, the contact area, and the temperature. Some ice properties are the density/porosity of the ice, the ice thickness, and the salinity.

2.1. Ice loads due to bending failure

Due to the gravitational force, the structure or vessel pushes the ice downwards. A vertical force component builds up, and once it exceeds the breaking strength of the ice, the ice fails by radial and circumferential cracking. Su et al. (2010) mentions that, due to the periodic characteristic of the process, dominant frequencies in the load by bending failure are identifiable. Yue et al. (2009) identified such regular force patterns for the interaction of ice and a slender vertical monopod structures. Bending failure is the dominant failure mechanism for sloping structures (Løset et al., 2006, Ch. 5), such as in the bow of an icebreaker.

2.2. Ice loads due to splitting failure

Besides bending failure, splitting as failure mode can occur especially in level-ice. As in the case of bending failure, a vertical force component builds up and leads to radial and circumferential cracking of the ice. In-plane forces act on the ice floe and on the newly formed crack. Lu et al. (2015b) refers to them as *splitting loads*. They cause an opening of the crack and a propagation of the crack in the ice floe. The propagated crack can extend to a length longer than the structure causing it (Bhat et al., 1991). When the ship propagates into the crack, and thus widens the crack, ice can slide along the hull, which typically cause measurable vibrations.

2.3. Ice loads due to crushing failure

Especially at small contact areas, non-sloped contact areas, and high encounter speeds, or with increasing ice thickness, crushing failure becomes the dominant failure mode during ship-ice interaction. The contact area of the ice with the ship or structure is changing randomly, which causes a non-uniform pressure distribution (Løset et al., 2006 Ch. 5) and the production of pulverized material. Due to the random size of the contact area, the load does not show regular frequency patterns. Instead a rather chaotic pattern is observed (Masterson et al., 1999; Yue et al., 2009).

2.4. The ice-breaking process

According to Riska (2011), Lubbad and Løset (2011), and Su et al. (2010), the ice-breaking occurs generally in four steps, as shown in Fig. 1: When the ship encounters an ice floe, the ship's hull and the ice form a small contact area. Due to the small contact area ice crushing will be the dominating failure mode. The ship will proceed further into the ice, which increases the contact area between the hull and the ice. A vertical force component on the ice increases until the bending strength of the ice is reached and ice floes are created by the formation of a bending crack, as described by Riska (2011). The ice pieces start to rotate and to push against the hull. This can cause an additional slamming load against the hull of the vessel (Lubbad and Løset, 2011) and an additional hydrostatic load can occur due to ventilation. This will occur if the gaps between the rotating ice floe and the water surface do not fill up with sea water fast enough. After the rotation process, the ice floe slides along the hull of the vessel until it clears to the sides or gets milled in the propellers of the vessel. If the ice is too strong, for example in the case of multi-year ice, the necessary vertical force component will not exceed the strength of the ice. Instead of bending, the ice will then continue to fail by crushing.

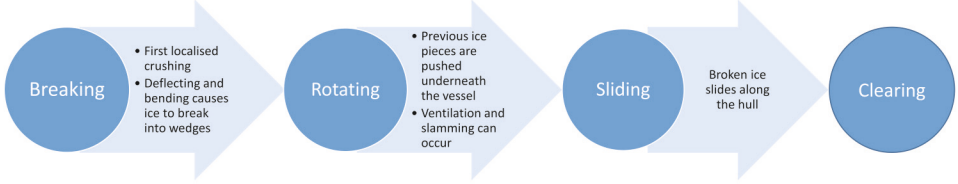

Fig. 1. The ice-breaking process under conventional ice conditions.

2.5. Ice-induced vibrations

Matusiak (1982) showed that ship vibrations can be regarded as the motions of a forced, damped multi-degree-of-freedom (MDOF) system, given as

$$\mathbf{M}\ddot{\boldsymbol{x}} + \mathbf{C}\dot{\boldsymbol{x}} + \mathbf{G}\boldsymbol{x} = \boldsymbol{\tau}(t), \tag{1}$$

with $\mathbf{M} \in \mathbb{R}^{n\times n}$ is the mass matrix, $\mathbf{C} \in \mathbb{R}^{n\times n}$ is the damping matrix, $\mathbf{G} \in \mathbb{R}^{n\times n}$ is the stiffness matrix, and $\boldsymbol{x} \in \mathbb{R}^n$ is the displacement. Upon an external excitation, such as the impact of sea-ice, the hull shows undamped free-vibrations natural modes, denoted ϕ_i, congregated in the modal matrix $\boldsymbol{\Phi} = [\phi_1, \phi_2, \cdots, \phi_n]$. The natural modes of the vessel's hull can be found by solving Eq. (2) under a known load:

$$\ddot{\boldsymbol{\eta}}(t) + \mathbf{C}_g\dot{\boldsymbol{\eta}}(t) + \text{diag}\quad(\omega_i^2)\boldsymbol{\eta}(t) = \text{diag}\quad(M_i^{-1})\boldsymbol{f}(t), \tag{2}$$

where $\mathbf{C}_g = \text{diag}(2\xi_i\omega_i) \in \mathbb{R}^{n\times n}$ is the generalised damping matrix, M_i is the ith generalised modal mass, ξ_i is the damping factor for the ith natural mode, $\boldsymbol{f}(t) = \boldsymbol{\Phi}^T\boldsymbol{\tau}(t)$ is the generalised force, and $\boldsymbol{\eta} \in \mathbb{R}^n$ is the generalised coordinate vector. Matusiak (1982) showed further that a change in generalised mass can be calculated under the assumption of a velocity and ice thickness independent ship stiffness by

$$M_{i,1} = M_{i,0}\cdot\sqrt{\frac{f_{i,0}}{f_{i,1}}}. \tag{3}$$

The generalised parameters have been identified by Matusiak (1982) for the icebreaker Sisu, a sister ship of the icebreaker Frej. They are summarised in Table 1.

3. Time-frequency analysis of acceleration signals

Changes in the ice failure regime cause changes in the frequency characteristic of the induced vibrations, and ice failure against the hull can also excite the natural modes of the ship's hull. Following the definition of Boashash (2003) we require the following results from a time-frequency decomposition:

- Identification of time variations in the signal in order to detect ice interaction events.
- Identification of frequency variations in the signal in order to characterize the ice failure regime and track the excitation of natural frequencies.

3.1. Definition of a signal and its spectrum

The *spectrum* $S(f)$ of a signal $s(t)$ is given by the *Fourier transformation*

Table 1
Generalised parameters of the icebreaker Sisu, a sister ship of the icebreaker Frej (Matusiak, 1982).

Mode	Condition	Natural	Generalised	Generalised mass
	(ice thickness)	frequency ω_i	damping ξ_i	M_i (kg·m^2)
1	Open water	2.916 Hz	0.008	0.1180
	30 cm	2.769 Hz	0.053	0.1210
	50 cm	2.703 Hz	0.095	0.1220
2	Open water	5.513 Hz	0.012	0.0201
	30 cm	5.150 Hz	0.054	0.0208
	50 cm	5.078 Hz	0.112	0.0210
3	Open water	7.550 Hz	0.011	0.0047
	30 cm	7.067 Hz	0.046	0.0050
	50 cm	6.594 Hz	0.084	0.0052
4	Open water	9.000 Hz	0.011	0.0036
	30 cm	8.700 Hz	0.044	0.0037
	50 cm	8.312 Hz	0.076	0.0038

$$\begin{aligned} S(f) &= \mathscr{F}\{s(t)\} \\ &= \int_{-\infty}^{\infty} s(t)e^{-j2\pi ft}dt. \end{aligned} \tag{4}$$

A real signal $s(t)$ exhibits *Hermitian symmetry* between the positive-frequency and negative-frequency components of its spectrum (Ohm and Lüke, 2010, Ch. 3).

$$S(-f) = S^*(f) \tag{5}$$

A *stationary signal* $s(t)$ can be written as the sum of cosine-terms and an offset a_0 (Hoffmann and Wolff, 2014, pp. 102–104), as shown in Eq. (6).

$$s(t) = a_0 + \sum_{k\in\mathbb{N}} c_k \cos(n\omega_0 t + \varphi_k). \tag{6}$$

Wave elevations of a long-crested irregular sea, for example, can be described by the sum of harmonic components (Fossen, 2011, Ch. 8.2.3)), implying the assumption of stationarity holds. Ice loads, however, are irregular and highly fluctuating. They are of *non-stationary* character (Bjerkås et al., 2007).

3.2. Energy description of a signal

The idea of Bjerkås (2006) to use a varying time-frequency decomposition in order to identify different ice load situations will be employed further. But instead of looking at the measured signal directly, an energy definition of the signal will be used. An energy distribution approach is directly applicable to non-stationary and random signals (Matz and Hlawatsch, 2003) and intuitive to interpret. The energy of a signal $s(t)$ in the time-domain is

$$E_s = \int_{-\infty}^{\infty} |s(t)|^2 dt \quad . \tag{7}$$

The energy of a signal in the frequency-domain is equivalently

$$E_s = \int_{-\infty}^{\infty} |S(f)|^2 df, \tag{8}$$

where the term $|S(f)|^2$ is the *energy spectral density*. A joint time-frequency energy density $\rho_s(t,f)$ is then implicitly defined by

$$E_s = \int_{-\infty}^{\infty}\int_{-\infty}^{\infty} \rho_s(t,f)dtdf. \tag{9}$$

Such a joint time-frequency energy density must satisfy the *marginal conditions* (Boashash, 2003), which state that if the time-frequency energy density is integrated along one of the variables, the result will be the energy density of the corresponding other variable, that is,

$$\int_{-\infty}^{\infty} \rho_s(t,f)dt = |S(f)|^2 \tag{10}$$

$$\int_{-\infty}^{\infty} \rho_s(t,f)df = |s(t)|^2. \tag{11}$$

3.3. Wigner distribution

A joint time-frequency energy density, that fulfils the marginal conditions Eqs. (10) and (11), is the Wigner distribution. The kernel $K_s(t,\tau)$ of the distribution is based on the autocorrelation function of the signal, given by

$$K_s(t,\tau) = s\left(t+\frac{\tau}{2}\right)s^*\left(t-\frac{\tau}{2}\right). \tag{12}$$

The Fourier transformation of the kernel leads further to a time-frequency energy density, denoted $W_s(t,f)$, defined as

$$\begin{aligned} \rho_s(t,f) &= \mathscr{F}\{K_s(t,\tau)\} \\ &= \int_{-\infty}^{\infty} s\left(t+\frac{\tau}{2}\right)s^*\left(t-\frac{\tau}{2}\right)e^{-j2\pi f\tau}d\tau \end{aligned} \tag{13}$$

$$= :W_s(t,f). \tag{14}$$

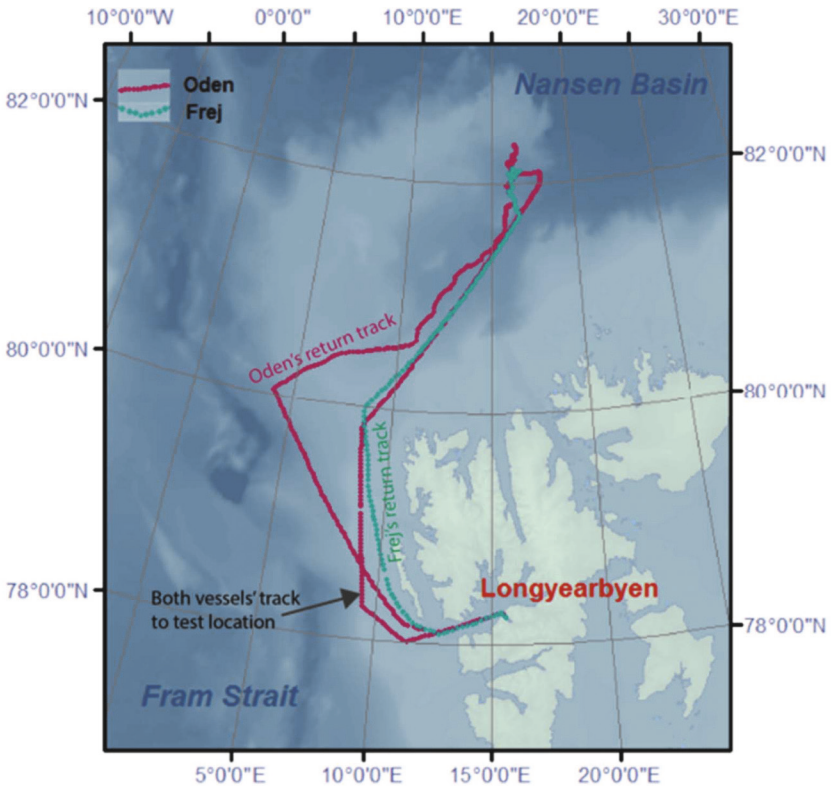

Fig. 2. Track of the icebreakers Frej and Oden (Courtesy of Wenjun Lu).

As a quadratic time-frequency distribution, the Wigner distribution leads to artefacts that compromise the interpretability of the time-frequency distribution image. An example of this effect is given in Appendix A.

3.4. Wigner-Ville distribution

The Wigner-Ville distribution can be defined exactly as the Wigner distribution (Eq. (13)) except for the chosen signal. Instead of the signal $s(t)$, the analytic associate $s_+(t)$ is used, which eliminates the frequency interference terms from the distribution. The analytic associate is defined by

$$s_+(t) = s(t) + j\mathscr{H}\{s(t)\}, \tag{15}$$

where $\mathscr{H}\{s(t)\}$ describes the *Hilbert transformation*, which removes the negative frequency components from the original signal $s(t)$. Due to the Hermitian symmetry (Eq. (5)), no information is lost. The Wigner-Ville distribution is then defined as

$$\begin{aligned} W_{s_+}(t,f) &= \mathscr{F}\{K_{s_+}(t,\tau)\} \\ &= \int_{-\infty}^{\infty} s_+\left(t+\frac{\tau}{2}\right)s_+^*\left(t-\frac{\tau}{2}\right)e^{-j2\pi f\tau}d\tau. \end{aligned} \tag{16}$$

The kernel $K_{s_+}(t,\tau)$ is referred to as *instantaneous autocorrelation function* (Boashash, 2003).

3.5. Windowed Wigner-Ville distribution

The signal $s_p(t)$ is time-limited and obtained by multiplying the signal $s(t)$ with a window function $h(t)$. The Wigner-Ville distribution is applied on the corresponding analytic associates of the signals,

$$W_{s_{p,+}}(t,f) = \int_{-\infty}^{\infty} h(\tau)s_+\left(t+\frac{\tau}{2}\right)s_+^*\left(t-\frac{\tau}{2}\right)e^{-j2\pi f\tau}d\tau. \tag{17}$$

The window function $h(t)$ causes a frequency smoothing of the time-frequency distribution (Boashash, 2003, Ch. 2.1.4.3). The use of a window function will be necessary when the system is used in a real-time system, where a sliding window function selects the available data for analysis.

3.6. Aspect of the application of the Wigner-Ville distribution on ice-induced acceleration signals

The Wigner-Ville distribution has several positive properties that are beneficial for the analysis of ice induced acceleration signals. Some important properties are summarised here, as from Flandrin (1999) and Boashash (2003).

- *Time-shift invariance*: A time shift in the signal s_+ causes the same time shift in $W_{s_+}(t,f)$. This allows moving time windows for analysing the ice induced signals in a real-time system.
- *Frequency-shift invariance*: A frequency shift in the signal s_+ causes the same shift in frequency in $W_{s_+}(t,f)$. This is needed to identify varying frequency components in the time-frequency distribution of the acceleration signals.
- *Instantaneous frequency*: The mean of the Wigner-Ville distribution is the instantaneous frequency of the signal.
- *Marginal conditions*: The Wigner-Ville distribution fulfils the marginal conditions Eqs. (10) and (11). That allows the calculation of the instantaneous power (Eq. (7)) and the energy spectrum of the

Table 2
Technical specifications of icebreaker Frej (Lubbad et al., 2016).

Icebreaker Frej	
Length	107.75 m
Beam	31.20 m
Draft	7.0 m–8.5 m
Power generation	18.6 MW
Speed in open waters	18 kts
Ice-breaking capability	1.2 m at 3 kts
Displacement	7800 t
Hydro. damping d_{11}	$2.14 \cdot 10^4$ kg·s^{-1}

signal (Eq. (8)) from the distribution.

- *Global energy*: The total energy of the signal can be evaluated with Eq. (9). This ensures that energy-changes caused by the ice interaction can be identified from the distribution.
- *Compatibility with filtering*: A convolution of two signals results in a convolution of the Wigner-Ville distributions of these two signals. This property ensures that an ice load signal can be filtered, e.g. by a lowpass filter.
- *Non-stationary signals*: It is shown by Matz and Hlawatsch (2003) that the Wigner-Ville distribution can generally also be applied on non-stationary random signals $s_r(t)$. Instead of the total energy of the signal, the mean energy is obtained by

$$\int_{-\infty}^{\infty} \int_{-\infty}^{\infty} W_{s_r,+} dt df = E\{||s_r||^2\}. \tag{18}$$

4. A measurement system for ice-induced accelerations

This section describes the measurement setup for collecting ice-induced acceleration data during an Arctic expedition with the Swedish icebreaker Frej in the Arctic Ocean north of Svalbard in September 2015.

4.1. The Oden Arctic technology research cruise 2015

The Oden Arctic technology research cruise took place in September 2015 in the Arctic Ocean north of Svalbard with the two icebreakers Oden and Frej. The track of the expedition is shown in Fig. 2, and general information about the expedition can be found in Lubbad et al. (2016). Frej is an Atle-class icebreaker, commissioned in 1975. The propulsion system consists of two fore and two aft propellers and a diesel-electric power-plant with four diesel generators. Up to three auxiliary generators provide electricity for the ship. In normal operations the generators for the propulsion system run at 495 rpm and the auxiliary generators run at 750 rpm. This information is important since the generators induced a constant vibration into the ship, which is noticeable in the vibration measurements. Table 2 summarises the technical specifications of the icebreaker.

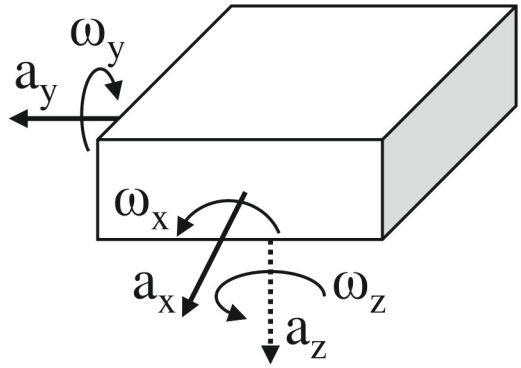

Fig. 4. IMU sensor with three accelerometers and three gyros.

4.2. Sensor configuration and specification

Four inertial measurement units (IMU) from Analog Devices were installed at various positions of the vessel; see Fig. 3. An IMU contains a tri-axis angular rate sensor and a tri-axis acceleration sensor, as illustrated in Fig. 4. Only the accelerometer data were used in this study.

One sensor (*ADIS 16480*) was placed on Deck 9, underneath the bridge level, on a firm metal beam to serve as a reference sensor. Three sensors (*ADIS 16364*) were placed in a storage compartment in the bow, close to the ice interaction zone of the vessel. The sensors in the bow

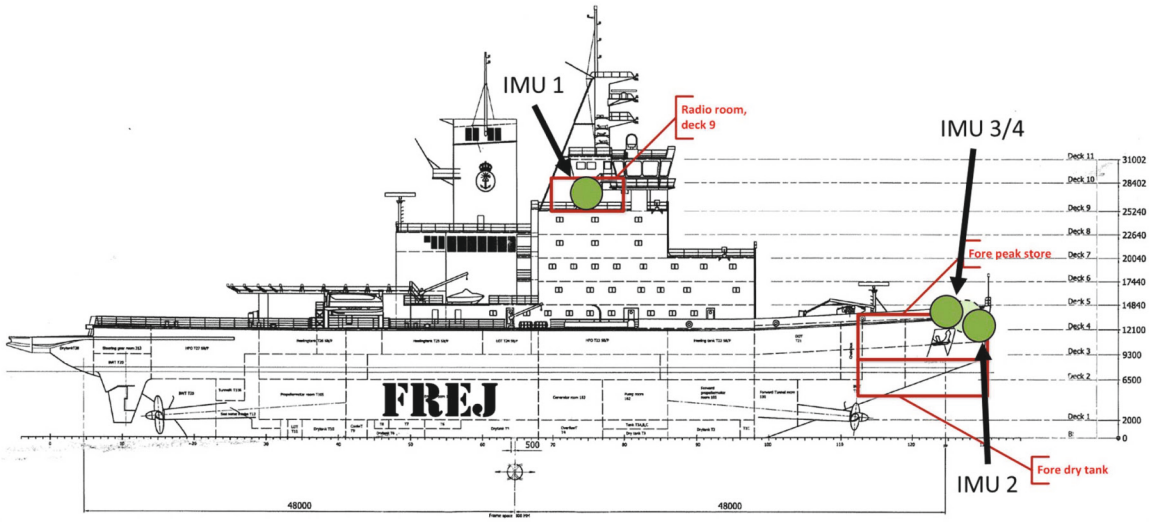

Fig. 3. Position of the motion sensors.

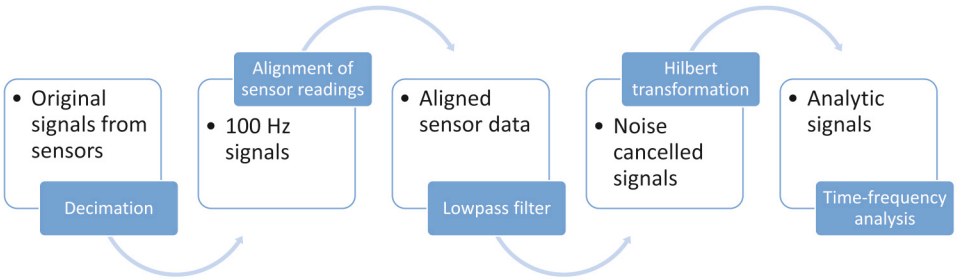

Fig. 5. Preprocessing steps for the signals from the accelerometers.

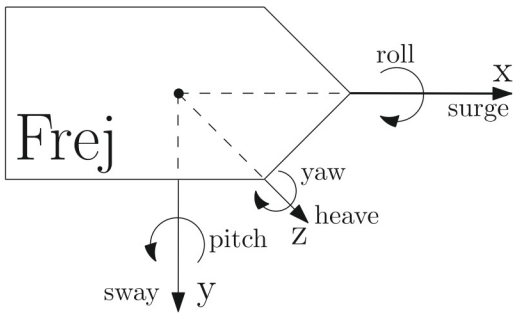

Fig. 6. Body-fixed coordinate system definition.

Table 3
Sensor orientation in relation to the body-fixed coordinate system of the ship.

	IMU 1	IMU 2	IMU 3	IMU 4
ϕ	180.18°	− 1.06°	2.10°	− 0.83°
θ	− 0.12°	208.73°	204.86°	203.94°
ψ	0°	0°	− 90.00°	90.00°

compartment were placed port, mid-ship, and starboard. The port- and starboard sensors were placed on beams directly connected to the hull of the ship. The compartment was heated to a constant temperature of 18 ° C, which minimised temperature related biases on the measurements. The *ADIS 16480* sensor contained additionally a tri-axis magnetometer, which was not used in this study.

A central server collected the data from the individual IMUs and served as time synchronisation server for the sensor units. To ensure time synchronisation during the measurements, a real-time clock in each of the sensor units was continuously synchronised with the GPS-time obtained from the ship systems. Furthermore, synchronised data from other ship systems such as the GPS system, the gyrocompass, and wind sensors, were collected. Images from a 360 ° camera system and two 180 ° cameras were also collected, synchronised and processed in order to identify the ice conditions around the vessel.

4.3. Preprocessing of sensor readings

To minimise the influence of sensor noise, to align the sensor readings and to remove the influence of cross terms in the time-frequency distribution, several preprocessing steps were executed, as summarised in Fig. 5.

4.3.1. Decimation of sensor signals

The sensors were operated with a sampling rate of 300 Hz. For the ice-induced vibrations, such a high sampling rate is not required since the ship's structure damps high frequency vibrations. To achieve a faster processing speed of the data, the signals were decimated to 100 Hz.

4.3.2. Alignment of sensor readings

For the alignment of the sensors, a body-fixed ship-wide coordinate system according to Fossen (2011) is defined, as shown in Fig. 6.

At the location of the sensor, the sensor's coordinate system is not aligned with the body-fixed coordinate system. The accelerations measured by any of the sensors in its coordinate system are denoted $\boldsymbol{a}_i^s$, and referred to as proper acceleration. The corresponding acceleration vector in the body-fixed coordinate system is denoted $\boldsymbol{a}_i^b$. The orientation-matrix $\boldsymbol{\Theta}_{s,i} = [\phi_i, \theta_i, \psi_i]^T$ states the orientation of each sensor's coordinate system relative to the body-fixed coordinate system. The orientation matrices for the four sensors are given in Table 3. A rotation matrix $\mathbf{R}_{s_i}^b(\boldsymbol{\Theta}_{s,i})$, as the result of a rotation sequence, is applied to transform all sensor readings into the body-fixed coordinate system of the ship (Fossen, 2011), according to

$$\boldsymbol{a}_i^b = \mathbf{R}_{s_i}^b(\boldsymbol{\Theta}_{s,i})\boldsymbol{a}_i^s, \tag{19}$$

with

$$\mathbf{R}_{s_i}^b(\boldsymbol{\Theta}_{s,i}) = \mathbf{R}_{z,\psi_i}\mathbf{R}_{y,\theta_i}\mathbf{R}_{x,\phi_i}.$$

Table 4
Overview of analysed measurements.

Case	Date	Seconds in measurement	Ice conditions	Ice thickness	Speed over ground
1	26.09.2017 11:19.40	1120–1200	Transit from broken ice to unbroken very close pack-ice	0.5 m–1.0 m	3.58 knots
2	26.09.2017 11:34.10	2050–2150	Broken ice, encounter of unbroken ice floe of ~100 m diameter	0.7 m	2.97 knots
3	26.09.2017 11:13.50	830–930	Broken ice, flipping of ice pieces on port side	0.3 m–0.5 m	3.74 knots
4	26.09.2017 11:40.00	2400–2500	Broken ice on starboard close pack-ice on port	0.5 m–0.7 m	4.33 knots
5	30.09.2017 10:47.40		Open-water		10.50 knots

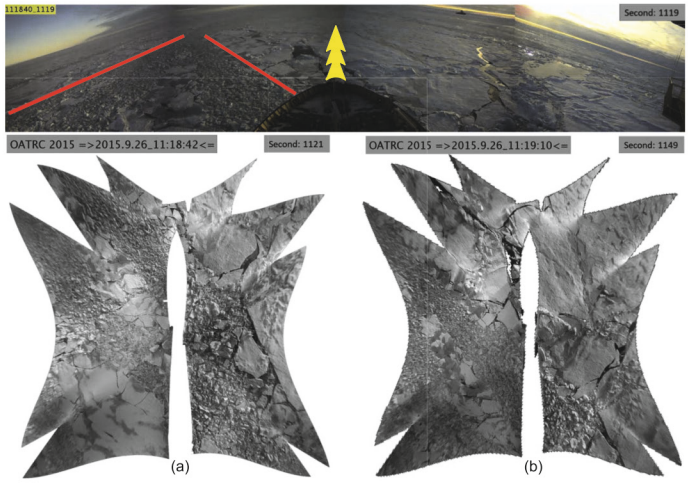

Fig. 7. Case 1: Ship leaving a channel of broken ice (a) and transits into unbroken ice (b).

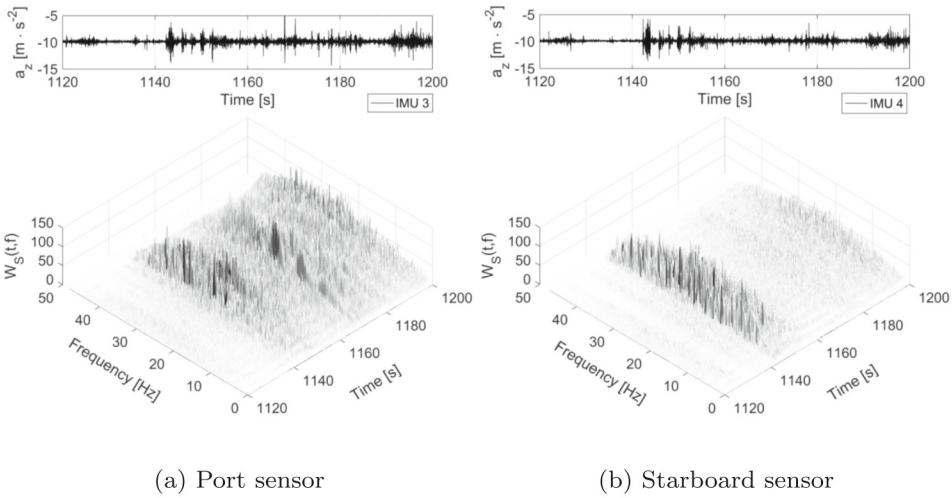

(a) Port sensor (b) Starboard sensor

Fig. 8. Case 1: Time-frequency distributions of the vertical acceleration.

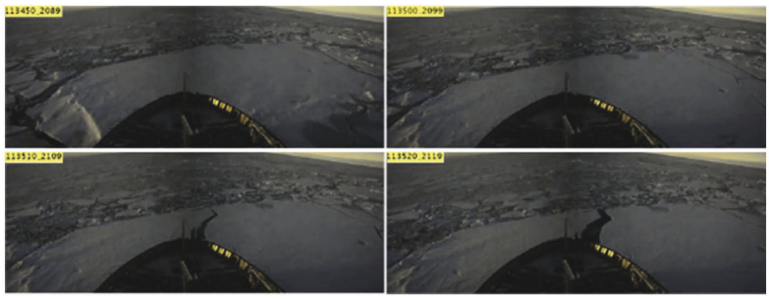

Fig. 9. Case 2: Ship encounters an unbroken ice floe which splits upon impact.

4.3.3. Lowpass and Hilbert filter

The signal has to be converted into an associated analytic signal in order to minimise the influence of cross terms in the time-frequency distribution. A lowpass filter removes high frequency noise components above 45 Hz from the signal. The sensors were calibrated and operated under a constant temperature in order to avoid a temperature related bias in the measurements.

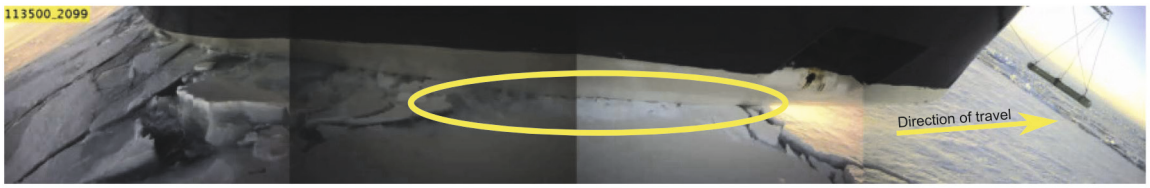

Fig. 10. Case 2: Crushing ice at starboard bow hull section just before splitting occurs.

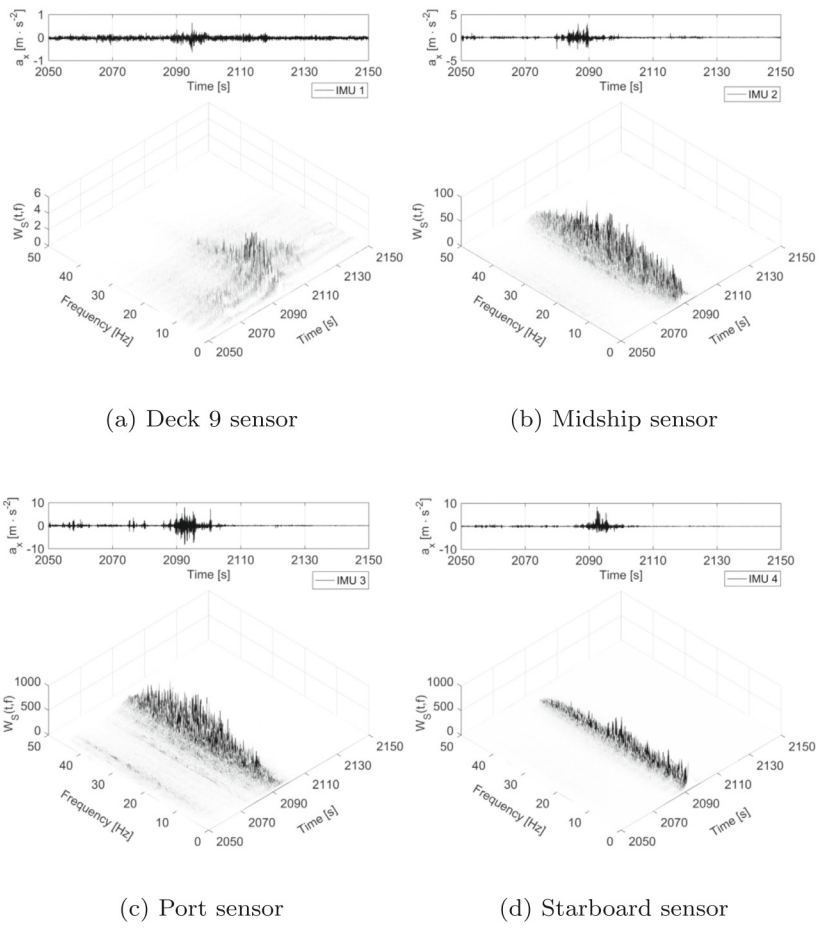

(a) Deck 9 sensor (b) Midship sensor

(c) Port sensor (d) Starboard sensor

Fig. 11. Case 2: Time-frequency distributions of the x-acceleration.

4.4. Impact load estimation from acceleration measurements

Under the assumption that sensor noise, biases, and the earth gravity influence are removed from the measurements, and that the influence of wind and waves can be neglected, the measured acceleration in the body-fixed coordinate system is

$$\boldsymbol{a}_i^b = \boldsymbol{a}_{hyd}^b + \boldsymbol{a}_{prop}^b + \boldsymbol{a}_{ice}^b + \boldsymbol{a}_{vib,i}^b, \tag{20}$$

with $\boldsymbol{a}_{hyd}^b \in \mathbb{R}^3$ describing the global hydrodynamic load, $\boldsymbol{a}_{prop}^b \in \mathbb{R}^3$ the global propellers' induced load, $\boldsymbol{a}_{ice}^b \in \mathbb{R}^3$ the global ice induced load, and $\boldsymbol{a}_{vib,i}^b \in \mathbb{R}^3$ the locally induced vibrations.

With a constant speed and heading just before the impact with an ice feature, it can be assumed that the propeller thrust compensates for the hydrodynamic forces acting against the travel direction of the vessel. If the acceleration is measured at a location with sufficient damping from locally induced vibrations, such that these can be neglected, the measured acceleration in surge direction will consist of the global ice induced impact load:

$$a_{ice,surge}^b = \mathbf{B}_x \mathbf{R}_{s_i}^b(\psi_i) \boldsymbol{a}_i^s, \tag{21}$$

where $\mathbf{B}_x = (1,0,0)$ selects only the surge acceleration. With information about the ship's mass m_{ship}, added mass m_{add} (assumed as 20% of m_{ship} for this study), linear hydrodynamic damping d_{11} for the surge direction, and velocity u_{surge}, the force acting against the vessel in surge direction is

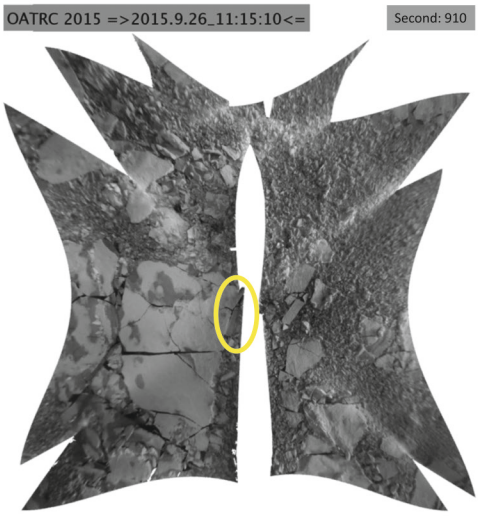

Fig. 12. Case 3: One piece of ice gets flipped by the ship.

Fig. 13. Case 3: Broken ice floe at the port side of the vessel.

$$F_{surge} = m_{11}(a^{b}_{ice,surge} + d^{-1}_{11}u_{surge}), \tag{22}$$

with

$$m_{11} = m_{ship} + m_{add}. \tag{23}$$

5. Time-frequency distributions of ship-ice interaction events

In this section several cases of ship-ice interaction events of the icebreaker Frej in the Arctic Ocean are analysed in regards to the excited frequencies in the hull vibration with the help of the Wigner-Ville distribution. The data for the cases 1 to 4 have been collected on the 26th September 2015 between 11:00 UTC and 12:00 UTC. The track of the ship is illustrated in Fig. 21. The relative wind speed was measured to be between 1 m/s and 6 m/s in the mentioned period. The influence of wind loads on the ice are neglected due to the low wind speeds. An overview of the analysed data is given in Table 4.

5.1. Case 1: transition from managed ice to unmanaged ice

The icebreaker Frej travelled at a speed of 3–4 knots inside an ice-channel created by the second icebreaker Oden. At second 1140, Frej moved out of the ice channel and hit a field of unbroken ice with an angle of about 45°. The ice was first-year ice with a thickness of 0.5 m to 1 m. The situation is shown in Fig. 7.

Fig. 8 a) and b) shows the time-frequency distribution of the ship's vertical acceleration measured by the sensors IMU 3 and IMU 4, which were placed in the bow section of the vessel. While moving in managed ice (seconds 1100–1140), significant vibrations in the hull are not noticeable. Upon entering the unbroken ice field at second 1141, the ice around the vessel failed by crushing and bending of the ice. The transition into unbroken ice is clearly visible in the time-frequency distribution due to a significant increase of energy of the signal over all frequencies. Especially vibrations with frequencies between 15 Hz and 30 Hz have a higher energy. After a few seconds the excitation decreases, but the energy of the vibrations is still significantly higher than when travelling in the broken ice.

The significant excitations upon exiting the ice channel can be connected to a sudden decrease in velocity of the vessel, which was observed. The kinetic energy upon contact with the unbroken ice might have caused a significant amount of crushing prior to bending of the ice. As soon as the ship's speed decreased, bending failure might have become the dominating failure mode again. This created significantly less vibrations than crushing, but still more than in the case of ice-interaction with already broken ice inside the ice channel.

5.2. Case 2: splitting of a major first-year ice floe

The ship encountered an unbroken ice floe with a characteristic length of about one ship length while travelling at about 3 knots through a field of broken ice. Upon impact the ship got significantly decelerated, nearly to a standstill. After about 15 s the ice floe split, and the ship moved ahead into the opening crack. The situation is shown in Fig. 9.

The resulting time-frequency distributions for the x-acceleration signals of all four sensors are shown in Fig. 11. The energy of the vibrations measured by the two sensors placed directly on the hull of the vessel (sensors IMU 3 and IMU 4) is significantly stronger between 2085 and 2010 s. The mid-ship sensor IMU 2 captured the vibration over all frequencies but with a tenth of the energy content as the sensors placed directly on hull. The reason is that the sensor IMU 2 was not placed directly on a hull segment but on a bearing beam of the foredeck. The sensor on Deck 9 (IMU 1) could not measure signal components over 20 Hz, which is due to damping of the superstructure.

It is notable, that major vibrations occur prior to the actual splitting of the ice floe. The reason might be that, due to the propagating ship, crushing occurred while the overall stress on the ice floe had increased. Upon splitting, the measured vibrations decay as the ship moves forwards inside the crack. Instead of failing, the ice was pushed away from the ship. In Fig. 10, the starboard hull section of the bow of the vessel is shown just before the splitting has occurred. Crushing of ice is visible along the hull of the vessel (see yellow marked area in the image) and it might be the cause for the broadband vibrations in the time-frequency distribution.

5.3. Case 3: port side contact with larger ice piece in broken ice field

While travelling in a field of broken ice, the ship encountered several pieces of a broken ice floe on the port side. The situation is shown in Fig. 12. While moving forward, the port section of the hull of the vessel got in contact with one piece of the broken ice floe and flipped it, as shown in the yellow marked area in Fig. 13. The first-year ice had a thickness of estimated 30 to 50 cm and the ship travelled at about 3–4 knots.

Fig. 14 shows the time-frequency distributions for the vertical accelerations measured by the hull mounted sensors. The energy content of the signals is low, because the ship moved in already managed ice.

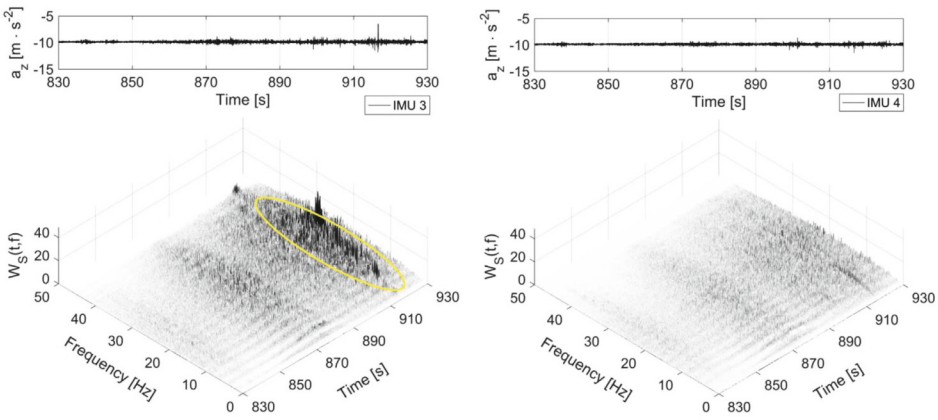

(a) Port sensor (b) Starboard sensor

Fig. 14. Case 3: Time-frequency distributions of the vertical acceleration.

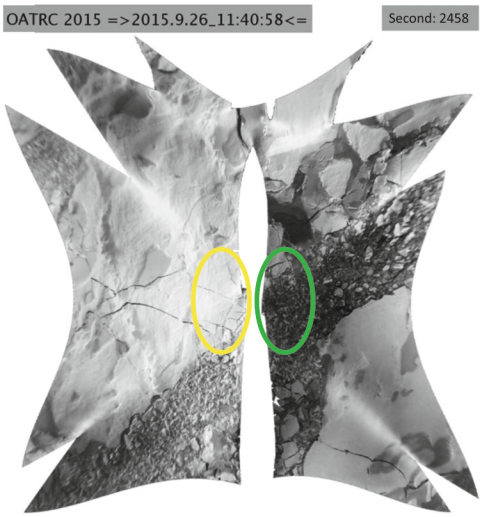

Fig. 15. Case 4: Ice fails at port side of the ship (marked yellow) while starboard side encounters broken ice pieces (marked green). (For interpretation of the references to color in this figure legend, the reader is referred to the web version of this article.)

During the time of hull contact with a piece of the broken ice floe, the port mounted sensor (IMU 3) recorded an increase in vibration energy, especially in the frequencies 5 Hz–15 Hz. The starboard sensor (IMU 4) did not record any significant change in the energy of the vibrations.

Since the piece of ice got only in contact with the port section of the hull, it makes sense, that the sensor on this side recorded the vibrations, which could have been caused by sliding of the ice piece along the hull while it flipped. The energy content of the measured vibrations is much lower than in the previous Case 2, where crushing against the hull occurred. The kinetic energy of the impact went into the rotational movement of the ice piece, and no failure of the ice piece occurred.

5.4. Case 4: bending failure on one shipside

The ship hit unbroken level-ice on the port side while travelling in a channel of broken ice. The first-year level-ice had a thickness of 50 to 70 cm. While propagating forward the unbroken ice at the port side of the ship failed by forming circumferential and radial cracks, as shown in Fig. 15 and, in more detail, in Fig. 16. The sea-ice consisted of small broken ice pieces at the starboard side of the ship.

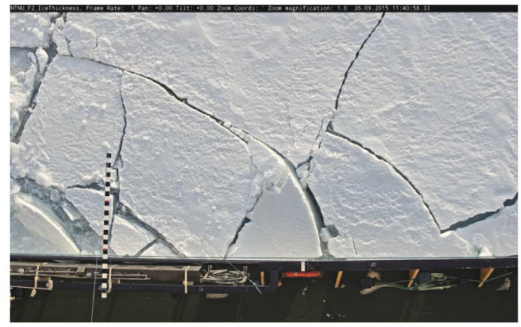

Fig. 16. Case 4: Close-up view of yellow marked area in Fig. 15. The measuring beam raster is 10 cm per block and has been mounted about 3 m above the ice. The camera is installed 20 m above the ice. Therefore the lengths taken from the measuring beam has to be multiplied by a factor of 1.2. (For interpretation of the references to color in this figure legend, the reader is referred to the web version of this article.)

The time-frequency distribution for the vertical accelerations measured by the hull mounted sensors IMU 3 and IMU 4 are shown in Fig. 17. The bending failure occurred between seconds 2450 and 2460. Both sensor registered the ice interaction. However, the energy of the measured vibrations on the side of impact, the port side, is significantly higher. Most energy is contained in the range of frequencies between 5 Hz and 25 Hz.

The high energy content of the measured accelerations must be a result of the circumferential and radial cracking, as shown in Fig. 16. In contrast to Case 3, where the piece of ice just flipped around without breaking, the ice floe actually failed against the hull of the vessel, which induced significant broadband vibrations.

5.5. Case 5: measurements in open water during a severe sea state

The ship encountered a storm on the return journey to Svalbard while travelling in open water without any ice interaction. The significant wave height was estimated to be between 5 and 7 m. The data was recorded on the 30th September 2015. The resulting time-

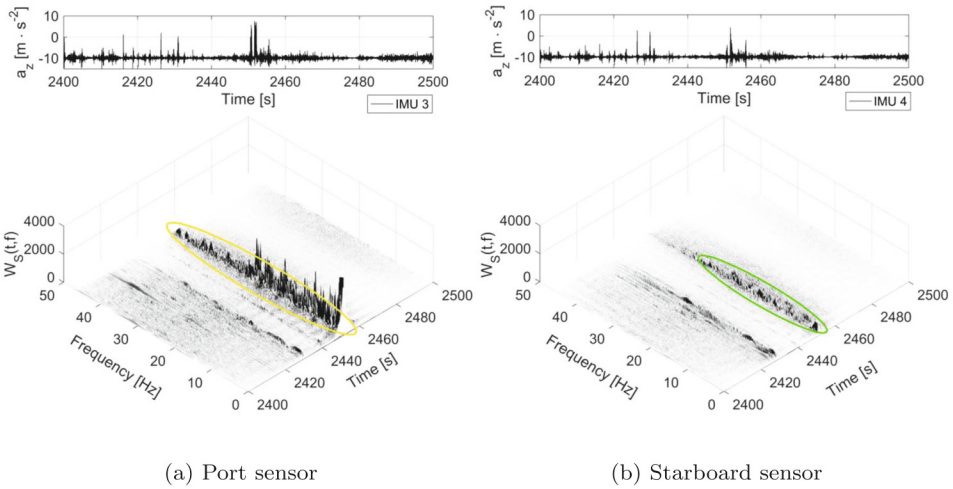

(a) Port sensor (b) Starboard sensor

Fig. 17. Case 4: Time-frequency distributions of the z-acceleration during one-sided encounter of a large piece of ice in a broken ice field.

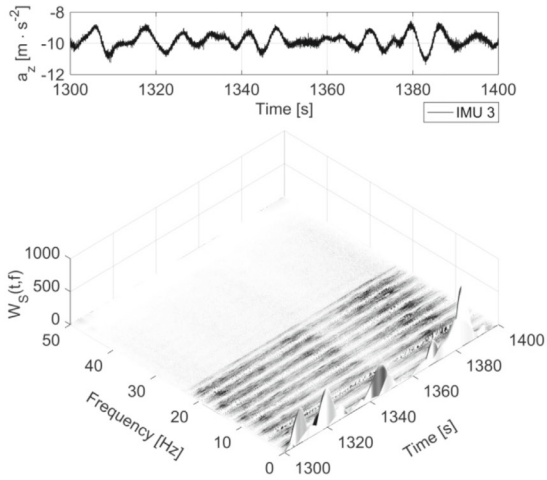

Fig. 18. Case 5: Time-frequency distributions of the vertical acceleration (IMU 3).

frequency distribution for the measured vertical acceleration of IMU 3 is shown in Fig. 18.

The most obvious property of the time-frequency distribution of the recorded vertical acceleration is the high energy content at the typical wave frequencies below 1 Hz. Furthermore, the ship hull's natural frequencies are visible. In contrast to ice-induced vibrations, there are no broadband impact events.

6. Excitation of natural frequencies of the hull

6.1. Tracking of the first natural frequency during transit in ice

In all cases, the natural modes of the hull were excited and the natural frequencies can be seen in the time-frequency distributions. A closer look at the spectral densities for different scenarios is given in Figs. 19 and 20.

Significant energy is contained in vibrations at around 2.72 Hz–2.75 Hz, 5.02 Hz–5.08 Hz, and 8.05 Hz and 9.85 Hz. The two frequencies around 2.72 Hz and 5.02 Hz correspond to the natural frequencies found by Matusiak (1982), see Table 1. The vibrations with 8.05 Hz must be originated in the engines, since the main engines ran normally at 495 rpm, which equals a frequency of about 8.25 Hz. The frequency at 9.85 Hz can be another higher natural mode, not present during the measurements on the sistership Sisu in 1982. It has to be noted, that the ship Frej has been significantly modified since it's launch in 1975.

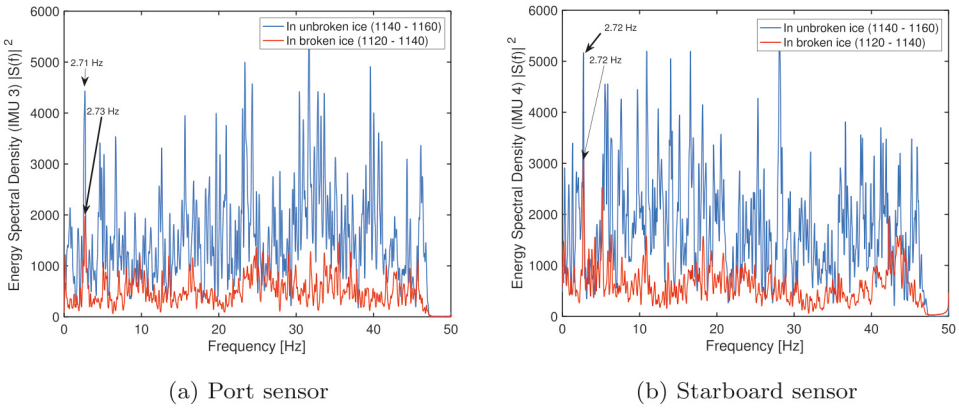

Fig. 19. Case 1: Energy spectral density of the vertical acceleration during transit from broken to unbroken ice.

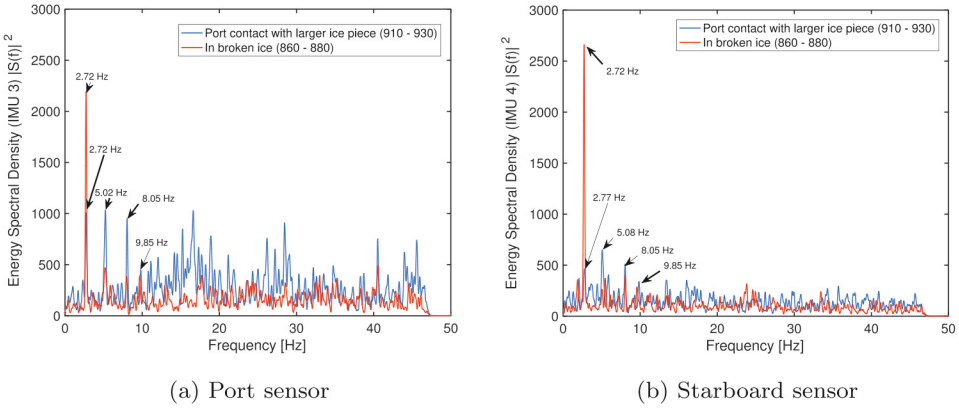

Fig. 20. Case 3: Energy spectral density of the vertical acceleration during port-sided encounter of a larger piece of ice.

Matusiak (1982) mentions that the first natural frequency decreases, depending on the ice thickness, when travelling in ice. To investigate this behaviour, the resulting Wigner-Ville distribution was used to automatically determine the first natural frequency in the measured acceleration signal of IMU 1 during transit in an ice field with broken and unbroken ice, as illustrated in Fig. 21. The result of the tracking of the first natural frequency is presented in Fig. 22, and plotted together with the estimated ice induced impact load. The impact load has been calculated from the measurements of IMU 1 using Eq. (22), and the parameters given in Table 2. A lowpass filter, set with a cut-off frequency at 7.5 Hz was applied to the acceleration signal. A running average filter has been applied on the resulting load estimate in order to make the load trend better.

The first natural frequency ξ_1 measured by IMU 1 occurs in the frequency band 2.67 Hz to 2.77 Hz. It is notable, that a lower first natural frequency (lower than 2.70 Hz) occurs always during an increase in induced ice load and upon impact with an unbroken ice floe. A higher first natural frequency (higher than 2.74 Hz) corresponds with transit in broken ice between the unbroken ice floes.

7. Conclusion

This study proposed the Wigner-Ville distribution for the time-frequency analysis of ice-induced accelerations during transit with an Atle-class icebreaker. The resulting time-frequency spectra motivates the development of accelerometer based sensor system for ships operating in ice-infested waters.

The interaction with sea-ice induces vibrations into the ship's hull with frequency components up to 25 Hz, and especially crushing as failure mode induces high-frequency vibration in the hull of the vessel. Natural frequencies of the ship's hull up to 7.5 Hz are globally measurable, and high-frequency vibration are only locally measurable. Measuring ice induced accelerations locally at several points along the ship's hull allows therefore for the localisation of ice action against the ship along the ship's hull. Each failure regimes of the ice induces a unique frequency pattern, which allows for the detection of the acting failure mode during ship-ice interaction.

Accelerometers are capable of tracking the excitation of the ship's hull natural frequencies. Depending on the ice-condition around the vessel, the natural frequencies change. Matusiak (1982) claimed that this change in the natural frequencies is due to a change in added mass when an ice floe is attached to the ship's hull. It was shown, that a lower first natural frequency occurs upon impact of the vessel with an unbroken ice floe (Case 3). Just before the splitting occurred, the ship's bow was well pressing against the unbroken ice floe and the measured first natural frequency decreased to 2.675 Hz. After splitting had occurred, the bow of the vessel moved into the open water inside the split and the first natural frequency increased to 2.760 Hz, which, according to Eq. (3) corresponds to a loss of mass of 1.55%. The reason can be, that the additional mass of the ice floe was not in contact with the ship's hull anymore.

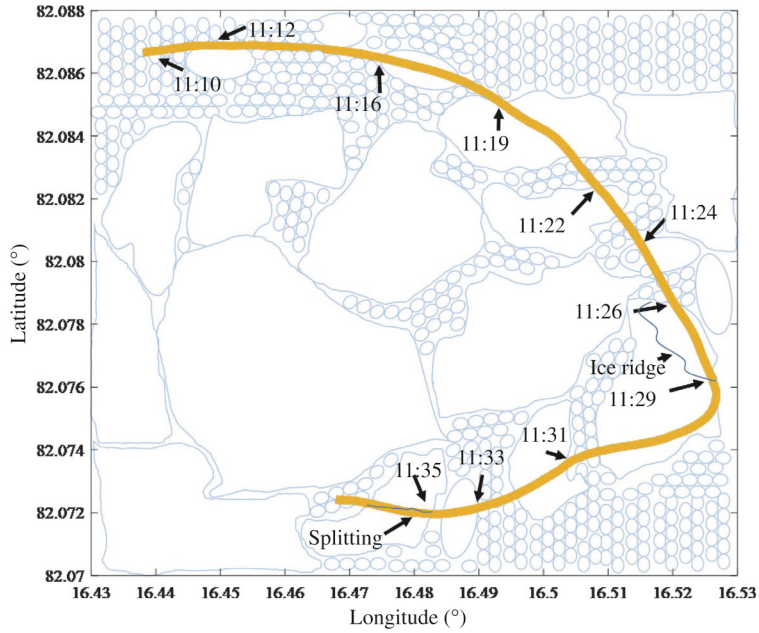

Fig. 21. Illustration of encountered icefield.

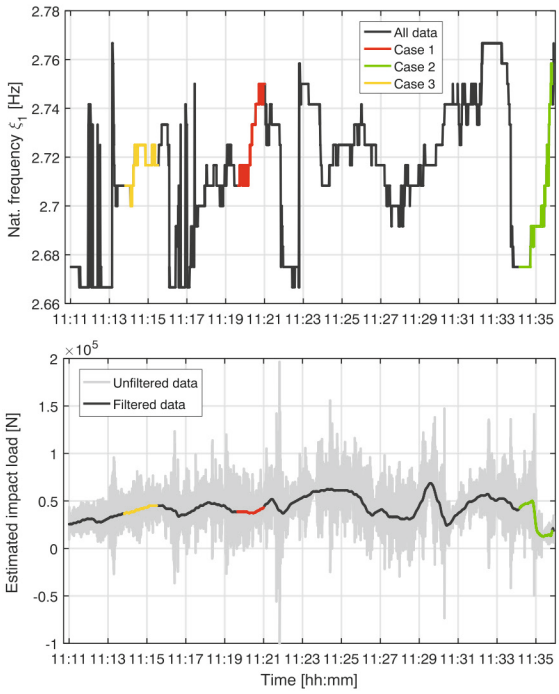

Fig. 22. Track of first natural frequency and estimated impact load during transit in icefield.

7.1. Further work

The shift of natural frequency upon impact with ice floe can be used for an estimation of the ice mass during ship-ice interaction, as already mentioned by Matusiak (1982). With the addition of IMUs on a vessel, a system could be realised, that estimates in real-time the mass of any ice feature the ship get in contact with. By locally tracking high frequent vibrations in the hull, a warning upon occurrence of crushing against the hull can be issued to the crew of an ice-going vessel.

Only global and local acceleration measurements during transit were available for this study. Additional work should be conducted in collecting acceleration data during stationkeeping, and analyse if scenarios like accumulation of ice on one side of the stationkeeping vessel can be detected with local vibration measurements in the hull.

Acknowledgments

The authors would like to thank the Research Council of Norway (RCN) for financial support through projects 203471 CRI SAMCoT and 223254 CoE AMOS. Oden Arctic Technology Research Cruise 2015 (OATRC2015) was supported by the ExxonMobil Upstream Research Company and performed by the Norwegian University of Science and Technology (NTNU) through the SAMCoT CRI and in cooperation with the Swedish Polar Research Secretariat (SPRS) and the Swedish Maritime Administration (SMA). Furthermore, the authors are grateful for the extraordinary hospitality and support received from the crews of the icebreakers Frej and Oden and the Swedish Maritime Administration (SMA).

The authors would like to thank Professor Sveinung Lø set, Professor Raed Lubbard, Dr. Wenjun Lu, Dr. Øivind Kjerstad, and Thorvald Grimstad for their help, input, and valuable discussions during and after the expedition.

Appendix A

A.1. Interference term in the Wigner distribution

An example from Boashash (2003) explains the interference effect: A signal with constant frequency f_c is given as $s(t) = \cos(2\pi f_c t)$.

The kernel of the corresponding Wigner distribution is given by:

$$\begin{aligned} K_s(t,\tau) &= s\left(t+\frac{\tau}{2}\right)s^*\left(t-\frac{\tau}{2}\right) \\ &= \cos\left(2\pi f_c\left(t+\frac{\tau}{2}\right)\right)\cdot\cos\left(2\pi f_c\left(t-\frac{\tau}{2}\right)\right) \\ &= 0.5\cdot\cos(2\pi f_c\tau) + 0.5\cdot\cos(2\pi f_c t), \end{aligned}$$

and the Fourier transformation leads further to the time-frequency energy density

$$\begin{aligned} W_s(t,f) &= \mathscr{F}\{K_s(t,\tau)\} \\ &= 0.25\cdot\delta(f-f_c) + 0.25\cdot\delta(f+f_c) \\ &+ 0.5\cdot\cos(4\pi f_c t)\delta(f). \end{aligned} \tag{24}$$

The last term in Eq. (24) is the interference between the positive- and negative frequency components of the real signal (Boashash, 2003).

References

Arctic Council, 2009. Arctic Marine Shipping Assessment 2009 Report. Technical Report Arctic Council.

Belov, I.M., Spiridonov, N.N., 2012. Features of ship vibration in ice operation conditions. Twenty-second (2012) Int. Offshore Polar Eng. Conf. 4, 1223–1228.

Bhat, S.U., Choi, S.K., Wierzbicki, T., Karr, D.G., 1991. Failure analysis of impacting ice floes. J. Offshore Mech. Arct. Eng. 113, 171–178.

Bjerkås, M., 2006. Wavelet transforms and ice actions on structures. Cold Reg. Sci. Technol. 44, 159–169.

Bjerkås, M., Skiple, A., Iver Røe, O., 2007. Applications of continuous wavelet transforms on ice load signals. Eng. Struct. 29, 1450–1456.

Boashash, B., 2003. Time Frequency Signal Analysis and Processing. Elsevier.

Eik, K., 2008. Review of experiences within ice and iceberg management. J. Navig. 61, 557–572.

Flandrin, P., 1999. Time-frequency/Time-scale Analysis. vol. 10 Academic Press, London.

Flandrin, P., Auger, F., Chassande-Mottin, E., 2002. Time-frequency Reassignment from Principles to Algorithms. CRC Press, pp. 179–203 Chapter 5.

Fossen, T.I., 2011. Handbook of Marine Craft Hydrodynamics and Motion Control. Wiley Sons, Ltd.

Hamilton, J., Holub, C., Blunt, J., Mitchell, D., Kokkinis, T., 2011. Ice management for support of Arctic floating operations. In: Arctic Technology Conference.

Haugen, J., Imsland, L., Løset, S., Skjetne, R., 2011. Ice observer system for ice management operations. In: Proceedings of the Twenty-first International Offshore and Polar Engineering Conference.

Hoffmann, R., Wolff, M., 2014. Intelligente Signalverarbeitung 1. Springer Vieweg.

Hossain, K., Koivurova, T., Zojer, G., 2014. Arctic Marine and Governance and Opportunities for and Transatlantic Cooperation. Understanding Risks Associated with Offshore Hydrocarbon Development. Springer, pp. 159–176.

ISO/FDIS/19906:2010, 2010. Petroleum and Natural Gas Industries — Arctic Offshore Structures. In: International Organization for Standardization, Geneva, Switzerland.

Løset, S., Shkhinek, K.N., Gudmestad, O.T., Høyland, K.V., 2006. Actions from Ice on Arctic Offshore and Coastal Structures. LAN.

Lu, W., Lubbad, R., Høyland, K., Løset, S., 2015a. Physical model and theoretical model study of level ice and wide sloping structure interactions. Cold Reg. Sci. Technol. 101, 40–72.

Lu, W., Lubbad, R., Løset, S., 2015b. In-plane fracture of an ice floe: a theoretical study on the splitting failure mode. Cold Reg. Sci. Technol. 110, 77–101.

Lubbad, R., Løset, S., 2011. A numerical model for real-time simulation of ship-ice interaction. Cold Reg. Sci. Technol. 65.

Lubbad, R., Løset, S., Hedman, U., Holub, C., Matskevitch, D., 2016. Oden Arctic Technology Research Cruise 2015. In: Arctic Technology Conference, http://dx.doi.org/10.4043/27340-MS.

Lubin, D., Massom, R., 2006. Polar Remote Sensing. Sea Ice. Springer, pp. 308–728.

Masterson, D.M., Spencer, P.A., Nevel, D.E., Nordgren, R.P., 1999. Velocity effects from multi-year ice tests. In: 18th International Conference on Offshore Mechanics and Arctic Engineering.

Matusiak, J., 1982. Dynamic Loads and Response of Icebreaker Sisu During Continuous Icebreaking. Technical Report. Winter Navigation research board, Helsinki.

Matz, G., Hlawatsch, F., 2003. Wigner distributions (nearly) everywhere: time-frequency analysis of signals, systems, random processes, signal spaces, and frames. Signal Process. 83, 1355–1378.

Ohm, J.-R., Lüke, H.D., 2010. Signalübertragung. Springer.

Riska, K., 2011. Ship-ice Interaction in Ship Design: Theory and Practice. In: Encyclopedia of Life Support Systems (EOLSS), Developed under the Auspices of the UNESCO. Eolss Publisher.

Sodhi, D.S., 1991. Ice-Structure Interaction During Indentation Tests. In: Ice-Structure Interaction. Springer Berlin Heidelberg, Berlin, Heidelberg, pp. 619–640. http://dx.doi.org/10.1007/978-3-642-84100-2_31.

Su, B., Riska, K., Moan, T., 2010. A numerical method for the prediction of ship performance in level ice. Cold Reg. Sci. Technol. 60.

Yue, Q., Guo, F., Krn, T., 2009. Dynamic ice forces of slender vertical structures due to ice crushing. Cold Reg. Sci. Technol. 56.

Yue, Q., Qu, Y., Bi, X., Krn, T., 2007. Ice force spectrum on narrow conical structures. Cold Reg. Sci. Technol. 49, 161–169.

Chapter 8

Applications of motion sensing for local ice condition assessment

8.1 Ice condition assessment during transit in sea ice

Ice condition assessment using onboard accelerometers and statistical change detection

Hans-Martin Heyn, *Member, IEEE,* Mogens Blanke, *SM, IEEE,* Roger Skjetne, *SM, IEEE,*

***Abstract*—The presence of sea ice is the predominant risk for ship operations in the Arctic, and monitoring of ice condition around a vessel is crucial during all times of operation. This paper presents a system for online onboard assessment of ice condition. It is demonstrated that ice-induced accelerations in the bow section of the hull follow a bivariate t-distribution and that parameters of the distribution have a one to one relation to ice condition. The paper suggests a methodology to monitor the ice condition in real time through estimation of parameters that characterise the distribution of hull accelerations. It is shown how a Kullback-Leibler divergence measure can classify ice condition among a set of pre-trained conditions. An absolute measure of ice load is suggested as an alternative for situations when pre-training data are not available. The alternative algorithm quantifies the condition through the entropy of measured accelerations. The article presents a computationally easy methodology and tests against data collected during Arctic transit of an icebreaker. Further, the classification results are compared with the results from two standard methods from machine learning, decision tree and a support vector machine approaches. The results show that the statistical methods provide robust assessment of the prevailing ice conditions, independent of visual and weather conditions. The also comparison shows that the statistical classification methods, designed by process knowledge, provide steadier and more reliable results.**

Keywords*—Arctic; bivariate t-distribution; entropy; generalised log-likelihood ratio; IMU; Kullback-Leibler divergence; machine learning; ocean engineering; sea ice; ship-ice interaction, statistical change detection.

I. Introduction

Operations in the Arctic are heavily influenced by ice loads as the predominant risk factor. Accidents impairing the fragile environment of the Arctic have to be avoided at any cost [1]. Therefore, ice management ensures that ice loads on a protected vessel do not exceed its structural and operational safety limits [2]. Ice management relies on ice intelligence, which is the process of collecting and processing information about the ice environment [3], [4]. It is beneficial to collect this information in situ, without the need of external platforms such as satellites, drones, or buoys. The system collecting the information should be able to operate without weather-related

Hans-Martin Heyn is with the Department of Marine Technology, Norwegian University of Science and Technology, Trondheim, Norway e-mail: martin.heyn@ntnu.no

Mogens Blanke is with the Automation and Control Group, Department of Electrical Engineering, Technical University of Denmark, Kgs. Lyngby, Denmark e-mail: mb@elektro.dtu.dk

Roger Skjetne is with the Department of Marine Technology, Norwegian University of Science and Technology, Trondheim, Norway

Manuscript submitted January 06, 2019;

Nomenclature

$\boldsymbol{a}_{ib}^{b}$	Dynamic acceleration at at origin of body frame
$\boldsymbol{a}_{is}^{b}$	Dynamic acceleration at sensor location
$B(x,y)$	Beta function
$\boldsymbol{b}_{as}^{b}$	Sensor bias
$\boldsymbol{c}$	Mean vector
D_{kl}	Kullback-Leibler divergence
$\mathcal{F}$	Smooth function
$\boldsymbol{f}_{i,s}^{b}$	Specific force denoted in body frame
$\boldsymbol{f}_{i,s}^{s}$	Specific force denoted in sensor frame
$f(x;\mu,s,\nu)$	Univariate t-distribution
$f(\boldsymbol{x};\boldsymbol{\theta})$	Multivariate t-distribution
$f(\boldsymbol{z};\boldsymbol{\theta})$	Bivariate t-distribution
$\mathcal{G}$	Cumulative distribution
$G_i^k(\hat{\boldsymbol{\theta}},\boldsymbol{\theta}_p)$	Test statistic defined in (27)
$\bar{\boldsymbol{g}}_n$	Gravitational vector
g	Standard gravity (9.80665 m·s^{-2})
$g(k,\hat{\theta})$	Test statistic of best fitting trained ice condition
$h_{\mathcal{G}}$	Threshold for seperation of ice conditions
$H(\boldsymbol{\theta})$	Statistical entropy for bivariate t-distribution
$\mathcal{H}_p$	Hypothesis that trained ice condition p fits best
$\mathcal{H}_{\neq p}$	Hypothesis that any other condition besides p fits better
k	Running index for sliding data window
$\boldsymbol{\mathcal{L}}_i^k$	Log-likelihood function
$\boldsymbol{l}_s^b$	Lever arm length
N	Length of sliding data window
P	The set of all trained ice conditions
P_{class}	Probability of classification
$\boldsymbol{p}_{\boldsymbol{bs}}^{\boldsymbol{b}}$	Position of sensor in regards to body frame
$\boldsymbol{p}_{\boldsymbol{CO}}^{\boldsymbol{b}}$	Position of centre of orientation
p	Index for trained ice condition
$p(k)$	Declared ice condition
$\boldsymbol{R}_n^b$	Rotation matrix between NED frame and body frame
$\boldsymbol{R}(\boldsymbol{\Theta})$	Rotation matrix with orientation $\boldsymbol{\Theta}$
$\boldsymbol{S}$	Correlation matrix
s	Scale parameter
$\boldsymbol{w}_{as}^{b}$	Sensor noise
$\boldsymbol{z}_i^k$	Sliding data window
$\boldsymbol{\alpha}_{ib}^{b}$	Angular acceleration
$\Gamma(x)$	Gamma function
θ	Pitch angle
$\boldsymbol{\theta}$	Parameters set
$\hat{\boldsymbol{\theta}}$	Estimated parameter set
$\boldsymbol{\theta}_p$	Parameter set for a trained ice condition p
μ	Location parameter
ν	Degrees of freedom
$\boldsymbol{\xi}_s^b$	Local vibration component
ϕ	Roll angle
$\Psi(x)$	Digamma function
ψ	Yaw angle
$\omega(\boldsymbol{x};\boldsymbol{\theta})$	See (10)
$\boldsymbol{\omega}_{ib}^{b}$	Angular rate

limitations. It should be possible to process ice information in real-time into a format, which is useful as decision support for operators, and which can be used as input to a control and monitoring system.

Present ship-based ice observation systems employ optical cameras, e.g. [5], [6], and image processing extracts information such as ice concentration, floe size distribution [7]–[11], and ice thickness [12]. Camera based ice intelligence becomes unavailable in harsh weather conditions, such as fog or heavy snow. Shipborne synthetic aperture radar (SAR) systems can help to identify ice fields, but SAR is unreliable in the close vicinity of the vessel [13]–[15]. Inertial measurement units (IMUs) provide direct information about exterior loads on the vessel. IMUs are inexpensive, easy to install, and do not depend on weather conditions. Johnston et al. [16] showed that shipboard IMUs provide global loads from interaction with sea ice. Kjerstad et al. [17], [18] extended the approach to four distributed IMUs. These approaches provided global load information. It is desired to obtain spatial information about the surrounding ice, taking into account that the ship's hull is not a rigid, but rather a flexible and deformable body. Strain gauges measure strain and bending. Locally induced ice loads can be extracted from such measurements [19], [20]. In contrast to IMUs, strain gauges are time-consuming to install, and thus expensive [21]. This study therefore focus on the problem of assessing local ice condition based on measurements by IMUs placed in the hull of the ship.

Changes in ice load depend on the vessel's velocity, shape of the hull, and on the properties of the ice, such as density, thickness, and salinity [22], [23]. The properties of the ice have a large local variability, which results in sudden changes in magnitude of the ice-induced loads, especially upon the encounter of ice ridges [24]. Studies conducted with data from strain gauges suggested that the measured ice loads could be described statistically [25], e.g., by a Weibull distribution [26], by a log-normal distribution [19], or by a 3-parameter exponential distribution [27]. The Weibull and log-normal distributions are heavy tailed distributions. A recent study [28] showed that local ice-induced vibrations, measured by IMUs in the hull of an icebreaker, follow a non-central, scaled t-distribution, where the shape changes with the ice condition.

The goal of the paper is to develop and validate a fast, online, shipborne ice assessment system based on the estimation of parameters in the distribution of local accelerations. Data from in-plane accelerometers are used to find a statistical model of local ice-induced accelerations. Typical distribution parameters for four ice conditions are determined using training data. Under operations, the distribution parameters are estimated for small time windows and compared to the parameter sets from the trained ice conditions. The paper proposes two custom methods to assess ice-induced hull accelerations: Method one employs a modified Kullback-Leibler divergence to find the trained ice condition that best describes the measured data. Method two utilises directly the change in signal entropy to classify the severity of ice loads. The results from both classification approaches are validated using data obtained during the transit of an icebreaker. Data from a camera system that observed the *visual ice condition* is used for reference. Furthermore, the classification results are compared with the results from two trained machine learning classification models, namely a trained decision tree model and a trained support vector machine (SVM) model.

TABLE I: Technical data of icebreaker Oden [31].

Length	107.75 m
Beam	31.2 m
Draft	7.0 - 8.5 m
Total power	18 MW
Speed in open water	15 knots
Icebreaking capability	1.9 m level ice at 3 knots
Bunker capacity	4600 m^3
Displacement	11.000 - 13.000 t
Propulsion	4 medium speed diesel engines 2 propellers in nozzles

The paper is structured as follows. Section II introduces the experiment setup and documents training data for different ice conditions. Section III describes how ice-induced accelerations are modelled by a bivariate t-distribution and derives a maximum-likelihood estimator for recursive parameter estimation of the distribution. Section IV presents the statistical methods for ice condition classification seconded by two standard machine learning approaches. Section V validates the classification approaches with data sets obtained onboard an icebreaker. Furthermore, the section also presents a comparison between the custom classification approaches and the two trained machine learning models. Section VI assess the robustness of results and suggests how the monitoring technology could best be applied. A final section provides discussion of results and conclusions.

II. Problem formulation

The problem at hand is to determine the ice condition and to capture changes in ice condition at a section of the ship's hull from local acceleration measurements in the interior structure. The detection of a change in ice condition must be fast enough to detect sudden changes in ice thickness, which typically occur when the ship encounters an ice ridge [19], [29]. The system must therefore detect changes within seconds to give enough time for the crew or a control system to prevent getting locked-in ice.

A. Measurement setup

A test system was established with two IMUs installed on the Swedish icebreaker Oden during the Arctic Ocean 2016 expedition [30]. A summary of the icebreaker's technical specifications is given in Table I.

Figure 1 illustrates the placement of sensors. IMU 1 was installed close to the geometrical centre of symmetry of the hull. Its purpose was to provide reference data of the global accelerations acting on the vessel. IMU 2 was installed inside the hull, at the ice knife of the vessel. This unit recorded local vibrations in the bow section of the hull. The data provided by IMU 2 will be used for the ice diagnostic system, with the aim to detect changes in ice condition at the bow section. The full technical specifications of the IMUs can be found in [32].

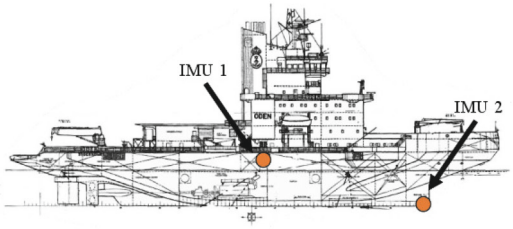

Fig. 1: Placement of the inertial measurement units (IMUs).

TABLE II: Placement of IMUs relative to CO.

		IMU 1	IMU 2
$\boldsymbol{\iota}_s^b$	x	0 m	33.95 m
	y	0 m	0 m
	z	0 m	-8.39 m
$\boldsymbol{\Theta}_{bs}$	ϕ_s	$-0.58°$	$-2.90°$
	θ_s	$180.45°$	$180.05°$
	ψ_s	$106.00°$	$90.00°$

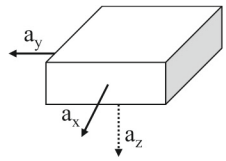

Fig. 2: IMU sensor containing three accelerometers.

B. Model of the sensor data

Each sensor contains three orthogonal accelerometers as illustrated in Figure 2. The three accelerometers record the specific forces, $\boldsymbol{f}_{is}^s \in \mathbb{R}^3$ in the sensor frame $\{s\}$ with respect to an inertial frame $\{i\}$. A rotation matrix $\boldsymbol{R}(\boldsymbol{\Theta}_{bs})$ (see [33], Eq. 2.18), transforms the recorded specific forces to the ship's body frame $\{b\}$, where $\boldsymbol{\Theta}_{bs} = (\phi_s, \theta_s, \psi_s)$ describes the orientation of the sensor, see Table II:

$$\boldsymbol{f}_{is}^b = \boldsymbol{R}(\boldsymbol{\Theta}_{bs})\boldsymbol{f}_{is}^s. \tag{1}$$

The rotated sensor output for the accelerations is modelled in standard literature, [33], [34]:

$$\boldsymbol{f}_{i,s}^b = \boldsymbol{a}_{is}^b - \boldsymbol{R}_n^b \bar{\boldsymbol{g}}^n + \boldsymbol{b}_{a_s}^b + \boldsymbol{w}_{a_s}^b, \tag{2}$$

where $\boldsymbol{a}_{is}^b \in \mathbb{R}^3$ is the dynamic acceleration in the location s of the sensor with respect to $\{i\}$, $\boldsymbol{R}_n^b \in \mathbb{R}^{3\times3}$ is the rotation matrix between the north-east-down (NED) frame $\{n\}$ and $\{b\}$, $\bar{\boldsymbol{g}}^n = (0, 0, g)$ is the gravitational vector [34] in $\{n\}$, $\boldsymbol{b}_{a_s}^b \in \mathbb{R}^3$ contains the sensor bias, and $\boldsymbol{w}_{a_s}^b \in \mathbb{R}^3$ accounts for the sensor noise. The translational accelerations $\boldsymbol{a}_{is}^b$ can be transferred to the origin b of the ship's body frame (i.e., the centre of orientation (CO)),

$$\boldsymbol{a}_{ib}^b = \boldsymbol{a}_{is}^b - \boldsymbol{S}(\boldsymbol{\omega}_{ib}^b)^2 \boldsymbol{l}_s^b - \boldsymbol{S}(\boldsymbol{\alpha}_{ib}^b)\boldsymbol{l}_s^b, \tag{3}$$

where $\boldsymbol{\omega}_{ib}^b \in \mathbb{R}^3$ and $\boldsymbol{\alpha}_{ib}^b = \dot{\boldsymbol{\omega}}_{ib}^b$ are the angular velocities and accelerations of b relative to $\{i\}$, respectively, and $\boldsymbol{l}_s^b = \boldsymbol{p}_{bs}^b - \boldsymbol{p}_{\mathrm{CO}}^b$ is the lever arm from $\{b\}$ to $\{s\}$. $\boldsymbol{S}(\boldsymbol{\omega})$ is the skew-symmetric matrix, that represents the cross product operator $\boldsymbol{\omega}\times$,

$$\boldsymbol{S}(\boldsymbol{\omega}) = \begin{bmatrix} 0 & -\omega_z & \omega_y \\ \omega_z & 0 & -\omega_x \\ -\omega_y & \omega_x & 0 \end{bmatrix}. \tag{4}$$

The measured accelerations $\boldsymbol{f}_{i,s}^b$ at the sensor's location contain a translational component $\boldsymbol{a}_{is}^b$, and in addition a local vibration component $\boldsymbol{\xi}_s^b$, which is typically damped out through the flexibility of the hull structure and attenuated in the vessel's origin b. Hence, an IMU located in CO may not feel the local vibration component at the bow; however, when transforming the measurements $\boldsymbol{f}_{i,s}^b$ in s to CO, the vibrations are part of the signal, according to

$$\begin{aligned} \boldsymbol{a}_{ib}^b &= \tilde{\boldsymbol{a}}_{is}^b - \boldsymbol{S}(\boldsymbol{\omega}_{ib}^b)^2 \boldsymbol{l}_s^b - \boldsymbol{S}(\boldsymbol{\alpha}_{ib}^b)\boldsymbol{l}_s^b \\ &= \boldsymbol{f}_{i,s}^b + \boldsymbol{R}_n^b \bar{\boldsymbol{g}}^n - \boldsymbol{S}(\boldsymbol{\omega}_{ib}^b)^2 \boldsymbol{l}_s^b - \boldsymbol{S}(\boldsymbol{\alpha}_{ib}^b)\boldsymbol{l}_s^b \\ &\quad - \boldsymbol{b}_{a_s}^b - \boldsymbol{\xi}_s^b - \boldsymbol{w}_{a_s}^b, \end{aligned} \tag{5}$$

with $\tilde{\boldsymbol{a}}_{is}^b = \boldsymbol{a}_{is}^b - \boldsymbol{\xi}_s^b$ being the vibration free acceleration at the sensor's location. The rotated in-plane specific forces $f_{is,x}^b$ and $f_{is,y}^b$ were utilised in this study.

C. Mapping of roll- and pitch angles from acceleration measurements

Under operations, the ship experiences roll and pitch motions, which change the attitude angle of the ship. Under the assumptions that the average acceleration with respect to the environment is zero for a sufficiently large data window [33] and the accelerometers are calibrated to remove bias, the total additional roll and pitch angles experienced by the sensors can be estimated by:

$$\phi_{add} \approx \operatorname{atan2}\left(-\bar{a}_y, -\bar{a}_z\right) \tag{6}$$

$$\theta_{add} \approx -\operatorname{atan2}\left(\bar{a}_x, \sqrt{\bar{a}_y^2 + \bar{a}_z^2}\right), \tag{7}$$

where $\operatorname{atan2}(y, x)$ provides an angle in the interval $(-\pi, \pi]$. If gyro data were available, they could be utilised to enhance the precision of the attitude estimation, using an extended Kalman filter or nonlinear observers; see [35].

D. Preprocessing

Preprocessing of accelerometer data were performed as follows:

- To assure that sensor noise is not entering the diagnostic system, and to accelerate processing, the data recorded at 100 Hz, were decimated to 20 Hz, with prior lowpass filtering to 10 Hz and subsequent downsampling. It was shown in [36], [37] that a frequency spectrum up to 10 Hz allows for the capture of relevant ice-induced hull vibrations. The utilised lowpass filter was a Chebyshev Type I filter of order 8 with a passband ripple of 0.05 dB.
- Each accelerometer was calibrated to minimise the measurement bias.

- Influence of roll and pitch were removed in pre-processing using (6) and (7) on the mean of a sufficiently large data window.
- The in-plane (in body frame coordinates) acceleration measurements were used. The horizontal plane acceleration will be shown to follow a bivariate statistical distribution, see III-B. This distribution has clear mathematical advantages. By omitting the vertical acceleration, compensation of fast pitch motions was not needed.

E. Training data sets

Training data sets were recorded under the following conditions:

- The training data sets were collected at a constant speed of the vessel (5 knots). The result of the ice condition assessment depends on the speed of the vessel. Therefore the validation data were recorded under normal ice-breaking velocities of the vessel (3-7.5 knots).
- Because the sensor was placed in the bow, the ice action had to occur against the bow of the vessel.

Four ice conditions are shown in Figure 3. The upper left image shows the condition of open water, denoted as $\mathcal{H}_{OW}$. The upper right image shows a condition of open ice, $\mathcal{H}_{OI}$. The lower left image shows close ice, $\mathcal{H}_{CI}$, and the lower right image shows very close ice, $\mathcal{H}_{VCI}$. Half a minute of accelerations were recorded by the IMUs under each ice condition. These data were used as training data for the detection system. The rotated x- and y-acceleration data from IMU 1 and IMU 2 are depicted in Figures 4a and 4b, respectively, for each of the ice conditions. The scatter plots also include the 99%-confidence ellipses for data from each ice condition. The measurements from both IMUs, for all ice conditions, are centred near the origin. Furthermore, the radius of the confidence ellipses increases with the severity of the ice conditions. The reason is that the measured accelerations scatter significantly more under heavy ice conditions due to an increase in variance of the recorded signals. The data from IMU 2 show significantly more scattering for each ice condition than data from IMU 1. The additional local vibrations $\boldsymbol{\xi}_s^b$, present at the location of IMU 2, are assumed to give rise to this behaviour. Therefore, the measurements from the in-plane accelerometers of IMU 2 will be used throughout this study. Measurements from IMU 1 were discarded because they do not contain local ice-induced hull vibrations that would allow for a clear distinction of ice conditions based on acceleration data.

F. Problem statement

The change in ice conditions around a vessel is a continuous process. The severity of ship-ice interaction can be classified into a set of conditions, each of which characterise the distribution of hull accelerations. Table III describes four trained ice conditions. The number of ice conditions is arbitrary and can be increased if a more fine-grained classification is of interest. The ice condition can change without notice at an unknown change time k_0. The x- and y-components of the acceleration vector described in (5) are congregated in $\boldsymbol{z}$. At each time instance k, the last N measurements are considered: $\boldsymbol{z} \in \mathbb{R}^{2\times N}$. The measurements are assumed independent and distributed with a bivariate probability distribution $f(\boldsymbol{z};\boldsymbol{\theta})$. To show that statistical independence can be justified, the appendix provides a correlogram of the measurement data from case 1 (see Section V.A). The parameters $\boldsymbol{\theta}$ of this joint probability distribution change with the ice condition. Following the concept of change detection, described in [38], at a time instant k it must be decided which of the trained ice conditions fits the recorded data best. The problem consists of three parts:

- Estimation of the current parameter vector $\boldsymbol{\theta}$.
- Generation of a test statistic.
- Decide on an ice condition hypothesis $\mathcal{H}_p$.

This combination of estimation of parameters from given signals, change detection from an estimated set of parameters, and declaring a hypothesis from a test statistic defines a diagnostic system, as shown in Figure 5. The hypothesis testing is in its principles similar to the one-vs-all multi-class extension for support vector machines (SVMs) [39]. For each condition a hypothesis test exists to distinguish the data sample between two hypotheses, namely accept the condition or accept another condition.

TABLE III: Trained ice conditions.

Hypothesis	Ice condition	Ice cover*
$\mathcal{H}_{\mathrm{OW}}$	Open water	$< 10\%$
$\mathcal{H}_{\mathrm{OI}}$	Open pack ice	11% - 60%
$\mathcal{H}_{\mathrm{CI}}$	Close pack ice	61% - 80%
$\mathcal{H}_{\mathrm{VCI}}$	Very close pack ice	81% - 100%

*Visual ice coverage on sea surface.

III. Parameter estimation in bivariate t-distributed data

A. Statistical change detection for heavy-tailed data

Hypothesis testing in Gaussian distributed data is a well established field of research, and an extensive overview can be found in [40]. Detecting changes in a measured signal has parallels with outlier detection [41]. While in applied statistics, the multivariate t-distribution is well established and thoroughly treated in [42]–[44], it has just recently found interest in fault diagnosis and statistical change detection. In contrast to the Gaussian distribution, the t-distribution allows for better modelling of heavy tailed data. Heavy tailed data occur in cases of commonly expected outliers, which is often the case in tracking applications [45] or in any application where sudden changes are to be expected. Due to the heavy tail characteristic of t-distributed data, outliers in the data have less impact on the parameter estimates [46]. This allows for a more robust parameter estimation, which is crucial for reliable change detection [38].

For the purpose of drillstring washout detection, [47] first presented statistical change detection on t-distributed data using generalised log-likelihood ratio (GLR) testing. The authors

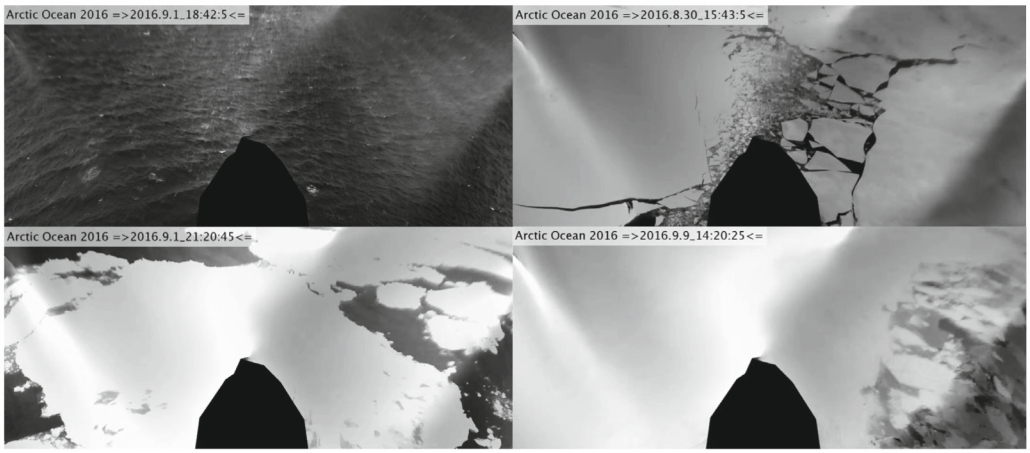

Fig. 3: Pictures of the trained ice conditions, a) Open Water b) Broken ice, c) Close ice d) Very close ice.

derived GLR tests for changes in the mean of univariate and multivariate t-distributed data. They assumed known scale and degrees of freedom parameters, and then they employed maximum likelihood estimators (MLE) for the estimation of the mean in the t-distributed data. For condition monitoring of floating wind turbine drivetrains, [48] showed that statistical change detection for unknown changes in scale and degrees of freedom of a univariate t-distribution can be used. The authors employed both a moment estimator and an MLE for estimation of the unknown parameters of the t-distribution. While a moment estimator for scale and degrees of freedom requires large window sizes for robust estimation and enough degrees of freedom, such that the excess kurtosis is defined ($\nu > 4$), the MLE provided robust estimates, also for short data windows, at the computational cost of solving a set of nonlinear equations.

B. Bivariate t-distribution

The previous study [28] showed that ice-induced accelerations can be statistically modelled by a univariate t-distribution. This is defined as

$$f(x;\mu,s,\nu) = \frac{\Gamma((1+\nu)/2)}{\Gamma(\nu/2)s\sqrt{\pi\nu}} \left(1 + \frac{(x-\mu)^2}{\nu s^2}\right)^{-\frac{1+\nu}{2}}, \quad (8)$$

where $\Gamma(x) = \int_0^\infty t^{z-1}e^{-1}\,\mathrm{d}t$ is the gamma function. The three parameters that define the t-distribution are: location $\mu \in \mathbb{R}$, scale $s \in \mathbb{R}$, and degrees of freedom $\nu \in \mathbb{R}$. The univariate t-distribution depends on the results from evaluating the gamma function, which is a computational burden when the parameters for the distribution have to be estimated [49]. To avoid this gamma function evaluation, the following will show how the parameters of a bivariate t-distribution can be estimated with ease if data sets of the x- and y-acceleration are used together.

The bivariate t-distribution is derived from the joint probability distribution function of a q-variate t-distribution based on the sample data vector $\boldsymbol{x} = [\boldsymbol{x}_1, \boldsymbol{x}_2, \ldots, \boldsymbol{x}_q]^{\mathrm{T}}$, according to [43]

$$f(\boldsymbol{x};\boldsymbol{\theta}) = \frac{\Gamma((q+\nu)/2)}{\Gamma(\nu/2)|\boldsymbol{S}|^{\frac{1}{2}}(\pi\nu)^{\frac{q}{2}}} \left(1 + \omega(\boldsymbol{x};\boldsymbol{\theta})\right)^{-\frac{q+\nu}{2}}, \quad (9)$$

with

$$\omega(\boldsymbol{x};\boldsymbol{\theta}) = \frac{1}{\nu}(\boldsymbol{x}-\boldsymbol{c})^{\mathrm{T}}\boldsymbol{S}^{-1}(\boldsymbol{x}-\boldsymbol{c}), \quad (10)$$

where $\boldsymbol{\theta} = [\boldsymbol{c}, \boldsymbol{S}, \nu]^{\mathrm{T}}$ congregates the parameters of the distribution. Furthermore, the mean vector is defined by $\boldsymbol{c} = [\mu_1, \mu_2, \ldots, \mu_q]^{\mathrm{T}}$, the correlation matrix is given by $\boldsymbol{S} \in \mathbb{R}^{q\times q}$, which contains the scale parameter $[s_1^2, s_2^2, \ldots, s_q^2]$ of each node on its diagonal entries, and the degrees of freedom of the distribution is ν.

As $\nu \to \infty$, (9) approaches the multivariate Gaussian distribution [49]. Therefore, the t-distribution is also suitable, as an approximation of the Gaussian distribution for large ν.

The x-acceleration and y-acceleration data can be considered as a sequence of two data sets $\boldsymbol{x}_1$ and $\boldsymbol{x}_2$, whose correlation is described by a correlation coefficient ρ. Each data set contains a sequence of independent random variables with $\boldsymbol{x}_1 \sim t(\mu_1, s_1, \nu)$, $\boldsymbol{x}_2 \sim t(\mu_2, s_2, \nu)$. The joint t-distribution (9) of $\boldsymbol{z} = [\boldsymbol{x}_1, \boldsymbol{x}_2]$ with $q = 2$ and

$$\boldsymbol{c} = [\mu_1, \mu_2]^{\mathrm{T}}, \quad (11)$$

is a bivariate t-distribution, given by

$$f(\boldsymbol{z};\boldsymbol{\theta}) = \frac{\Gamma(1+\nu/2)}{\Gamma(\nu/2)|\boldsymbol{S}|^{\frac{1}{2}}(\pi\nu)} \left(1 + \omega\left(\boldsymbol{z};\boldsymbol{\theta}\right)\right)^{-\frac{2+\nu}{2}}. \quad (12)$$

Using the fact that

$$\frac{\Gamma(1+\nu/2)}{\Gamma(\nu/2)(\pi\nu)} = \frac{1}{2\pi},$$

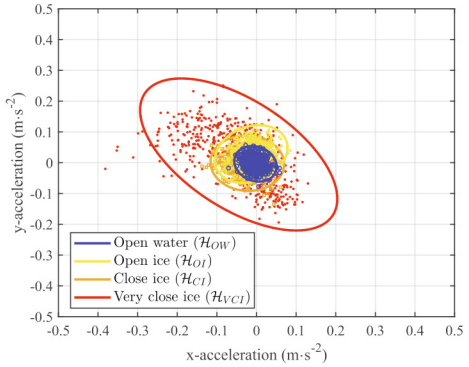

(a)

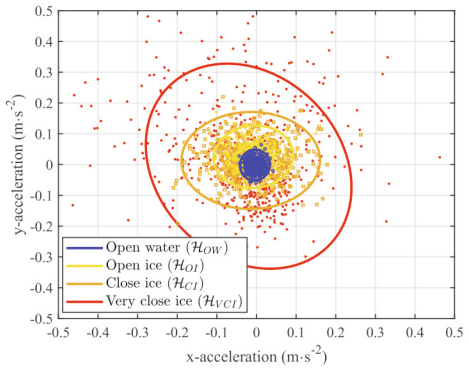

(b)

Fig. 4: Scatter plots of 30 seconds of acceleration data from (a) IMU 1, and (b) IMU 2 under each considered ice condition.

turns the evaluation of (12) particularly simple, since the Gamma function evaluation vanishes,

$$f(\boldsymbol{z};\boldsymbol{\theta}) = \frac{1}{2\pi|\boldsymbol{S}|^{\frac{1}{2}}} \cdot (1+\omega(\boldsymbol{z};\boldsymbol{\theta}))^{-\frac{2+\nu}{2}}, \tag{13}$$

where the correlation matrix of the x and y accelerations is described by

$$\boldsymbol{S} = \begin{bmatrix} s_1^2 & \rho s_1 s_2 \\ \rho s_1 s_2 & s_2^2 \end{bmatrix}. \tag{14}$$

The mean vector $\boldsymbol{c}$, which is caused by accelerometer bias, remains constant and very small over short windows of time. It is therefore only the scale matrix $\boldsymbol{S}$ and the degrees of freedom ν that change with ice condition. By removing all biases and the influence of the propulsion from the measurements, the mean vector is assumed zero under all ice conditions. The

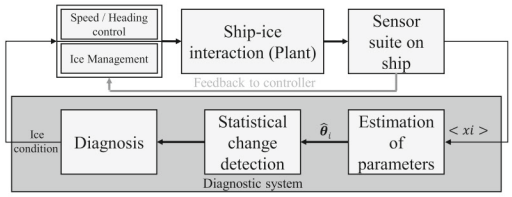

Fig. 5: Structure of an ice diagnostic system.

TABLE IV: Parameter estimates for the bivariate t-distributions under different ice conditions at constant speed (4 knots).

Condition (p)	μ	$s_{1,p}$	$s_{2,p}$	ρ_p	ν_p
Open water (OW)	0	$1.5 \cdot 10^{-4}$	$2.8 \cdot 10^{-4}$	$1 \cdot 4.7^{-6}$	20.0
Open ice (OI)	0	$1.1 \cdot 10^{-3}$	$1.1 \cdot 10^{-3}$	$6.3 \cdot 10^{-5}$	9.5
Close ice (CI)	0	$5 \cdot 10^{-3}$	$4.5 \cdot 10^{-3}$	$6 \cdot 10^{-4}$	8
Very close ice (VCI)	0	$0.7 \cdot 10^{-2}$	$1.2 \cdot 10^{-2}$	$2.0 \cdot 10^{-3}$	2.8

parameters are congregated in $\boldsymbol{\theta}_p = [\boldsymbol{0}, \boldsymbol{S}_p, \nu_p]^{\mathrm{T}}$ for each of the trained ice condition out of the set $p \in \{\mathrm{OW}, \mathrm{OI}, \mathrm{CI}, \mathrm{VCI}\}$; see Table IV. Note that the correlation ρ_p between the x and y accelerations is close to zero in all cases. We assume that the ice-induced vibrations measured by the bow sensor clearly dominates any wind-induced vibrations. Furthermore, we assume that waves can be neglected in the presence of sea ice. Therefore, the parameters in Table IV are assumed to be independent of weather conditions.

C. Maximum likelihood estimation of parameters

The parameters $\boldsymbol{S}$ and ν are estimated from data. Several methods are available among which a maximum likelihood estimation approach was found to be convenient. This estimator is derived as follows: Because an online estimation of the ice conditions is desired, a sliding window of length N selects a sequence $\boldsymbol{z}_i^k$ with $i = k - N + 1$ from the accelerometer measurements. The log-likelihood function for (13) is then

$$\mathcal{L}_i^k(\boldsymbol{S},\nu) = \sum_{j=1}^{N} \ln f(\boldsymbol{z}_i^k(j);\boldsymbol{\theta}) \tag{15}$$

$$\begin{aligned} &= \sum_{j=1}^{N} \ln |\boldsymbol{S}|^{-\frac{1}{2}} \left(1+\omega\left(\boldsymbol{z}_i^k(j);\boldsymbol{\theta}\right)\right)^{-\frac{2+\nu}{2}} \\ &= -\frac{N}{2} \cdot \ln|\boldsymbol{S}| \\ &\quad - \frac{2+\nu}{2} \cdot \sum_{j=1}^{N} \ln(1+\omega(\boldsymbol{z}_i^k(j);\boldsymbol{\theta})) \end{aligned} \tag{16}$$

The set of parameters $\boldsymbol{\theta}_p$ can be estimated by solving the maximisation problem

$$\hat{\boldsymbol{\theta}} = \arg\max_{\boldsymbol{S},\nu} \mathcal{L}_i^k(\boldsymbol{S},\nu). \tag{17}$$

TABLE V: Decision thresholds for hypothesis testing ($h_{\mathcal{G}}$) and for entropy based classification ($H(\theta)$).

Condition (p)	$h_{\mathcal{G}}$	$H(\boldsymbol{\theta})$
Open water (OW)	$9.55 \cdot 10^3$	≥ -12
Open ice (OI)	$1.12 \cdot 10^3$	≥ -5.0
Close ice (CI)	$0.57 \cdot 10^3$	≥ -3.2
Very close ice (VCI)	$0.07 \cdot 10^3$	≥ -1.8

To find the maximum of this expression, the derivatives of (16) with respects to $\boldsymbol{S}$ and ν have to be computed, and the resulting set of two equations has to be equated to zero. With $\boldsymbol{c} = [0, 0]^{\mathrm{T}}$, the following set of equations derived from

$$\frac{\partial \mathcal{L}_i^k(\boldsymbol{S}, \nu)}{\partial \boldsymbol{S}} = 0$$

gives

$$\begin{aligned} &- \frac{N}{2} \cdot \mathrm{tr}\left(\boldsymbol{S}^{-1}\right) \\ &+ \frac{2+\nu}{2} \cdot \sum_{j=1}^{N} \frac{\boldsymbol{z}_i^k(j)^{\mathrm{T}} \boldsymbol{S}^{-2} \boldsymbol{z}_i^k(j)}{\nu_p + \boldsymbol{z}_i^k(j)^{\mathrm{T}} \boldsymbol{S}^{-1} \boldsymbol{z}_i^k(j)} = 0, \end{aligned} \tag{18}$$

and from

$$\frac{\partial \mathcal{L}_i^k(\boldsymbol{S}, \nu)}{\partial \nu} = 0$$

gives

$$\begin{aligned} &\sum_{j=1}^{N} -\frac{1}{2} \ln\left(1 + \frac{1}{\nu} \boldsymbol{z}_i^k(j)^{\mathrm{T}} \boldsymbol{S}^{-1} \boldsymbol{z}_i^k(j)\right) \\ &+ \frac{2+\nu}{2} \cdot \frac{\boldsymbol{z}_i^k(j)^{\mathrm{T}} \boldsymbol{S}^{-1} \boldsymbol{z}_i^k(j)}{\nu \left(\boldsymbol{z}_i^k(j)^{\mathrm{T}} \boldsymbol{S}^{-1} \boldsymbol{z}_i^k(j) + \nu\right)} = 0. \end{aligned} \tag{19}$$

To obtain the estimate $\hat{\boldsymbol{\theta}} = [\boldsymbol{0}, \hat{\boldsymbol{S}}, \hat{\nu}]^{\mathrm{T}}$, the set of equations (18) and (19) has to be solved using a nonlinear solver as described in [50]. This result is the maximum likelihood estimate of the parameters that describe the distribution of data within a time window $\boldsymbol{z}_i^k$ of N samples.

IV. Methods for ice condition assessment

This section will introduce methods for assessment of ice condition based on statistical measures. A hypothesis test based on the Kullback-Leibler divergence is introduced to identify the condition out of the set of trained ice conditions, which has most similar distribution to the one observed. An alternative approach is the direct comparison of the signal's statistical entropy, which does not require trained data for comparison. Finally, two supervised machine learning approaches using a decision tree model and quadratic support vector machines allow for a benchmark between the two proposed custom methods and the two "off-the-shelf" machine learning approaches.

A. Hypothesis testing

The ice conditions during a sequence of N observations collected in a vector $\boldsymbol{z}_i^k$ with $i = k - N + 1$ are characterised by a bivariate t-distribution with an estimated parameter set $\hat{\boldsymbol{\theta}}$.

For each trained set of distribution parameters $\boldsymbol{\theta} = \{\boldsymbol{\theta}_p\}$, the distribution under the observed data is

$$\begin{aligned} &\mathcal{H}_p : \sum_{j=1}^{k} f(\boldsymbol{z}_i^k(j); \boldsymbol{\theta}_p) \\ &p \in \mathcal{P} = \{\mathrm{OW}, \mathrm{OI}, \mathrm{CI}, \mathrm{VCI}\} \end{aligned} \tag{20}$$

and the distribution with the estimated parameter set $\hat{\boldsymbol{\theta}}$:

$$\sum_{j=1}^{k} f(\boldsymbol{z}_i^k(j); \hat{\boldsymbol{\theta}}). \tag{21}$$

The problem is to find the trained ice condition p out of the set of trained conditions $\mathcal{P}$ that describes best the ice condition characterised by $\hat{\boldsymbol{\theta}}$. Each trained ice condition is described by a bivariate t-distribution with parameter set $\boldsymbol{\theta}_p$. A hypothesis test is needed to determine which condition $\boldsymbol{\theta}_p \in \mathcal{P}$ best describes the observed condition $\hat{\boldsymbol{\theta}}$.

For this purpose, the Kullback-Leibler divergence, see the overview in [51], provides a measure of the divergence between two probability distributions. Calculating the divergence between the current estimate with the parameter $\hat{\boldsymbol{\theta}}$ and any of the trained distributions with parameters $\boldsymbol{\theta}_p$, gives:

$$D_{kl,p}(k, \hat{\boldsymbol{\theta}} | \boldsymbol{\theta}_p) = \sum_{j=1}^{N} f(\boldsymbol{z}_i^k(j); \hat{\boldsymbol{\theta}}) \ln \frac{f(\boldsymbol{z}_i^k(j); \hat{\boldsymbol{\theta}})}{f(\boldsymbol{z}_i^k(j); \boldsymbol{\theta}_p)}. \tag{22}$$

The Kullback-Leibler divergence is 0 when the two distributions are identical.

If a trained ice condition $\boldsymbol{\theta}_p$ describes the current ice conditions well, then $D_{kl}(k, \hat{\boldsymbol{\theta}} | \boldsymbol{\theta}_p)$ will be a small positive number. To find the trained ice condition that best fits the observation, (22) is used as follows:

$$D_{kl}(k, \hat{\boldsymbol{\theta}} | \boldsymbol{\theta}_p) = \min_{p \in \mathcal{P}} \sum_{j=1}^{N} f(\boldsymbol{z}_i^k(j); \hat{\boldsymbol{\theta}}) \ln \frac{f(\boldsymbol{z}_i^k(j); \hat{\boldsymbol{\theta}})}{f(\boldsymbol{z}_i^k(j); \boldsymbol{\theta}_p)} \tag{23}$$

$$= \min_{p \in \mathcal{P}} G_i^k(\hat{\boldsymbol{\theta}}, \boldsymbol{\theta}_p). \tag{24}$$

Selection of Hypothesis: The minimisation over p in (23) finds the training distribution that is closest to the actual sequence of observations. Thus, the most likely condition can be communicated by evaluating:

$$p(k) = \arg\min_{p \in \mathcal{P}} D_{kl}(k, \hat{\boldsymbol{\theta}} | \boldsymbol{\theta}_p). \tag{25}$$

Equation (25) always provides a result that indicates which of the pre-trained conditions are closest, in terms of divergence measure, to the observed distribution. If two of the pre-trained conditions have the same divergence to the distribution obtained during the latest time window, the more severe condition is decided.

Test statistic: The test statistic can be evaluated using (13):

$$\frac{f(\boldsymbol{z}_i^k(j);\hat{\boldsymbol{\theta}})}{f(\boldsymbol{z}_i^k(j);\boldsymbol{\theta}_p)} = \frac{|\boldsymbol{S}_p|^{\frac{1}{2}} \cdot \left(1+\omega(\boldsymbol{z}_i^k(j);\hat{\boldsymbol{\theta}})\right)^{-\frac{2+\hat{\nu}}{2}}}{|\hat{\boldsymbol{S}}|^{\frac{1}{2}} \cdot \left(1+\omega(\boldsymbol{z}_i^k(j);\boldsymbol{\theta}_p)\right)^{-\frac{2+\nu_p}{2}}}, \tag{26}$$

where $\omega(\boldsymbol{z}_i^k(j);\boldsymbol{\theta})$ is defined in (10).

$$\begin{aligned} G_i^k(\hat{\boldsymbol{\theta}},\boldsymbol{\theta}_p) = &\sum_{j=1}^{N} \frac{\left(1+\omega(\boldsymbol{z}_i^k(j);\hat{\boldsymbol{\theta}})\right)^{-\frac{2+\hat{\nu}}{2}}}{2\pi|\hat{\boldsymbol{S}}|^{\frac{1}{2}}} \\ &\cdot \ln \frac{|\boldsymbol{S}_p|^{\frac{1}{2}} \cdot \left(1+\omega(\boldsymbol{z}_i^k(j);\hat{\boldsymbol{\theta}})\right)^{-\frac{2+\hat{\nu}}{2}}}{|\hat{\boldsymbol{S}}|^{\frac{1}{2}} \cdot \left(1+\omega(\boldsymbol{z}_i^k(j);\boldsymbol{\theta}_p)\right)^{-\frac{2+\nu_p}{2}}} \end{aligned} \tag{27}$$

It can be of interest to know how well an estimated distribution is separated from the other pre-trained conditions. This information can be conducted by applying a supplemental threshold test. With a threshold h, the hypothesis test can be supplemented with the following test:

$$\begin{aligned} &\text{For each } \; p \in \mathcal{P} \\ &\qquad \text{if} \quad D_{kl}(k,\hat{\boldsymbol{\theta}}|\boldsymbol{\theta}_p) \le h_{\mathcal{G}} \quad \text{accept} \quad \mathcal{H}_p \\ &\qquad \text{if} \quad D_{kl}(k,\hat{\boldsymbol{\theta}}|\boldsymbol{\theta}_p) > h_{\mathcal{G}} \quad \text{accept} \quad \mathcal{H}_{\neq p}. \end{aligned} \tag{28}$$

Figure 6 shows the results of (27) for all combinations of trained ice condition and the entire set of trained conditions, which are represented by the t-distributions with estimated parameters for each condition. A threshold $h_{\mathcal{G}}$ can be determined for each ice condition to clearly separate the correct ice condition from any other of the trained conditions. The procedure of selecting a value of $h_{\mathcal{G}}$ is described in Appendix B.

This section has shown how an estimate of the distribution, based on horizontal acceleration data over a time window, can be compared with pre-trained data, and a multiple hypothesis test can determine which of the pre-trained conditions are closest to the one observed. A threshold method was suggested as a supplemental means to determine how well the observed data fit one of the trained conditions. When pre-trained data are not available, ice load level assessment can be made anyway, using a measure of statistical entropy. This approach is elaborated next.

B. Condition assessment through statistical entropy

The Kullback-Leibler divergence is closely related to the statistical entropy [51]. The statistical entropy is a measure on the extent a single probability distribution concentrates on a few points or disperses over many points [42]. Figure 4b shows how the dispersion of datapoints depends on the ice condition.

The differential entropy for a random variable $\mathbf{Z}$ with probability function $f(\boldsymbol{z}_i^k(j);\boldsymbol{\theta})$, data sequence $\boldsymbol{z}_i^k(j)$ of length N with $i = k - N + 1$, and parameter vector $\boldsymbol{\theta}$, is defined by [52] as

$$H(\mathbf{Z}) = -\sum_{j=1}^{N} f(\boldsymbol{z}_i^k(j);\boldsymbol{\theta}) \ln f(\boldsymbol{z}_i^k(j);\boldsymbol{\theta}). \tag{29}$$

For a q-variate, central ($\boldsymbol{c} = 0$) t-distribution (9), and the parameter estimate $\hat{\boldsymbol{\theta}} = [\mathbf{0}, \hat{\boldsymbol{S}}, \hat{\nu}]^{\mathrm{T}}$, the entropy solely depends on the parameter estimate $\hat{\boldsymbol{\theta}}$ and is given by [53] as

$$\begin{aligned} H(\hat{\boldsymbol{\theta}}) = &\frac{1}{2}\ln|\hat{\boldsymbol{S}}| \\ &+ \ln\left(\frac{(\hat{\nu}\pi)^{\frac{q}{2}}}{\Gamma\left(\frac{q}{2}\right)} B\left(\frac{q}{2},\frac{\hat{\nu}}{2}\right)\right) \\ &+ \frac{q+\hat{\nu}}{2}\left(\psi\left(\frac{q+\hat{\nu}}{2}\right) - \psi\left(\frac{\hat{\nu}}{2}\right)\right), \end{aligned} \tag{30}$$

where $\psi(x) = \mathrm{d}\ln(\Gamma(x))/\mathrm{d}x$ denotes the digamma function, and $B(x,y) = \Gamma(x)\Gamma(y)\Gamma(x+y)^{-1}$ denotes the beta function.

For a bivariate t-distribution ($q = 2$), the expression (30) can be significantly simplified, using $\Gamma(x+1) = x\Gamma(x)$, and $\psi(x+1) = \psi(x) + x^{-1}$ to give:

$$H(\hat{\boldsymbol{\theta}}) = \frac{1}{2}\ln|\hat{\boldsymbol{S}}| + \ln(2\pi) + \left(\frac{\hat{\nu}}{\hat{\nu}+2}\right). \tag{31}$$

Figure 7 shows the entropy for the four different ice conditions of Figure 3. The ice conditions can be discriminated by defining entropy thresholds using the training data set. Those entropy specific thresholds are given in Table V. The statistical entropy is seen to associate a monotonic increasing grade to ice condition. Being an absolute measure related to measured accelerations, the statistical entropy measure can be extrapolated beyond the range of pre-classified conditions, and it can express a condition in between those that were pre-classified. The expression (31) is computationally efficient.

C. Algorithm for ice condition assessment

The following algorithm summarises the proposed methods for ice condition assessment:

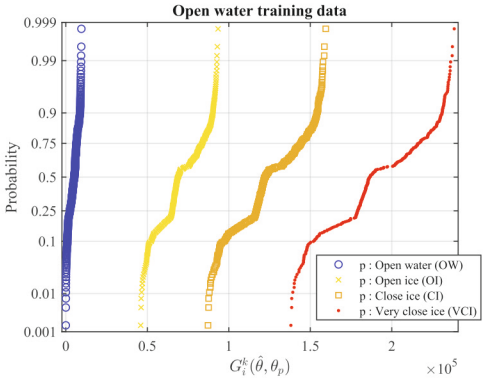

(a) Test statistic for trained open water parameter set

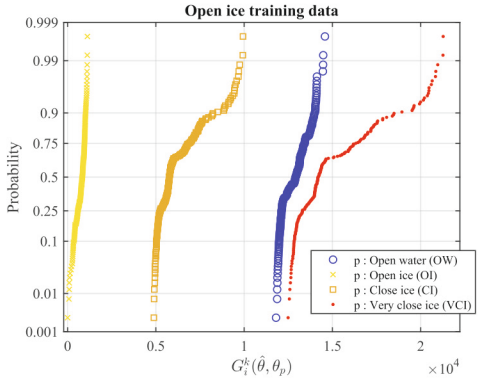

(b) Test statistic for trained open ice parameter set

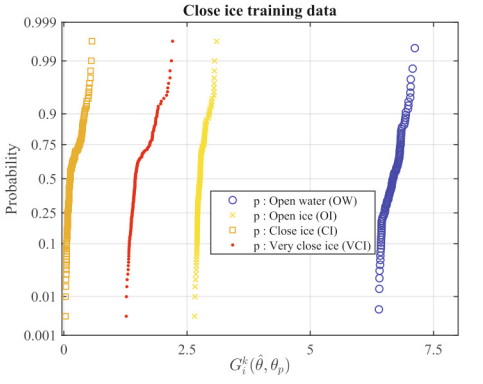

(c) Test statistic for trained close ice parameter set

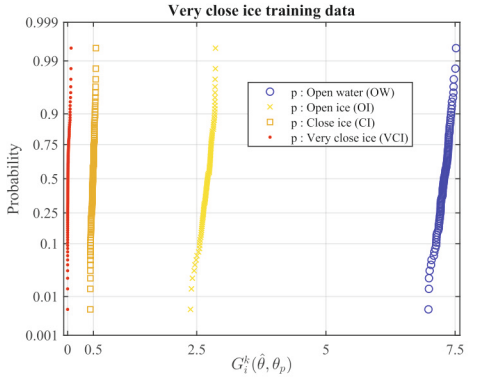

(d) Test statistic for trained very close ice parameter set

Fig. 6: Probability plots of the result from the test statistic (27) with different data sets under each trained ice condition.

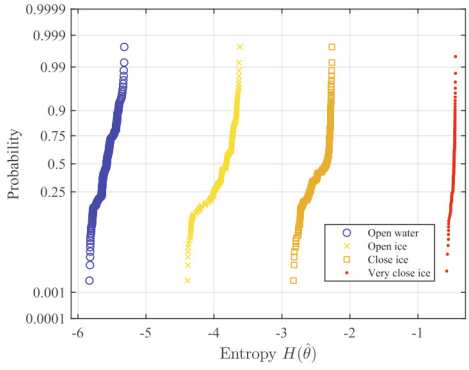

Fig. 7: Probability plot of the entropy results under the four training data ice conditions.

Algorithm IV.1
Ice condition assessment algorithm

Preprocessing

- *Collect motion data for a data window of length N.*
- *Apply Chebyshev lowpass filter.*
- *Calculate roll (6) and pitch (7).*
- *Correct for attitude of sensor using (1).*

Parameter estimation

- *Find $\hat{\boldsymbol{S}}$ and $\hat{\nu}$ with (18) and (19).*

Ice condition assessment Method 1

- *Calculate test statistics (27).*
- *Find minimum in (24) and evaluate (25).*
- *In case two pre-trained conditions have the same divergence to the observed distribution, chose the more severe of these.*

Ice condition assessment Method 2

- *Calculate statistical entropy using (31).*
- *Evaluate ice condition against predefined thresholds (Table V).*

Result

- *Vector $p(k)$ with decisions on ice condition at bow.*

D. Machine learning approaches

Two standard machine learning approaches serve as a benchmark for the statistical classification methods introduced earlier. Both machine learning approaches were trained with the training data presented in Figures 3 and 4b.

The Matlab® Classification Learner toolbox provides a number of supervised machine learning approach for training of classification models, among others decision tree models, support vector machines, and nearest neighbour classifiers. An overview of classification learning methods is given in [54].

Training data: Using the pure acceleration data as depicted in Figure 4b did not result in reasonable classification models. Therefore, the machine learning models were trained with statistical data, specifically the components of the correlation matrix (14) and the degrees of freedom ν as described in (13). For each considered ice condition, 30 seconds of training data were used, the same length as for the earlier described change detection methods.

Validation: Cross-validation with five folds was used for validation of the trained models. For this approach the training data were partitioned into five disjoint sets. For each set the model was trained with the data which were not part of the specific set. The data in the remaining disjoint sets were used for validation. The process was repeated for each set. The best training results were archived with a decision tree model and a quadratic state-vector machine.

Decision Tree model: Decision Trees are a popular methods for classification models [55]. A detailed survey on the construction of decision trees can be found in [56]. Figure 8 illustrates the trained decision tree for ice condition classification.

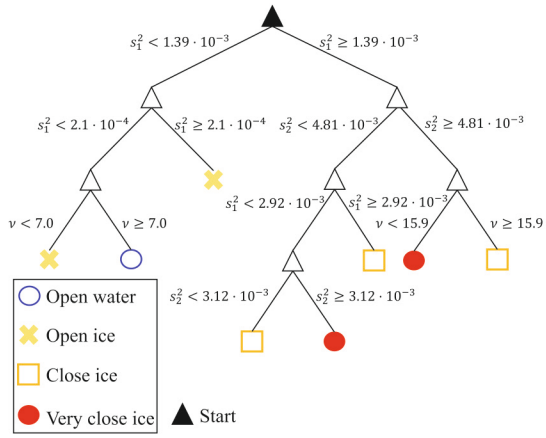

Fig. 8: Trained decision tree for ice condition detection

Support vector machine: Support vector machines try to classify training data by introducing separating hyperplanes which depend on data points lying on margins called support vectors. Maximisation of the margins results in better generalised performance under unknown data; see [57]. A kernel operation can transform the training or input data to a higher dimension feature space, which allows a clearer definition of the margin regions. The best SVMs were obtained using a quadratic kernel and the statistical properties of the training data as input, specifically the results from equations (18) and (19). Figure 9 contains three plots that illustrate the relation between the estimated parameters of the statistical model (12) for each ice condition in the training sets. It is obvious that already with a linear SVM, planes can be constructed to separate the ice conditions well. The quadratic SVM uses a quadratic kernel to create a transformed feature space, allowing for an even better separation of the ice condition regions.

V. Validation of Custom Classification Methods Using Full Scale Data

For three data sets, recorded during transit in ice, the ice conditions at the bow of the vessel were determined using two custom classification algorithms IV.1 with the trained parameter sets (Table IV) and thresholds (Table V) found with the training data set. The data sets serve as validation for the proposed ice condition assessment system. In all cases, the apparent windspeed and the heading of the vessel were constant during the measurements. The sampling rate of the sensors was decimated to 20 Hz. A sliding window collects measurement samples for processing. The window size determines the detection delay (more delay with larger data window), but also the steadiness of the detection result (more steady results with larger data window). Figure 10 presents the detection results for three different window sizes. As a

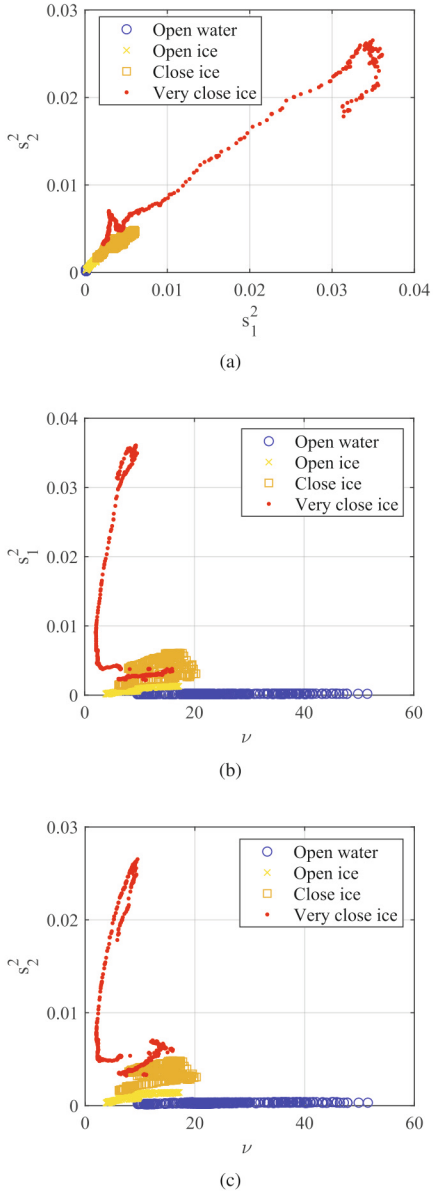

Fig. 9: Scatterplots of statistical parameters of the training data for model (13) (a) s_1^2 and s_2^2 (b) ν and s_1^2 (c) ν and s_2^2.

compromise between speed of detection and steadiness of result, a window size of 10 seconds was chosen for this study.

Figures 12 - 14 consist each of four sections:

1) Section (1) shows images from a camera system. The images were taking in synchronisation with the acceleration measurements.
2) Section (2) gives a plot of the ice concentration at the bow of the ship. The ice concentration has been continuously determined (every 5 seconds) from the images using image processing techniques described in [8]. Because the camera system can only differentiate between ice cover and open water, and does not include a measure of other ice properties such as thickness or porosity, the camera analysis is merely an indicator of the ice condition.
3) Section (3) presents the results from the differential entropy based classification of ice conditions. The section contains a plot of the entropy (31), and a colourbar, which indicates the results of the classification using the thresholds defined in Table V.
4) Section (4) gives the results of the hypothesis test. The decision function $G_i^k(\boldsymbol{\theta}_p, \hat{\boldsymbol{\theta}})$ for each trained ice condition are plotted, and the result of (25) are illustrated as a colourbar.

A. Case 1: Transit in open water until impact with a single ice floe

In the scenario shown in Figure 12, the ship travelled at 6 knots in open water. Upon impact with an ice floe at 21:20.30 the speed over ground reduced to 4.5 knots.

Both diagnostic approaches recognise correctly the open water condition at the beginning. Before the impact with the solid ice floe smaller ice pieces were encountered, which both systems classify as open ice condition. Upon impact with the unbroken ice floe, the ship slows down due to the pressure

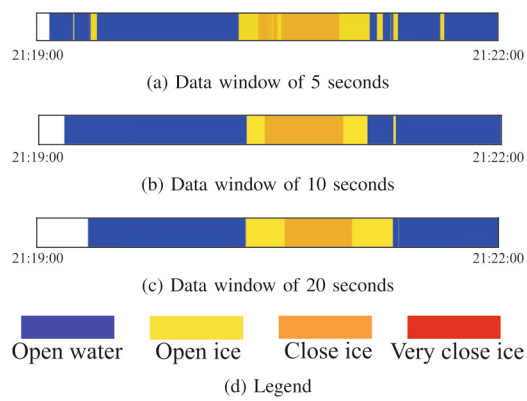

Fig. 10: Detection results of Case 1 data under hypothesis testing with different data window sizes.

increase against the hull. Both approaches detect close ice conditions. The pressure against the hull was released when the ice floe broke. This causes the classification of the ice condition to change to open ice. Towards the end of the measurement the ship pushed the broken ice floes away instead of further breaking them. This means that the bow of the vessel travelled in open water, which is correctly assessed by both diagnostic approaches. The entropy based method reacts more sensitive to changes in the ice conditions.

B. Case 2: Transit in broken ice

Figure 13 shows the diagnostic results during transit at 7.5 knots in broken ice of 30-40 cm thickness.

At first the ship travelled for a short period in open water, which both methods detect correctly. At 15:39.40 the ship entered broken ice, and both approaches for the diagnostic system correctly classify this as open ice. At 15:39:45 both methods declare the encounter with a smaller unbroken ice floe as close ice. At 15:40:30 the ship encountered several larger ice pieces, which were rammed and split. Both methods declare this as close ice. At 15:41.50 the ship encountered open water followed by a channel of broken ice as shown in the last image of Figure 13. Both system declare the open water correctly. The entropy based method reacts faster on the ice condition change. Compared to the result from the camera system, the entropy based method seems to be more correct, especially because it registers earlier the encounter of unbroken ice pieces at 15:40:30.

C. Case 3: Transit in close ice

Figure 14 shows the third scenario in which the ship encountered heavy ice conditions. The ice in this case was thicker (>50cm) than in the previous two cases. It consisted mostly of closed level ice with areas of newly frozen ice in between. The ship travelled at 6.5 - 7.5 knots.

Both the entropy and the hypothesis testing methods register close ice conditions at the bow of the vessel in the beginning of the measurement with a short moment of open ice. At 11:29.40, the ship encountered a large, unbroken ice floe (with a diameter of 80-100 metres). It required several seconds until the ice floe broke. During this time the pressure against the hull increased so much that both methods classify the situation as very close ice conditions. The speed of the vessel reduced nearly to zero. At 11:30.25 the ice floe split and the pressure was released. At this point the results from the two approaches deviate slightly. The entropy based approach detects open ice conditions while the hypothesis testing approach detects first close ice conditions. The camera image at 11:31.00 shows an area of newly formed ice, which should not create major resistance against the hull. Therefore the entropy-based result seems correct. Upon inspection of the full camera image several ice pieces starboard of the vessel are visible. These have formed a string and broke simultaneously just before 11:31.00; see Figure 11. This may have caused pressure against the hull. On the image at 11:32.00 an unbroken larger ice floe can be seen ahead of the vessel's bow. At 11:32.35 the ship split the ice floe. Both systems declare this event as very close ice conditions. On the last image a major unbroken ice floe is visible. Forty seconds later the ship hits this ice floe. That causes the ice diagnostic system to declare the situation correctly as very close ice conditions again.

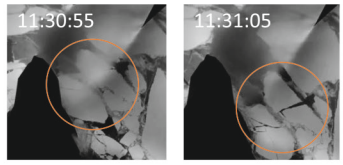

Fig. 11: Simultaneous breaking of ice pieces starboard of vessel at 11:31.00.

D. Comparison with machine learning approaches

Figure 15 gives a comparison of the detector results of custom classification methods with the results from the two trained "off-the-shelf" machine learning classification models introduced earlier.

Using the data of Case 1, in which the vessel encountered a larger unbroken ice floe, all methods are capable of detecting the event. During transit in open water the decision tree based classification model often classifies open ice conditions. The SVM model provides more steady results. As an example, Figure 16a provides a ground truth of the ice situation at 21:19:15 (marked with a black line in Figure 15a). The bow was completely surrounded by open water. Therefore, the assessment of the decision tree method is wrong.

Using the data of Case 2, in which the vessel transited in broken ice and encountered an area of open water, the decision tree model works more stable, whereas the SVM model provides more erratic classification during the open ice situation. All methods, however, detect correctly the open water periods. The machine learning based models seem to react faster on changes. Figure 16b shows that at 15:41:40 (marked with a black line in Figure 15b) the bow of the vessel was already inside open water. The statistical change detection methods react a few seconds delayed due to the sliding data window. On the other hand, the sliding data window allows for a more steady result compared to the machine learning based models.

Using the data of Case 3, in which the vessel was exposed to more severe ice conditions, all four methods detect all three encounters of large and unbroken ice features (very close ice conditions). The open water patch in the middle of the measurement was thereafter reliably detected by all methods. The SVM based classification gives more erratic results. In the last quarter of the measurement, the decision tree model wrongly classifies open water, where the camera images do show the presence of light ice conditions; see Figure 16c. Although it looks like open water, the bow actually travelled inside thin, unbroken ice just in front of a major unbroken ice floe. Open water appears darker on the image, as it is visible in

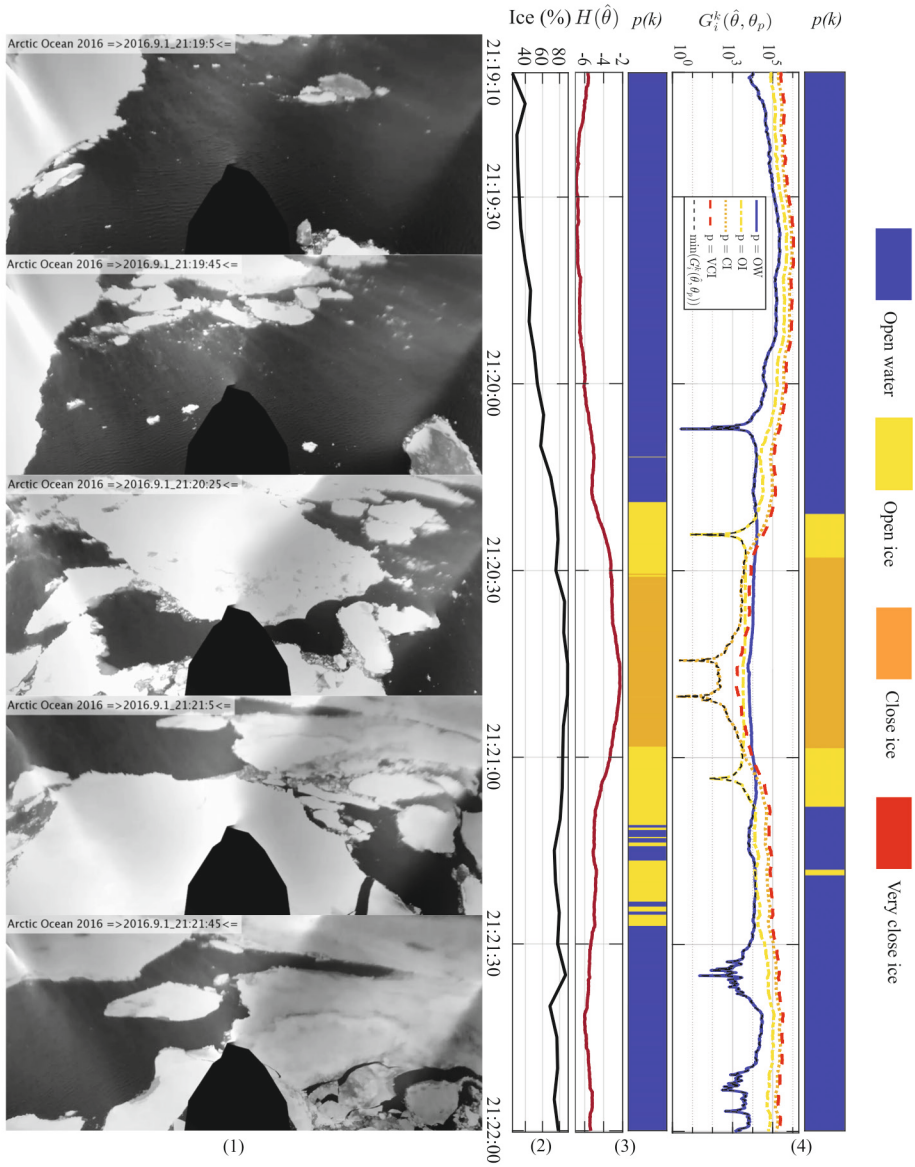

Fig. 12: Test statistic and classification result during transit onto an solid ice floe in open water (Case 1).

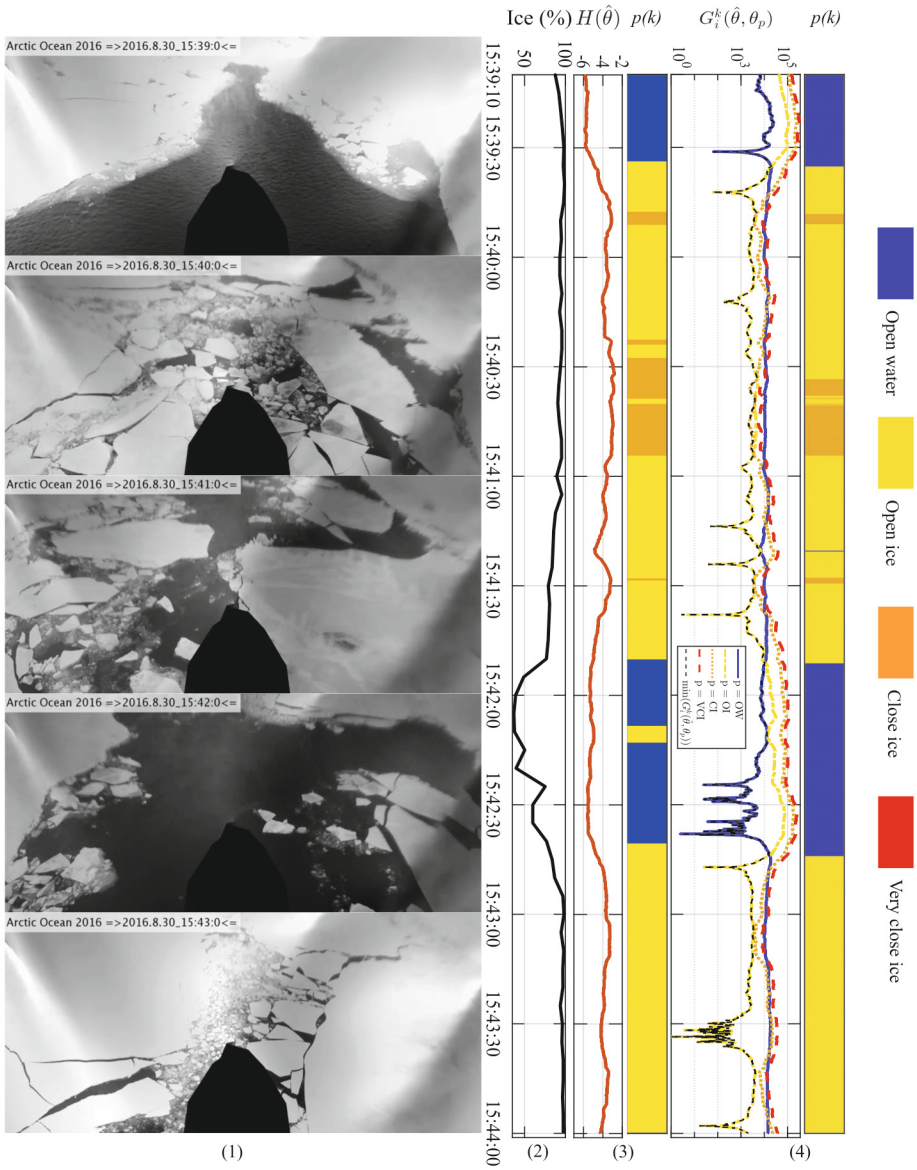

Fig. 13: Test statistic and classification result during transit in broken ice (Case 2).

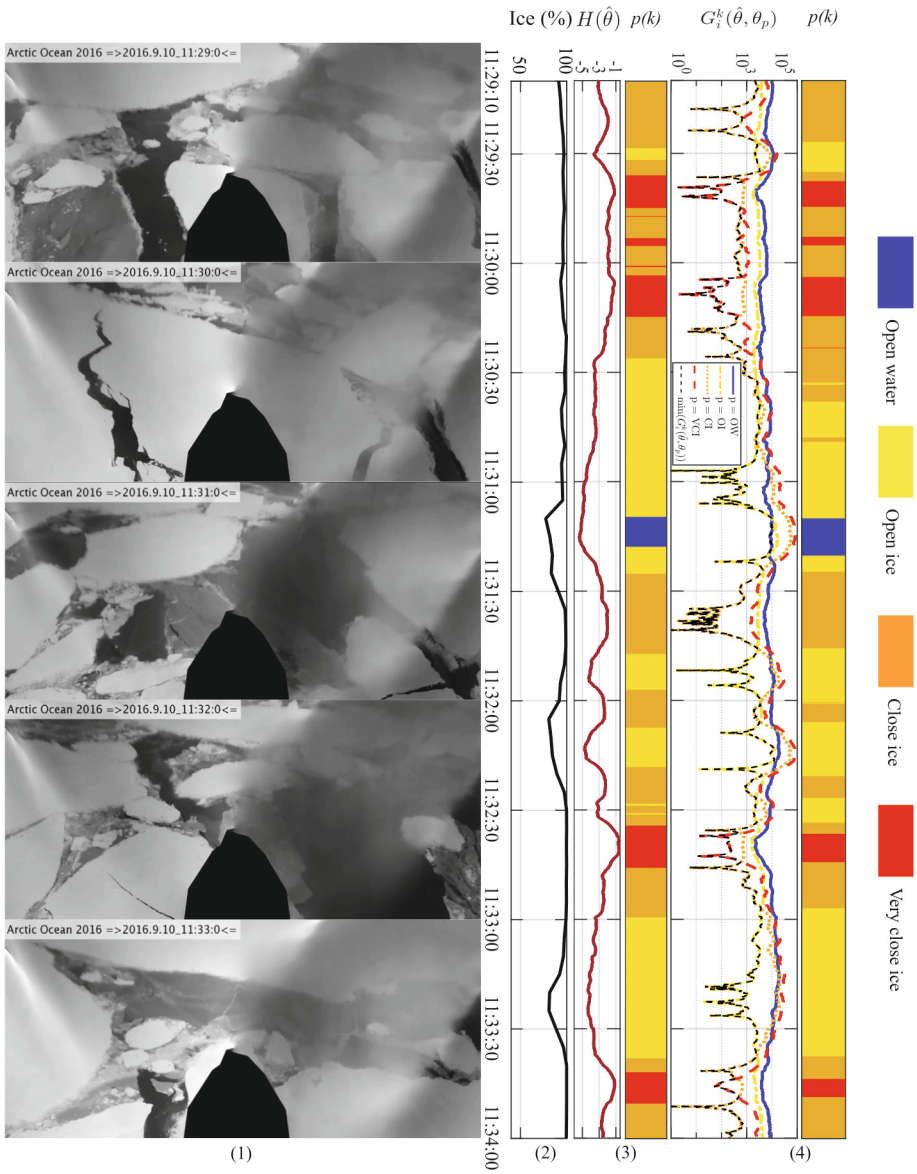

Fig. 14: Test statistic and classification result during transit in close ice (Case 3).

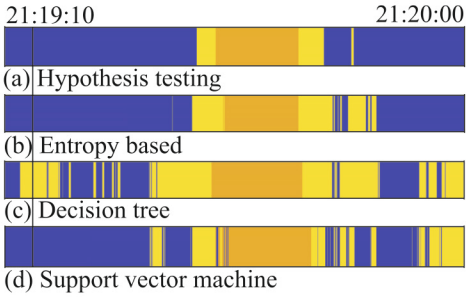

(a) Comparison of classification results for transit onto solid ice floe in open water (Case 1).

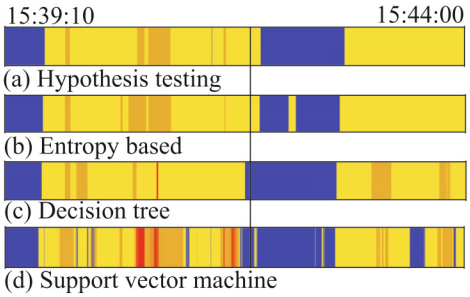

(b) Comparison of classification results during transit in broken ice (Case 2).

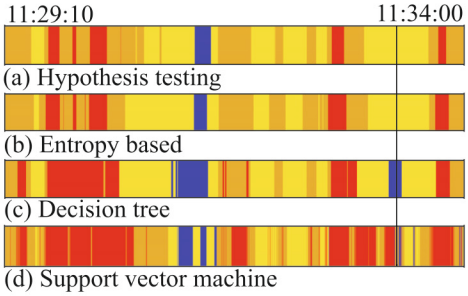

(c) Comparison of classification results during transit in close ice (Case 3).

(d) Legend

Fig. 15: Comparison of custom classification methods with "off-the-shelf" machine learning approaches.

the left part of the image, where patches of sea water are visible where the thin ice had broken up. Therefore, the assessment of open ice is correct.

(a) Ice situation Case 1 at 21:19:15

(b) Ice situation Case 2 at 15:41:40

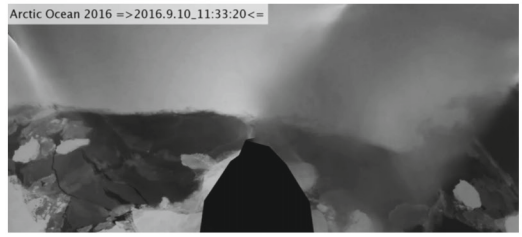

(c) Ice situation Case 3 at 11:30:20

Fig. 16: Use of image proof to determine correct ice condition

VI. Discussion, Perspectives, and Conclusion

A. Discussion

Two custom classification algorithms, that are based on estimating the parameters of the t-distribution of data, were compared with two machine learning methods. The methods have the following characteristics:

- *Hypothesis test* is made by calculating (27). Training data are needed to represent the categories in which we wish to classify the ice condition. A hypothesis is selected that is closest to fits a category using (25). This study used four categories of ice conditions. Data represented each by parameters of the associated t-distribution. Additional training data can easily be added, should this be preferred.
- *Entropy test* provides an absolute measure through calculation of (31). The entropy detector can extrapolate to conditions where training data are not available, and can

interpolate, and can supplement the hypothesis test.
- *Two machine learning* methods were employed: a decision tree model and a support vector machine model. The training data sets were used for learning. The training of machine learning models to data is transparent and does not physical behaviours are not directly represented in model parametrization.

The comparison of the two statical methods with the two selected approaches from machine learning showed that the statistical methods, being based on inherent knowledge of the underlying statistics of the physical processes, provide steadier results. The statistical tests have the window size is a tuning parameter and more steady, albeit slower, assessment can be achieved by using a larger data window size for parameter estimation.

All methods were able to detect sudden and significant changes of ice conditions, for example the transition from open ice to harsh unbroken ice.

The training of machine learning models require test cases to train correct classification, and it is difficult to control how the models adapt to each ice condition. For example, the automatically trained decision tree model in Figure 8 is unnecessarily complicated and does not follow a physical reasoning.

The statistical classification is based on a physical reasoning: Heavier ice conditions causes more fluctuations of the hull vibrations, and as a result the scale parameter of the t-distribution increases. Furthermore, high energy spikes, caused by the interaction of heavy ice feature, result in a heavy-tail characteristic of the recorded signal, which results in a low degree of freedom of the estimated t-distribution. An automatically trained machine learning model does not take these physical phenomena into account.

B. Perspective

The installation of IMUs in the hull of an ice-going ship is very simple. In combination with the proposed diagnostic system, there is a range of applications that this system can be used for:

- The most obvious application is a decision support system for ice-going vessel, especially container vessels travelling the Arctic sea route or cruise ships entering ice-infested waters. The system can support a warning system for getting locked-in ice. The system can also assist icebreakers which scout ice conditions for ice management.
- By distributing a sensor array in the hull of the vessel, a local awareness of the ice conditions around a vessel can be obtained. Although the system has not yet been deployed during stationkeeping in ice, it can be tested if the proposed diagnostic system can detect the accumulation of ice at one side of the stationkeeping vessel; see [58]. This information can be forwarded to a control system, which e.g. changes the heading of the stationkeeping vessel to counteract the accumulation of ice along the hull.
- The system is currently a reactive system. It communicates the ice conditions, which are directly affecting the vessel. However, a deeper statistical analysis using extreme value prediction of occurring ice loads can allow for a forecasting of ice loads.
- This diagnostic system might be extended to differentiate between different sea states in open water, see [59] and references herein. In addition to in-plane accelerometers, data from z-acceleration, angular rates, and roll-pitch motion could be utilised, and a multiple hypothesis test could be designed to decide between different sea states.

C. Conclusion

A system for ice condition assessment was developed which solely used data from accelerometers in the hull of an ice-going vessel. Merging the data from the in-plane accelerometers, it was possible to describe the ice-induced accelerations with a bivariate t-distribution. The bivariate t-distribution made it possible to obtain a maximum likelihood estimator without making use of the Gamma function, and it appeared to be very robust. Training data from different ice conditions gave reference parameters of bivariate t-distributions that represented each of the training conditions.

Two principal custom methods were proposed for detection of the prevailing ice condition. A modified Kullback-Leibler divergence formulation was used with a hypothesis testing scheme to classify the current ice condition being closest to a training condition. A second method did not require training data but utilised the change in statistical entropy of the accelerations. It was found that the entropy changes significantly, and in a monotone way with ice conditions, which demonstrated that the entropy measure is a good indicator for ice load. Additionally, a decision tree model and a support vector machine classifier were trained with the same training data as the custom methods.

All classification methods were tested on three data sets, obtained during transit in the Arctic Ocean under different ice conditions. Both statistical classification methods, i.e., hypothesis testing and entropy estimation, produced valid and very similar results for the ice condition assessment, which appeared to agree with the ice conditions judged from simultaneous camera system recordings. Classification using standard machine learning models also produced valid results, but they showed to be more fluctuating.

Working 24/7, being independent of visibility conditions, and providing objective estimates of ice condition, it is concluded that an IMU-based ice condition monitoring system can indeed be a good addition for decision support on vessels operating in ice-infested waters. Installation of the required sensors is easy, the method works robustly, and extrapolation outside training data will be feasible. Further possible applications of the monitoring system were proposed, such as the detection of ice accumulation along the hull of a ship.

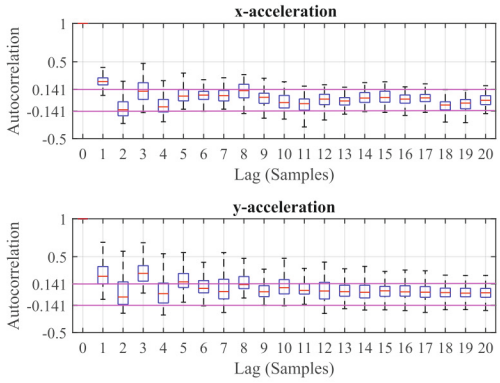

Fig. 17: Correlogram of Case 1 measurements from IMU 2

APPENDIX A
STATISTICAL INDEPENDENCE OF MEASUREMENTS

One assumption is that the measurements are independent. To show that this assumption is justified, Figure 17 presents a correlogram of the measurements from Case 1. The entire dataset contained 3600 datapoints. Because the proposed system operates on data windows of 200 samples, the autocorrelation function was determined for a sliding window of 200 samples at a time. The results are presented as boxplots, showing in red the median value, and the box representing the 25th to 75th percentiles. The 95% confidence interval for assuming statistically independence is indicated as purple line. The correlation plot shows for both x- and y-accelerations an autocorrelation on the first lag (and third lag for y-acceleration) that exceeds independence level. All other lags show an autocorrelation that supports the hypothesis of independence within a 95% confidence level. Because data originate from a physical process, the assumption of statistical independence may not hold perfectly. One consequence is that the test statistics (27) will not follow a chi-square distribution [40], [47]. The evidence for independence is concluded to be strong enough for our development.

APPENDIX B
THRESHOLD SELECTION

This appendix details how a threshold is determined from test data.

Algorithm B.1
Threshold calculation algorithm.

Distribution of test statistics

- *Given the training datasets $z(k;p)$, $p \in P$ and the parameter vector $\boldsymbol{\theta}_p$ for each training data set.*
- *Calculate the cumulative distributions $\mathcal{G}_{q,p}$ of the test statistics $\boldsymbol{G}_i^k(\boldsymbol{\theta}_q, \boldsymbol{\theta}_p)$, $q \in P$ and $q \neq p$.*
- *Approximate each of the cumulative distributions $\mathcal{G}_{q,p}(G)$ by smooth functions $\mathcal{F}_{q,p}(G)$.*
- *Define a probability of wrong classification P_{clas} e.g. 10^{-4}.*
- *$\forall q, p, q \neq p$, find a threshold $h_{\mathcal{G}} = \max_h |\mathcal{G}_{q,p}(h)| \leq P_{clas}$.*

Result

- *A threshold $h_{\mathcal{G}}$ that can determine whether an observed cumulative distribution $\boldsymbol{G}_i^k(\hat{\boldsymbol{\theta}}, \boldsymbol{\theta}_p)$ is separated sufficiently from all but one of the training sets with a probability P_{clas}.*

ACKNOWLEDGMENT

The authors would like to thank the Research Council of Norway (RCN) for financial support through projects 203471 CRI SAMCoT and 223254 CoE AMOS and the Swedish Polar Research Secretariat for support through the SWEDARCTIC 2016 research program.

REFERENCES

[1] N. Bock, "Sustainable Development Considerations in the Arctic," in *Environmental Security in the Arctic Ocean*, P. A. Berkman and A. N. Vylegzhanin, Eds. Cambridge: Cambridge University Press, 2010, pp. 37–59. [Online]. Available: http://ebooks.cambridge.org/ref/id/CBO9781107415324A009

[2] J. M. Hamilton, "The Challenges of Deep Water Arctic Development," *Isope*, vol. 8, no. 4, pp. 1–7, 2011.

[3] R. Skjetne, L. Imsland, and S. Løset, "The Arctic DP research project: Effective stationkeeping in ice," *Modeling, Identification and Control*, vol. 35, no. 4, pp. 191–210, 2014.

[4] K. Eik, "Review of Experiences within Ice and Iceberg Management," *Journal of Navigation*, vol. 61, no. 04, p. 557, 2008.

[5] H. Bjørklund, A. Sinitsyn, and A. Prusakov, "360 degree camera system for monitoring ice conditions," *Proceedings of the 23rd International Conference on Port and Ocean Engineering under Arctic Conditions*, 2015.

[6] M. Suominen, J. Kulovesi, M. Lensu, J. Lehtiranta, and P. Kujala, "A Comparison of Shipborne Methods for Ice Thickness Determination," in *22nd international Symposium on Ice*, Singapore, 2014.

[7] Q. Zhang and R. Skjetne, *Sea Ice Image Processing with MATLAB*. Boca Raton: CRC Press, 2018.

[8] H.-M. Heyn, M. Knoche, Q. Zhang, and R. Skjetne, "A system for automated vision-based sea-ice concentration detection and floe-size distribution indication from an icebreaker," in *Proceedings of the 36th International Conference on Ocean, Offshore & Arctic Engineering*, Trondheim, 2017.

[9] Q. Zhang and R. Skjetne, "Image Processing for Identification of Sea-Ice Floes and the Floe Size Distributions," *IEEE Transactions on Geoscience and Remote Sensing*, vol. 53, no. 5, pp. 2913–2924, 5 2015.

[10] ——, "Image Techniques for Identifying Sea-Ice Parameters," *Modeling, Identification and Control: A Norwegian Research Bulletin*, vol. 35, no. 4, pp. 293–301, 2014.

[11] P. Lu and Z. Li, "A method of obtaining ice concentration and floe size from shipboard oblique sea ice images," *IEEE Transactions on Geoscience and Remote Sensing*, vol. 48, no. 7, pp. 2771–2780, 2010.

[12] W. Lu, Q. Zhang, R. Lubbad, S. Løset, and R. Skjetne, "A Shipborne Measurement System to Acquire Sea Ice Thickness and Concentration at Engineering Scale Installation of Cameras," in *Arctic Technology Conference 2016*, 2016.

[13] Ø. K. Kjerstad, S. Løset, R. Skjetne, and R. A. Skarbø, "An Ice-Drift Estimation Algorithm Using Radar and Ship Motion Measurements," *IEEE Transactions on Geoscience and Remote Sensing*, pp. 1–13, 2018.

[14] A. Parsa and D. Smith, "Remote Sensing of Sea Ice Using Co- and Cross-Polarization Measurements with Shipborne Radar," *International Journal of Offshore and Polar Engineering*, vol. 26, no. 4, pp. 321–326, 2016.

[15] T. Toyota, K. Nakamura, S. Uto, K. I. Ohshima, and N. Ebuchi, "Retrieval of sea ice thickness distribution in the seasonal ice zone from airborne L-band SAR," *International Journal of Remote Sensing*, vol. 30, no. 12, pp. 3171–3189, 2009.

[16] M. Johnston, R. Frederking, G. Timco, and M. Miles, "Using Motan To Measure Global Accelerations of the Ccgs Terry Fox During Bergy Bit Trials," *International Conference on Offshore Mechanics and Arctic Engineering*, pp. 1–8, 2004.

[17] O. K. Kjerstad and R. Skjetne, "Disturbance Rejection by Acceleration Feedforward for Marine Surface Vessels," *IEEE Access*, vol. 4, pp. 2656–2669, 2016.

[18] Ø. K. Kjerstad, W. Lu, R. Skjetne, and S. Løset, "A method for real-time estimation of full-scale global ice loads on floating structures," *Cold Regions Science and Technology*, 2018.

[19] M. Suominen and P. Kujala, "Variation in short-term ice-induced load amplitudes on a ship's hull and related probability distributions," *Cold Regions Science and Technology*, vol. 106-107, pp. 131–140, 10 2014.

[20] B. Leira, L. Børsheim, . Espeland, and J. Amdahl, "Ice-load estimation for a ship hull based on continuous response monitoring," *Proceedings of the Institution of Mechanical Engineers, Part M: Journal of Engineering for the Maritime Environment*, vol. 223, no. 4, pp. 529–540, 11 2009.

[21] M. Johnston, R. Frederking, G. Timco, and M. Miles, "MOTAN: A Novel Approach for determining Ice-Induced Global Loads on Ships," *Proceedings MARI-TECH 2003*, no. 05, pp. 1–17, 2003.

[22] S. van der Werff, A. Haase, R. Huijsmans, and Q. Zhang, "Influence of the ice concentration on the ice loads on the hull of a ship in a managed ice field," in *Proceedings of the ASME 2012 31st International Conference on Ocean, Offshore and Arctic Engineering*, Rio de Janeiro, 2012, pp. 1–7.

[23] S. Løset, K. N. Shkhinek, O. T. Gudmestad, and K. V. Høyland, *Actions from ice on Arctic offshore and coastal structures*. LAN, 2006.

[24] K. Riska, "Ship-ice interaction in ship design: Theory and practice," Developed under the Auspices of the UNESCO, Tech. Rep., 2011.

[25] I. J. Jordaan, "Mechanics of ice - structure interaction," *Engineering Fracture Mechanics*, vol. 68, pp. 1923–1960, 2001.

[26] A. Suyuthi, B. J. Leira, and K. Riska, "Short term extreme statistics of local ice loads on ship hulls," *Cold Regions Science and Technology*, vol. 82, pp. 130–143, 2012.

[27] ——, "A generalized probabilistic model of ice load peaks on ship hulls in broken-ice fields," *Cold Regions Science and Technology*, vol. 97, pp. 7–20, 2014.

[28] H.-M. Heyn, G. Udjus, and R. Skjetne, "Distributed motion sensing on ships," in *Oceans 17 Conference*, 2017.

[29] P. Kujala, *On the statistics of ice loads on ship hull in the Baltic /*. Finish Academy of Technology, 1994.

[30] K. Gårdfeldt and . Lindgren, "SWEDARCTIC Arctic Ocean 2016," Swedish Polar Research Secretariat, Stockholm, Tech. Rep., 2017.

[31] R. Lubbad, E. V. Raaij, and K. J. Eik, "Oden Arctic Technology Research Cruise 2012," in *22nd International Conference on Port and Ocean Engineering under Arctic Conditions*, vol. 2012. Offshore Technology Conference, 10 2013, pp. 1–13. [Online]. Available: http://www.onepetro.org/doi/10.4043/27340-MS

[32] Analog Devices Inc., "Data Sheet ADIS 16364," Analog Devices Inc., Norwood, Tech. Rep., 2011.

[33] T. I. Fossen, *Handbook of Marine Craft Hydrodynamics and Motion Control*. Chichester, UK: John Wiley & Sons, Ltd, 4 2011.

[34] A. Noureldin, T. B. Karamat, and J. Georgy, *Fundamentals of inertial navigation, satellite-based positioning and their integration*. Berlin, Heidelberg: Springer Berlin Heidelberg, 2013.

[35] T. H. Bryne, J. M. Hansen, R. H. Rogne, N. Sokolova, T. I. Fossen, and T. A. Johansen, "Nonlinear Observers for Integrated INS\/GNSS Navigation: Implementation Aspects," *IEEE Control Systems*, vol. 37, no. 3, pp. 59–86, jun 2017.

[36] J. Matusiak, "Dynamic loads and response of icebreaker Sisu during continuous icebreaking," Winter Navigation research board, Helsinki, Tech. Rep., 1982.

[37] H.-M. Heyn and R. Skjetne, "Time-frequency analysis of acceleration data from ship-ice interaction events," *Cold Regions Science and Technology*, no. January 2017, pp. 1–14, feb 2018.

[38] M. Blanke, M. Kinnaert, J. Lunze, and M. Staroswiecki, *Diagnosis and Fault-Tolerant Control*, 3rd ed. Berlin, Heidelberg: Springer Berlin Heidelberg, 2016.

[39] H. Joutsijoki and M. Juhola, "Comparing the One-vs-One and One-vs-All Methods in Benthic Macroinvertebrate Image Classification," in *Machine Learning and Data Mining in Pattern Recognition*, P. Perner, Ed. Berlin, Heidelberg: Springer Berlin Heidelberg, 2011, pp. 399–413.

[40] S. M. Kay, *Fundamentals of statistical signal processing, Vol. II: Detection Theory*. Signal Processing. Upper Saddle River, NJ: Prentice Hall, 1998.

[41] R. Domingues, M. Filippone, P. Michiardi, and J. Zouaoui, "A comparative evaluation of outlier detection algorithms: Experiments and analyses," *Pattern Recognition*, vol. 74, pp. 406–421, 2018.

[42] S. Nadarajah and S. Kotz, "Mathematical Properties of the Multivariate t Distribution," *Acta Applicandae Mathematicae*, vol. 89, no. 1-3, pp. 53–84, 2005.

[43] S. Kotz and S. Nadarajah, *Multivariate t Distributions and Their Applications*. Cambridge: Cambridge University Press, 2004.

[44] D. Peel and G. J. McLachlan, "Robust mixture modeling using the t distribution," *Journal Statistics and Computing*, vol. 10, pp. 339–348, 2000.

[45] C. Aeschliman, J. Park, and A. C. Kak, "A novel parameter estimation algorithm for the multivariate t-distribution and its application to computer vision," in *European Conference on Computer Vision*. Springer, 2010, pp. 594–607.

[46] Z. Khan, T. Balch, and F. Dellaert, "MCMC-based particle filtering for tracking a variable number of interacting targets," *IEEE Transactions on Pattern Analysis and Machine Intelligence*, vol. 27, no. 11, pp. 1805–1819, 2005.

[47] A. Willersrud, M. Blanke, L. Imsland, and A. Pavlov, "Drillstring Washout Diagnosis Using Friction Estimation and Statistical Change Detection," *IEEE Transactions on Control Systems Technology*, vol. 23, no. 5, pp. 1886–1900, 2015.

[48] M. Ghane, A. Nejad, M. Blanke, Z. Gao, and T. Moan, "Statistical fault diagnosis of wind turbine drivetrain applied to a 5MW floating wind turbine," *Journal of Physics: Conference Series*, vol. 753, no. 5, 2016.

[49] S. Nadarajah and S. Kotz, "Estimation methods for the multivariate t distribution," *Acta Applicandae Mathematicae*, vol. 102, no. 1, pp. 99–118, 2008.

[50] C. Liu and D. B. Rubin, "ML Estimation of the t Distribution using EM and its extensions, ECM and ECME," *Statistica Sinica*, vol. 5, no. 1, pp. 19–39, 1995.

[51] J. M. Joyce, "Kullback-Leibler Divergence," in *International Encyclopedia of Statistical Science*. Berlin, Heidelberg: Springer Berlin Heidelberg, 2011, pp. 720–722.

[52] J. Beirlant, E. Dudewicz, L. Györfi, and E. Van der Meulen, "Nonparametric entropy estimation: An overview," *International Journal of Mathematical and Statistical Sciences*, vol. 6, no. 1, pp. 17–39, 1997.

[53] J.-L. Guerrero-Cusumano, "A measure of total variability for the multivariate t distribution with applications to finance," *Information Sciences*, vol. 92, no. 1, pp. 47–63, 1996.

[54] C. Sammut, "Concept Learning," in *Encyclopedia of Machine Learning and Data Mining*, 2017, pp. 256–259.

[55] J. Furnkranz, "Decision Tree," in *Encyclopedia of Machine Learning and Data Mining*, 2017, pp. 256–259.

[56] S. K. Murthy, "Automatic Construction of Decision Trees from Data: A Multi-Disciplinary Survey," *Data Mining and Knowledge Discovery*, vol. 2, no. 4, pp. 345–389, 1998.

[57] X. Zhang, "Support Vector Machine," in *Encyclopedia of Machine Learning and Data Mining*, 2017, pp. 1214–1220.

[58] Ø. Kjerstad, I. Metrikin, S. Løset, and R. Skjetne, "Experimental and phenomenological investigation of dynamic positioning in managed ice," *Cold Regions Science and Technology*, vol. 111, pp. 67 – 79, 2015.

[59] U. Nielsen, R. Galeazzi, and A. H. Brodtkorb, "Evaluation of shipboard wave estimation techniques through model-scale experiments," in *Proceedings of OCEANS'16*, 2016.

Hans-Martin Heyn received the M.Sc in electrical engineering from RWTH Aachen University, Germany in 2013. In 2013 and 2014 he worked with projects on electromobility and battery charging algorithms at the E.ON Energy Research Center in Aachen, Germany. Since 2014 he pursuits a PhD at the Centre for Autonomous Marine Operations and Systems (AMOS) at the Department of Marine Technology at the Norwegian University of Science and Technology in Trondheim, Norway. His research interests are within autonomous robots and systems, distributed sensor systems, statistical signal processing, and fault diagnosis.

Mogens Blanke received the M.Sc. and Ph.D. degrees in electrical engineering from the Technical University of Denmark (DTU), Lyngby, Denmark, in 1974 and 1982, respectively. He has been Professor in Automation and Control at DTU since 2000 and, since 2005, also Adjunct Professor at the Center for Excellence fo Autonomous Marine Operations and Systems (AMOS) at the Norwegian University of Science and Technology, Trondheim, Norway. He was formerly full professor at Aalborg University (1990-1999), Head of Marine Division at Lyngsø Marine, Denmark (1985-1990), and was systems analyst at the European Space agency (1975-76). He has authored more than 270 scientific papers, book chapters and books including a widely recognized textbook on Diagnosis and Fault-tolerant Control. His research interests include general subjects in automation and control, fault diagnosis and prognosis, and fault-tolerant control systems. Mogens Blanke was technical editor for IEEE Transactions of Aerospace and Electronic Systems during a decade and has been dedicated editor for several special issues of international journals. He is currently associate editor for Control Engineering Practice. He received several awards and recognitions, including the ASME DSCD Rudolf Kalman Best Paper Award in 2018.

Roger Skjetne received his MSc degree in 2000 from the University of California at Santa Barbara (UCSB) and his PhD degree in 2005 from the Norwegian University of Science and Technology (NTNU) on control engineering. He holds an Exxon Mobil prize for his PhD thesis at NTNU. Prior to his studies, he worked as a certified electrician for Aker Elektro AS on numerous oil installations for the North Sea, and in 2004-2009 he was employed in Marine Cybernetics AS, working on Hardware-In-the-Loop simulation for testing marine control systems. From August 2009 he has held the Kongsberg Maritime chair of Professor in Marine Control Engineering at the Department of Marine Technology at NTNU. His research interests are within dynamic positioning of marine vessels, Arctic stationkeeping and Ice Management systems, control of shipboard hybrid electric power systems, nonlinear motion control of marine vehicles, and autonomous ships and marine robots.

8.2 Ice condition assessment during stationkeeping in sea ice

Paper 5: Heyn, Hans-Martin; Skjetne, Roger; Nord, Torodd Skjerve. Fast onboard detection of ice drift changes under stationkeeping in ice.

This article is awaiting publication and is therefore not included.

Part III

Closing remarks

Chapter 9

Conclusion and further work

> I can see now a vision emerging how Canada is going to profit in the future from our Arctic resources without destroying the environment on which it is all based.
>
> Brian Mulroney

This thesis presented a local ice monitoring system that supplement existing ice monitoring systems by providing weather-independent real-time information about the surrounding sea ice during Arctic operations.

9.1 Addressing research questions

Three sets of research questions framed this thesis:

1. **What characterises motion measurements during operations in sea ice? Why do these characteristics in the measurements occur? How can these characteristics be measured best?**

The answer to the first set of questions is given in Chapter 7 of this thesis. The excitation of vibrations at or close to the natural frequencies of the hull show distinct characteristics during ship-ice interaction. The interaction induces vibrations with frequency components up to 25 Hz, which are mostly only locally measureable. The frequency and amplitude of the vibrations change under different ice conditions because the resonance characteristics of the ship's hull depend on the properties of the interacting ice and the failure mode. The ice-induced vibrations have high frequencies, which is why the ship's structure absorbs them. Therefore, the motion sensors need to be placed as close to the ice interaction zone as possible.

Two effects cause the observed hull vibration phenomena. The interaction of ice with the ship's hull can be seen equivalent to a hammer hitting the hull and exciting the natural frequencies like a clapper does to a bell. Analogue to the bell, the ship's hull will vibrate at characteristic frequencies and the amount of energy of the hit determines the amplitude. Furthermore, as ice-floes get into contact with

the hull, they change the vibration characteristics of the hull, because the ice give additional mass and damping. This is analogue to that a weight attached to a bell changes the bell's tone.

2. **Why can motion sensing provide additional safety during operations in the Arctic? What are typical marine operations in sea ice that benefit from this technology?**

The second set of questions could be answered by demonstrating in Chapter 8 how the system has been applied during two typical full-scale operations in the Arctic: Transit in sea ice and stationkeeping in sea ice. To allow for motion sensing based ice condition assessment, the following methodologies were developed:

- Statistical analysis of the recorded acceleration signals showed that acceleration signals during ship-ice interaction can be modelled by a bivariate t-distribution. It was shown with full-scale measurement data that the statistical parameter of these distributions depend on the surrounding ice conditions. Methods from statistical signal processing and change detection allowed for algorithms that can detect changes in the surrounding ice conditions during transit.
- During stationkeeping, the induced vibrations are not distinct enough to allow for the statistical modelling with t-distributions. However, by evaluating the extreme value statistics of the induced vibrations, a relationship between the ice drift direction and the statistical properties of the recorded signal could be found.

Because motion sensing on ships works independently of external conditions such as weather or satellite coverage, a motion based ice monitoring is a valuable supplement to ice observer systems. This thesis showed that the system provides assessments of the surrounding ice conditions within seconds, allowing to abort a transit operation before the vessels gets locked into the ice. During stationkeeping, the system provides a real-time measurement of the ice-drift. The system detects ice-drift changes in the close vicinity of the stationkeeping vessel in real-time, which allows a swift reallocation of supporting icebreakers.

3. **How can motion sensing be integrated into the framework of an ice observer system?**

The last research question was answered by evaluating the structure of modern ice observer systems. Chapter 3 presents that structure and explains where and why a motion based local ice monitoring system can supplement existing ice monitoring systems.

9.2 Application of research

The presented methods allow for a diagnostic system on icebreakers, ice-going and ice-strengthened vessels operating in sea ice:

- Icebreakers obtain a fast and easy understandable assessment of the local ice conditions. During support operations for stationkeeping vessels, icebreakers often scout the surrounding sea ice for breakability. Motion sensors in the hull give a fast, and easy understandable assessment of the local ice conditions.
- Ice-going and ice-strengthened vessels on transit, such as cargo vessels travelling the Northeast passage or cruise vessels in polar regions, obtain an additional weather-independent tool for local ice monitoring. By issuing early warnings about potentially dangerous ice conditions, situations such as getting locked in impenetrable ice can be avoided. In light level ice, the crew can try to find the route of least ice resistance.
- Stationkeeping vessel in ice, for example for the purpose of oil exploration, obtain an additional tool for weather independent ice drift and ice accumulation detection. Especially sudden changes in ice drift are a challenge during these operations, which can be quickly detected by the proposed sensor system and methods. The system allows for automatic weather vaning of a stationkeeping vessel into the direction of the ice drift. The installation of motion sensors is by magnitudes simpler and cheaper than the equipment of stationkeeping vessels with strain gauges, which can give the same capability of ice drift change detection.
- Accumulation of ice along a structure can be detected by motion sensors. Fixed structures exposed to ice, such as platforms, lighthouses or bridges equipped with motion sensors can automatically detect the accumulation of sea ice along those structures.

Although this thesis focused on operations in the Arctic region, motion based local ice monitoring can also assist during Antarctic operations.

Distributed motion sensing outside the ice

The idea of distributed motion sensing can be applied in the field of sea state estimation in open waters, see for example [51] and references therein. Because the interaction with waves in open water causes hull vibration, algorithms can be developed that allow for an online sea-state estimation using motion data from the sensors. The angle of attack of incoming wave fronts can be determined with a spatially distributed system of motion sensors, see for example the preliminary work in [27].

9.3 Future research

Because of the retreating sea ice, marine operations and traffic in the polar regions will increase in the foreseeable future. Despite the retreating sea ice, it will still pose a threat to vessels in the polar regions, especially during the months outside the summer season. The increased presence of vessels in these regions will increase the likelihood of accidents.

Therefore, it is indispensable for the closer future to further develop ice observer systems that provide ice information to the crew or to control systems. An ice observer system consists already today of a huge number of different, partly independent, ice monitoring systems. It is a future challenge to integrate all different ice monitoring systems and to break down the ice data to easy understandable information for the crew.

Full autonomous ships can be imagined to sail the Northeast passage in the distant future. These ships will be equipped with a deeply autonomous, artificial intelligence (AI) based control system. These autonomous vessels could be equipped with a motion sensor array spanning all its hull as illustrated in Figure 9.1. An AI system would produce decisions based on the sensor readings in combination with other ice monitoring systems. The combination of an ice sensing hull and additional ice monitoring systems such as cameras, radar or even autonomous scouting drones would create full ice awareness of the vessel.

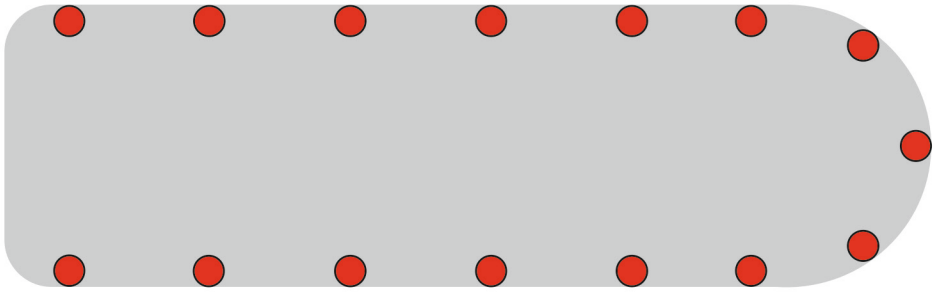

Figure 9.1: Proposed configuration for a multi-IMU system capable of sensing the precise location of ice pressure against the hull

References

[1] E. Almkvist, A. Kjøl, and A. Hansson. Station-keeping trials in ice: Data acquisition, post processing, storage and visualization. In *Proceedings of the 37th International Conference on Ocean, Offshore & Arctic Engineering*, Madrid, 2018. ASME.

[2] American Bureau of Shipping. Guide for ice loads monitoring systems. Technical report, American Bureau of Shipping, Houston, 2011.

[3] R. Amundsen. *The South Pole*. John Murray, London, 1912.

[4] Analog Devices Inc. Data Sheet ADIS 16364. Technical report, Analog Devices Inc., Norwood, 2011.

[5] Arctic Council. Arctic Marine Shipping Assessment 2009 Report. *Arctic*, pages 39–55, 2009.

[6] R. G. Barry. Remote Sensing of Sea Ice in the Northern Sea Route: Studies and Applications. *Eos, Transactions American Geophysical Union*, 89(27):248–248, 2008. ISSN 00963941. doi: 10.1029/2008EO270011.

[7] P. Batista, C. Silvestre, and P. Oliveira. On the observability of linear motion quantities in navigation systems. *Systems and Control Letters*, 60(2):101–110, 2011. ISSN 01676911. doi: 10.1016/j.sysconle.2010.11.002.

[8] A. Berg and L. E. B. Eriksson. Investigation of a Hybrid Algorithm for Sea Ice Drift Measurements Using Synthetic Aperture Radar Images. *IEEE Transactions on Geoscience and Remote Sensing*, 52(8):5023–5033, aug 2014. ISSN 0196-2892. doi: 10.1109/TGRS.2013.2286500.

[9] N. Bock. Sustainable Development Considerations in the Arctic. In P. A. Berkman and A. N. Vylegzhanin, editors, *Environmental Security in the Arctic Ocean*, pages 37–59. Cambridge University Press, Cambridge, 2010.

[10] A. Bogdanov, S. Sandven, O. Johannessen, V. Alexandrov, and L. Bobylev. Multisensor approach to automated classification of sea ice image data. *IEEE Transactions on Geoscience and Remote Sensing*, 43(7):1648–1664, 2005. ISSN 0196-2892. doi: 10.1109/TGRS.2005.846882.

[11] Bureau Vertias. Ice Load Monitoring System. Technical report, Bureau Vertias, Marine and Offshore Devision, Neuilly sur Seine Cedex, 2015.

[12] Det Norske Veritas. Rules for classification of ships, 2003. ISSN 0028-0836.

[13] K. Eik. Review of Experiences within Ice and Iceberg Management. *Journal of Navigation*, 61(04):557, 2008. ISSN 0373-4633. doi: 10.1017/S0373463308004839.

[14] D. Fields. The Concept of Relativity. In *Physics 262*, volume 26, chapter 26. University of New Mexico, 2015.

[15] I. O. for Standardization. ISO / FDIS 19906: Petroleum and natural gas industries — Arctic offshore structures, 2010.

[16] T. I. Fossen. *Handbook of Marine Craft Hydrodynamics and Motion Control*. John Wiley & Sons, Ltd, Chichester, UK, apr 2011. ISBN 9781119994138. doi: 10.1002/9781119994138.

[17] K. Gårdfeldt and Å. Lindgren. SWEDARCTIC Arctic Ocean 2016. Technical report, Swedish Polar Research Secretariat, Stockholm, 2017.

[18] D. L. Gautier, K. J. Bird, R. R. Charpentier, A. Grantz, D. W. Houseknecht, T. R. Klett, T. E. Moore, J. K. Pitman, C. J. Schenk, J. H. Schuenemeyer, K. Sørensen, M. E. Tennyson, Z. C. Valin, and C. J. Wandrey. Assessment of Undiscovered Oil and Gas in the Arctic. *Science*, 324(May):1175–1180, 2009.

[19] P. D. Groves. *Principles of GNSS, inertial, and multisensor integrated navigation systems*. Artech house, 2013.

[20] P. D. Groves. Navigation using inertial sensors [Tutorial]. *IEEE Aerosp. Electron. Syst. Mag.*, 30(2):42–69, 2015. ISSN 0885-8985. doi: 10.1109/MAES.2014.130191.

[21] C. Haas, J. Lobach, S. Hendricks, L. Rabenstein, and A. Pfaffling. Helicopter-borne measurements of sea ice thickness, using a small and lightweight, digital EM system. *Journal of Applied Geophysics*, 67(3):234–241, 2009. ISSN 09269851. doi: 10.1016/j.jappgeo.2008.05.005.

[22] R. J. Hall, N. Hughes, and P. Wadhams. A systematic method of obtaining ice concentration measurements from ship-based observations. *Cold Regions Science and Technology*, 34(2):97–102, 2002. ISSN 0165232X. doi: 10.1016/S0165-232X(01)00057-X.

[23] J. M. Hamilton. The Challenges of Deep Water Arctic Development. *Isope*, 8 (4):1–7, 2011. ISSN 10986189.

[24] Ø. Harsem, A. Eide, and K. Heen. Factors influencing future oil and gas prospects in the Arctic. *Energy Policy*, 39(12):8037–8045, 2017. ISSN 0301-4215. doi: 10.1016/j.enpol.2011.09.058.

[25] J. Haugen, L. Imsland, S. Løset, and R. Skjetne. Ice observer system for ice management operations. *Proceedings of the International Offshore and Polar Engineering Conference*, 8:1120–1127, 2011. ISSN 10986189.

[26] H.-M. Heyn and R. Skjetne. Time-frequency analysis of acceleration data from ship-ice interaction events. *Cold Regions Science and Technology*, 1 (January 2017):1–14, feb 2018. ISSN 0165232X. doi: 10.1016/j.coldregions.2018.01.019.

[27] H.-M. Heyn, G. Udjus, and R. Skjetne. Distributed motion sensing on ships. In *Oceans 17 Conference*, 2017.

[28] International Organization for Standardization. ISO / FDIS 35104: Petroleum and natural gas industries — Arctic operations — Ice management, 2017.

[29] M. Johnston, R. Frederking, G. Timco, and M. Miles. MOTAN: A Novel Approach for determining Ice-Induced Global Loads on Ships. *Proceedings MARI-TECH 2003*, pages 1–17, 2003. doi: 10.1039/B910216G.

[30] M. Johnston, R. Frederking, G. Timco, and M. Miles. Using MOTAN to measure Global Accelerations of the CCGS Terry Fox During Bergy Bit Trials. *Proceedings of the 23rd International Conference on Offshore Mechanics and Arctic Engineering*, pages 1–8, 2004. doi: 10.1115/OMAE2004-51239.

[31] Ø. K. Kjerstad and R. Skjetne. Disturbance Rejection by Acceleration Feedforward for Marine Surface Vessels. *IEEE Access*, 4:2656–2669, 2016. ISSN 2169-3536. doi: 10.1109/ACCESS.2016.2553719.

[32] Ø. K. Kjerstad, W. Lu, R. Skjetne, and S. Løset. A method for real-time estimation of full-scale global ice loads on floating structures. *Cold Regions Science and Technology*, 2018. doi: 10.1016/j.coldregions.2018.03.012.

[33] A. Lawrence. *Modern Inertial Technology*. Mechanical Engineering Series. Springer New York, New York, NY, 1998. ISBN 978-1-4684-0446-3. doi: 10.1007/978-1-4684-0444-9.

[34] B. Leira, L. Børsheim, Ø. Espeland, and J. Amdahl. Ice-load estimation for a ship hull based on continuous response monitoring. *Proceedings of the Institution of Mechanical Engineers, Part M: Journal of Engineering for the Maritime Environment*, 223(4):529–540, nov 2009. ISSN 1475-0902. doi: 10.1243/14750902JEME141.

[35] B. J. Leira and L. Borsheim. Estimation of Ice Load on a Ship Hull Based on Strain Measurements. In *Proceedings of the ASME 27th International Conference on Offshore Mechanics and Arctic Engineering*, pages 1–7. ASME, 2008.

[36] F. S. Leira, T. A. Johansen, and T. I. Fossen. A UAV ice tracking framework for autonomous sea ice management. *2017 International Conference on Unmanned Aircraft Systems, ICUAS 2017*, pages 581–590, 2017. doi: 10.1109/ICUAS.2017.7991435.

[37] P. Liferov, T. Mckeever, S. John, F. Scibilia, S. Asa, A. Kjøl, and E. Almkvist. Station-keeping trials in ice: Project overview. In *Proceedings of the 37th International Conference on Ocean, Offshore & Arctic Engineering*, pages 1–10, Madrid, 2018. ASME.

[38] P. Liferov, N. Serre, R. Bridges, and S. A. Total. Station-keeping trials in ice: Test scenarios. In *Proceedings of the 37th International Conference on Ocean, Offshore & Arctic Engineering*, pages 1–13, Madrid, 2018. ASME.

[39] S. Løset, K. N. Shkhinek, O. T. Gudmestad, and K. V. Høyland. *Actions from ice on Arctic offshore and coastal structures*. LAN, 2006. ISBN 5811407033.

[40] P. Lu and Z. Li. A method of obtaining ice concentration and floe size from shipboard oblique sea ice images. *IEEE Transactions on Geoscience and Remote Sensing*, 48(7):2771–2780, 2010. ISSN 01962892. doi: 10.1109/TGRS.2010.2042962.

[41] W. Lu, R. Lubbad, K. Høyland, and S. Løset. Physical model and theoretical model study of level ice and wide sloping structure interactions. *Cold Regions Science and Technology*, 101:40–72, 2014. ISSN 0165232X. doi: 10.1016/j.coldregions.2014.01.007.

[42] W. Lu, Q. Zhang, R. Lubbad, S. Løset, and R. Skjetne. A Shipborne Measurement System to Acquire Sea Ice Thickness and Concentration at Engineering Scale Installation of Cameras. In *Arctic Technology Conference 2016*, 2016.

[43] R. Lubbad and S. Løset. A numerical model for real-time simulation of ship-ice interaction. *Cold Regions Science and Technology*, 65(2):111–127, 2011. ISSN 0165232X. doi: 10.1016/j.coldregions.2010.09.004.

[44] R. Lubbad, S. Løset, U. Hedman, C. Holub, and D. Matskevitch. Oden Arctic Technology Research Cruise 2015. In *Arctic Technology Conference*, volume 2012, pages 1–13. Offshore Technology Conference, oct 2016. doi: 10.4043/27340-MS.

[45] R. Lubbad, S. Løset, W. Lu, A. Tsarau, and M. van den Berg. An overview of the Oden Arctic Technology Research Cruise 2015 (OATRC2015) and numerical simulations performed with SAMS driven by data collected during the cruise. *Cold Regions Science and Technology*, 1(December 2017):1–22, 2018. ISSN 0165232X. doi: 10.1016/j.coldregions.2018.04.006.

[46] J. Maslanik, J. Curry, S. Drobot, and G. Holland. Observations of sea ice using a low cost unpiloted aerial vehicle. *Proceedings of the 16th International Symposium on Sea Ice. International Association of Hydraulic Engineering and Research*, page 6, 2002.

[47] R. Massom and D. Lubin. *Polar Remote Sensing*, volume II of *Springer Praxis Books*. Springer Berlin Heidelberg, 2006. ISBN 978-3-540-26101-8. doi: 10.1007/3-540-30565-3.

[48] J. Matusiak. Dynamic loads and response of icebreaker Sisu during continuous icebreaking. Technical report, Winter Navigation research board, Helsinki, 1982.

[49] H. J. McGuinness, A. V. Rakholia, and G. W. Biedermann. High data-rate atom interferometer for measuring acceleration. *Applied Physics Letters*, 100 (1), 2012. doi: 10.1063/1.3673845.

[50] H. Meltofte. *Arctic Biodiversity Assessment: Synthesis*. Arctic Council, 2013. ISBN 9789935431288.

[51] U. Nielsen, R. Galeazzi, and A. H. Brodtkorb. Evaluation of shipboard wave estimation techniques through model-scale experiments. In *Proceedings of OCEANS'16*, 2016. doi: 10.1109/OCEANSAP.2016.7485701.

[52] P. Norgren and R. Skjetne. Using autonomous underwater vehicles as sensor platforms for ice-monitoring. *Modeling, Identification and Control*, 35(4):263–277, 2014. ISSN 03327353. doi: 10.4173/mic.2014.4.4.

[53] A. Noureldin, T. B. Karamat, and J. Georgy. *Fundamentals of inertial navigation, satellite-based positioning and their integration*. Springer Berlin Heidelberg, Berlin, Heidelberg, 2013. ISBN 9783642304668. doi: 10.1007/978-3-642-30466-8.

[54] Novatel. IMU Errors and Their Effects. Report APN-064 (Rev A). Technical report, Novatel Inc., 2014.

[55] H. Nyseth, A. Hansson, and J. J. Iseskär. Station-keeping trials in ice: Ice load monitoring system. In *Proceedings of the 37th International Conference on Ocean, Offshore & Arctic Engineering*, Madrid, 2018. ASME.

[56] K. Riska. *On the mechanics of the ramming interaction between a ship and a massive ice floe: Dissertation*. VTT Technical Research Centre of Finland, Helsinki University of Technology, Finland, 1987. ISBN 9513830004.

[57] K. Riska. Ship-ice interaction in ship design: Theory and practice. Technical report, Developed under the Auspices of the UNESCO, 2011.

[58] T. Sanderson. *Ice mechanics: risks to offshore structures*. Cold Region Engineering Studies. Graham & Trotman, 1988. ISBN 9780860107859.

[59] G. T. Schmidt and R. E. Phillips. INS / GPS Integration Architectures. *NATO Lecture Series*, 116(2011):1–18, 2011.

[60] R. Skjetne. Kinematic IMU equations. Technical report, University of California, Santa Barbara, 2018.

[61] M. Suominen, J. Kulovesi, M. Lensu, J. Lehtiranta, and P. Kujala. A Comparison of Shipborne Methods for Ice Thickness Determination. In *22nd international Symposium on Ice*, Singapore, 2014.

[62] S. H. T. Teigen, J. K. Lindvall, I. Samardzija, and R. I. Hansen. Station-keeping trials in ice: Ice and metocean conditions. In *Proceedings of the 37th International Conference on Ocean, Offshore & Arctic Engineering*, Madrid, 2018. ASME.

[63] T. Toyota, K. Nakamura, S. Uto, K. I. Ohshima, and N. Ebuchi. Retrieval of sea ice thickness distribution in the seasonal ice zone from airborne L-band SAR. *International Journal of Remote Sensing*, 30(12):3171–3189, 2009. ISSN 01431161. doi: 10.1080/01431160802558790.

[64] Wikimedia. CCGS Amundsen Wikicommons, 2018. URL https://upload.wikimedia.org/wikipedia/commons/8/82/CCGS{_}Amundsen2.jpg.

[65] Wikimedia. Icebreaker Frej Wikicommons, 2018. URL https://upload.wikimedia.org/wikipedia/commons/f/f2/Icebreaker_Frej_2004.jpg.

[66] O. R. Young. Arctic Futures: The Power of Ideas. In P. A. Berkman and A. N. Vylegzhanin, editors, *Environmental Security in the Arctic Ocean*, chapter 14, pages 123–136. Cambridge University Press, Cambridge, 2010.

[67] B. Zappa, G. Legnani, A. J. van den Bogert, and R. Adamini. On the Number and Placement of Accelerometers for Angular Velocity and Acceleration Determination. *Journal of Dynamic Systems, Measurement, and Control*, 123(3): 552–554, 2001. ISSN 00220434. doi: 10.1115/1.1386649.

[68] Q. Zhang and R. Skjetne. Image Techniques for Identifying Sea-Ice Parameters. *Modeling, Identification and Control: A Norwegian Research Bulletin*, 35(4): 293–301, 2014. ISSN 0332-7353. doi: 10.4173/mic.2014.4.6.

[69] Q. Zhang and R. Skjetne. Image Processing for Identification of Sea-Ice Floes and the Floe Size Distributions. *IEEE Transactions on Geoscience and Remote Sensing*, 53(5):2913–2924, 2015. ISSN 0196-2892. doi: 10.1109/TGRS.2014.2366640.

[70] Q. Zhang and R. Skjetne. *Sea Ice Image Processing with MATLAB*. Boca Raton: CRC Press, 2018. ISBN 9781351069199.

[71] Q. Zhang, R. Skjetne, S. Løset, and A. Marchenko. Digital Image Processing for Sea Ice Observations in Support to Arctic DP Operations. In *Volume 6: Materials Technology; Polar and Arctic Sciences and Technology; Petroleum Technology Symposium*. ASME, 2012. ISBN 978-0-7918-4493-9. doi: 10.1115/OMAE2012-83860.

[72] Q. Zhang, S. van der Werff, I. Metrikin, S. Løset, and R. Skjetne. Image Processing for the Analysis of an Evolving Broken-Ice Field in Model Testing. In *Volume 6: Materials Technology; Polar and Arctic Sciences and Technology; Petroleum Technology Symposium*, page 597. ASME, 2012. ISBN 978-0-7918-4493-9. doi: 10.1115/OMAE2012-84117.

ISBN 978-82-326-3874-1 (printed version)
ISBN 978-82-326-3875-8 (electronic version)
ISSN 1503-8181

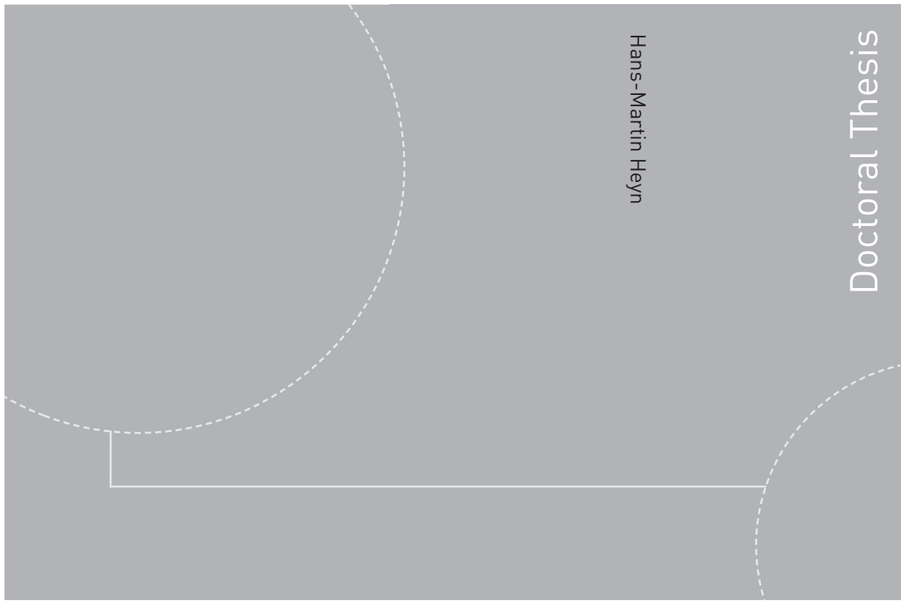

Doctoral theses at NTNU, 2019:138

Hans-Martin Heyn

Motion sensing on vessels operating in sea ice

A local ice monitoring system for transit and stationkeeping operations under the influence of sea ice

NTNU
Norwegian University of
Science and Technology
Faculty of Engineering
Department of Marine Technology

NTNU
Norwegian University of
Science and Technology

Doctoral theses at NTNU, 2019:138

NTNU

NTNU
Norwegian University of
Science and Technology